SANDIA REPORT
SAND2017-12565
Unlimited Release
Printed November 2017

Measuring Plasma Formation, Field Strength, and Current Loss in Pulsed Power Diodes

Mark D. Johnston, Sonal G. Patel, Ross E. Falcon, Keith Cartwright, Mark L. Kiefer, Michael E. Cuneo, and Yitzhak Maron

Prepared by
Sandia National Laboratories
Albuquerque, New Mexico 87185 and Livermore, California 94550

Sandia National Laboratories is a multimission laboratory managed and operated by National Technology and Engineering Solutions of Sandia, LLC, a wholly owned subsidiary of Honeywell International, Inc., for the U.S. Department of Energy's National Nuclear Security Administration under contract DE-NA0003525.

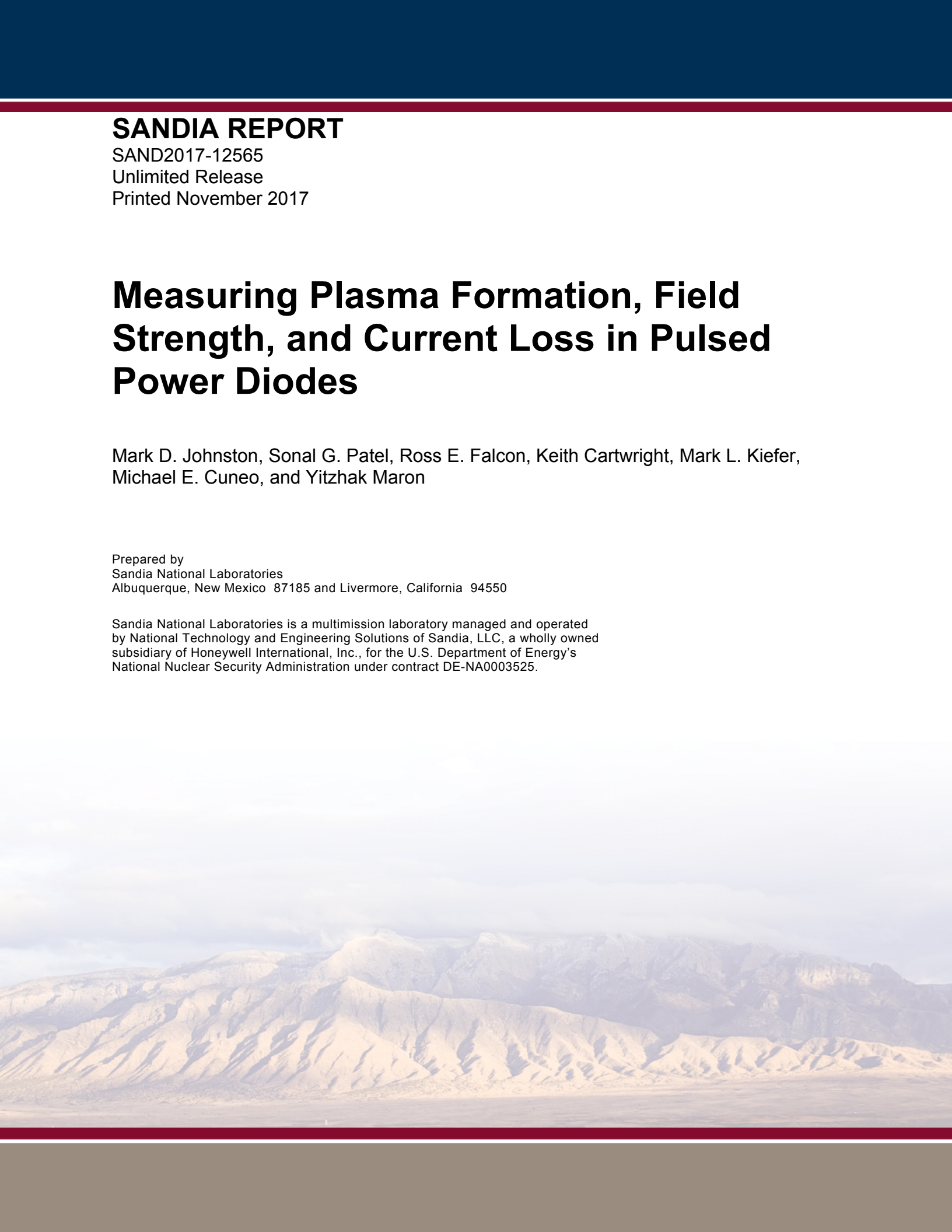

Issued by Sandia National Laboratories, operated for the United States Department of Energy by National Technology and Engineering Solutions of Sandia, LLC.

Available to DOE and DOE contractors from
U.S. Department of Energy
Office of Scientific and Technical Information
P.O. Box 62
Oak Ridge, TN 37831

Telephone: (865) 576-8401
Facsimile: (865) 576-5728
E-Mail: reports@osti.gov
Online ordering: http://www.osti.gov/scitech

Available to the public from
U.S. Department of Commerce
National Technical Information Service
5301 Shawnee Rd
Alexandria, VA 22312

Telephone: (800) 553-6847
Facsimile: (703) 605-6900
E-Mail: orders@ntis.gov
Online order: https://classic.ntis.gov/help/order-methods/

SAND2017-12565
Printed November 2017
Unlimited Release

Measuring Plasma Formation, Field Strength, and Current Loss in Pulsed Power Diodes

Mark D. Johnston[1], Sonal G. Patel, Ross E. Falcon, Keith Cartwright, Mark L. Kiefer, and Michael E. Cuneo
Advanced Radiographic Technologies Department
Sandia National Laboratories
P. O. Box 5800
Albuquerque, New Mexico 87185-MS1178

Yitzhak Maron
Weizmann Institute of Science
Rehovot, Israel 76100

Abstract

This LDRD investigated plasma formation, field strength, and current loss in pulsed power diodes. In particular the Self-Magnetic Pinch (SMP) e-beam diode was studied on the RITS-6 accelerator. Magnetic fields of a few Tesla and electric fields of several MV/cm were measured using visible spectroscopy techniques. The magnetic field measurements were then used to determine the current distribution in the diode. This distribution showed that significant beam current extends radially beyond the few millimeter x-ray focal spot diameter. Additionally, shielding of the magnetic field due to dense electrode surface plasmas was observed, quantified, and found to be consistent with the calculated Spitzer resistivity. In addition to the work on RITS, measurements were also made on the Z-machine looking to quantify plasmas within the power flow regions. Measurements were taken in the post-hole convolute and final feed gap regions on Z. Dopants were applied to power flow surfaces and measured spectroscopically. These measurements gave species and density/temperature estimates. Preliminary B-field measurements in the load region were attempted as well. Finally, simulation work using the EMPHASIS, electromagnetic particle in cell code, was conducted using the Z MITL conditions. The purpose of these simulations was to investigate several surface plasma generations models under Z conditions for comparison with experimental data.

[1]Email: mdjohn@sandia.gov

ACKNOWLEDGMENTS

The authors would like to acknowledge the RITS crew for helping to setup and field the experiments on RITS, in addition we would like to thank everyone associated with the Z-machine, and in particular the SVS team led by Dave Bliss and Dan Scoglietti for all their help and expertise fielding spectroscopy diagnostics on Z. We'd like to thank our management team for supporting this work, and in particular Mark Kiefer for his enthusiastic interest in this project, and the many hours of discussion we've had over the past three years. Finally, I'd like to thank Prof. Yitzhak Maron for all his work on this project. His collaboration was critical to the success of this endeavor. He has always been more than willing to lend his knowledge and expertise to this project and has been a great friend and mentor.

TABLE OF CONTENTS

FIGURES

TABLES

EXECUTIVE SUMMARY

The goal of this LDRD was to measure plasma parameters and fields in pulsed-power diodes using visible spectroscopy. In particular, experiments were conducted on the Self-Magnetic Pinch (SMP) e-beam diode on the RITS-6 accelerator, and on several load configurations on the Z Machine. Plasma parameters, such as temperatures and densities were measured, as well as magnetic fields from Zeeman splitting of spectral lines, and electric fields from Stark shifting of spectral lines. This project had several key accomplishments, including the first localized measurements of magnetic fields and current distributions on a TW particle beam diode using Zeeman spectroscopy, quantitative measurements of magnetic shielding due to electrode surface plasmas and subsequent plasma resistivity determinations, and electric field measurements of up to 9.5 MV/cm, representing the highest to date for a radiographic diode. In addition, the Z convolute was modeled using the EMPHASIS, finite-element PIC code, and the first attempts were made to use this code to evaluate various electrode plasma formation models using a first principles (non-empirical) approach. The results from this project are expected to improve the understanding of current distributions and losses in pulsed-power diodes, which is needed to increase the performance of existing machines like Z, and to have confidence in the designs of future machines like Z-Next, as well as provide input into models and simulations for radiographic diodes used in underground testing in support of the Stockpile Stewardship program. In conclusion, this LDRD made significant progress in developing the diagnostic techniques and analyses methods required to study plasma and fields in high energy, pulsed-power diodes. It is expected, that these techniques and methods will continue to be used and expanded upon in the years to come at Z and at other facilities.

1. INTRODUCTION

1.1. Objectives

The main purpose of this LDRD project was to investigate plasma formation, field strength, and current loss in pulsed power diodes. This originated from a proposed collaboration to leverage spectroscopy work being done at RITS, with power flow studies being done at Z. Previous LDRD proposals had been submitted to do electric and magnetic field measurements on the SMP diode on RITS, and similarly, a grand challenge LDRD, "New Capabilities for Hostile Environments on Z," [1] was underway on Z, which among other things was looking to investigate current losses in power flow regions near the load. Expanding upon the RITS and Z work, this LDRD sought to explore current loss through localized measurements of magnetic fields using visible spectroscopy. This technique had been used in the past [2] at lower field strengths, so the goal of this LDRD was to extend these techniques to higher fields generated in larger pulsed-power machines. Since much spectroscopy work was being done on RITS in support of the x-ray radiography program [3], this seemed like a good platform to test these techniques. Once the techniques were demonstrated on RITS, they would then be implemented on Z. The project had three main parts, experimental work on RITS, experimental work on Z, and modeling/simulation work provided by the Electromagnetic Theory group in Org. 1652. As the project developed, changes were made, and the scope of the simulation work was reduced, in support of more experimental efforts. During the second year, the radiography R&D program on RITS stopped, causing a shift of resources over to Z. For the final year of the project, the focus was mainly experiments on Z. To that end, since December 2016, there have been 24 shots fielded on Z, on variety of different load hardware configurations. Prior to that, Ross Falcon (Org. 1683) fielded visible spectroscopy on 39 Z shots looking at different power flow regions.

As stated in the original proposal, the future of pulsed-power requires the efficient delivery of large currents (>25MA) to a variety of loads with small and predictable amounts of current loss. Right now on the Z machine, certain loads have up to 20% current losses, and the mechanisms causing these losses are not well understood [4]. This impacts several research programs including: dynamic materials, gas-puff z pinches, and MagLIF experiments. As stated, the causes of these current losses are not well known, but the present thought is that surface contaminants [5] (hydrocarbons and water vapor), outgassing of electrode materials, and/or non-

ideal geometries, which cause field enhancements and/or nulls, are the primary culprits. At present, the total current is measured upstream of the load using B-dot current monitors, which are compared with load current measurements, obtained by a variety of velocity-based techniques; however, no technique is presently available to measure current within the final feed section, where the potential for losses are the greatest (smallest A-K gaps and highest current densities). Optical spectroscopy allows an unintrusive means of measuring currents within very small (sub-millimeter) spatial regions, which are limited only by the optics used. This method takes advantage of the relationship between the magnetic field and enclosed current as expressed in the following equation (Ampere's Law) [6]:

$$B = \frac{\mu_o I}{2\pi r} \qquad (1-1)$$

The goal of these measurements is to help to validate plasma dynamics models in hybrid fluid/PIC codes. These codes are essential for building an understanding of the detailed physics involved in complex pulsed-power systems, as well as providing a platform for predictive capabilities of current loss and delivery in present and future pulsed-power machines.

1.2. Techniques

Visible spectroscopy covering the wavelength ranges from ~380nm to 700nm is very useful as an unintrusive means of investigating plasmas. Within these wavelengths, higher-level transitions of carbon, hydrogen, and oxygen are measured, which can provide information on temperature and plasma composition. Other elements have ground state transitions in the visible which can be very useful as dopants, for example Na I and Mg I. Within this wavelength range Doppler line shifts can be used to determine plasma velocities, and Zeeman splitting of lines can be used to measure magnetic fields in the range of a few Tesla up to ~300T. Stark broadening of lines can be used to measure plasma densities, and Stark shifts to measure magnetic fields (ex. Li I 6708Å).

One of the greatest advantages of working in the visible is the ease of operation. Standard optical fibers and conventional lens and mirrors can be used. Light can be transported either

through optical fiber or air without significant losses. This makes fielding visible spectroscopy much simpler than either ultraviolet or vacuum ultraviolet systems. There are limitations, in that stronger line emission can be measured in the uv and vacuum uv systems, with less continua. In the uv, there tends to be less Stark broadening which helps with other measurements such as Doppler or Zeeman. As one goes to shorter wavelengths, more ground state transitions of carbon, oxygen, and hydrogen are present, which increase signal strength, and allow for better determinations of plasma parameters. This LDRD concentrated on the visible region, but the hope is that for continuing research, looking at power flow on Z, efforts will be made to look into the uv and vacuum uv regions, to allow for greater data collection.

2. MODELING

One important part of this LDRD, and really one of the primary motivators for the experimental efforts on RITS and Z, was the development of computer models which could be used to predict plasma generation in the power flow regions on Z, using a first principles approach. Quite a bit of modeling has been done over the years using the LSP, hybrid fluid/PIC code developed by Voss Scientific [7], and from this work, high density plasmas have been observed to develop in the post-hole convolute regions [8] on Z as shown in figure 1 below [9].

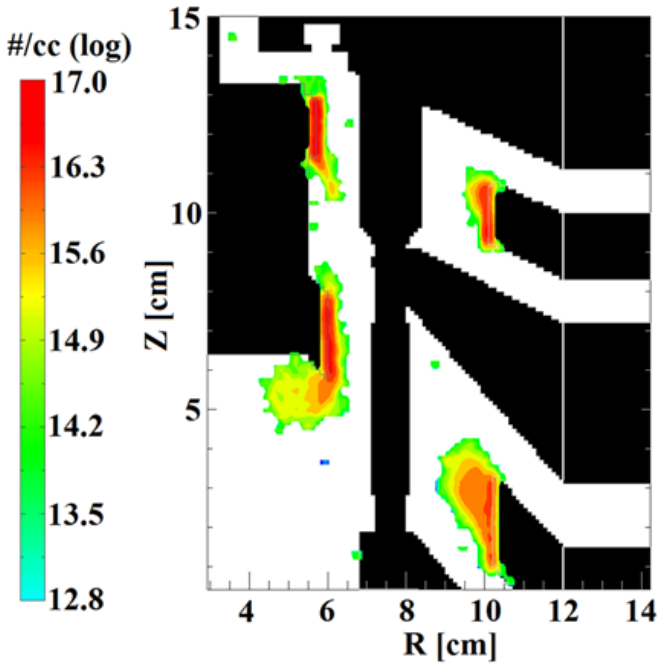

Figure 1. LSP simulation of the post-hole convolute region on Z.

This LDRD wanted to explore the possibility of using the EMPHASIS (ElectroMagnetics Physics AnalySIS) code developed in Org. 1352, to model plasmas in the Z power flow regions. EMPHASIS is an unstructured, finite element mesh, particle-in-cell (PIC) code [10].

To properly understand current loss on Z, one needs accurate modeling of plasma generation and neutral desorption from electrode surfaces. Several plasma emission models were studied as part of this LDRD, and are summarized in the table below.

Emission Model	Incident Particle	Secondary Particle	Thermal Dependence
Desorption (Hertz-Knudsen-Langmuir)(Sanford et.al.)	None	Neutral	Yes
Thermo-Field Emission (Murphy & Good)	None	Electron	Yes
Space Charge Limited Emission (limit of thermo-field emission for high voltage) (Shiffler)	None	Electron	No
Secondary Emission (Lin and Joy)	Electron	Electron	No
Secondary Emission (Raizer 1991)	Ion	Electron	No
Associative Desorption (Lieberman and Lichtenberg)	Ion/Neutral	Ion/Neutral	Yes
Sputtering (Langley)	Ion	Ion/Neutral	Weak

Table 1. Emission Models for EMPHASIS plasma simulations.

These models were used on both the anode and cathode side. The cathode models involve field and SCL electron emission, while the anode models include ion emission, which can be from stimulated or thermal desorption. Neutral desorption is accounted for as well. From these models, currents are calculated and compared with experimental results.

The Z convolute has been modeled in EMPHASIS using a realistic geometry from the SATIRE series (stainless steel wire array) [11]. The figure below shows the initial meshing in EMPHASIS used in these simulations. The mesh was generated with four levels of refinement: 1.0 mm, 0.5 mm, 0.25 mm, and 0.125 mm.

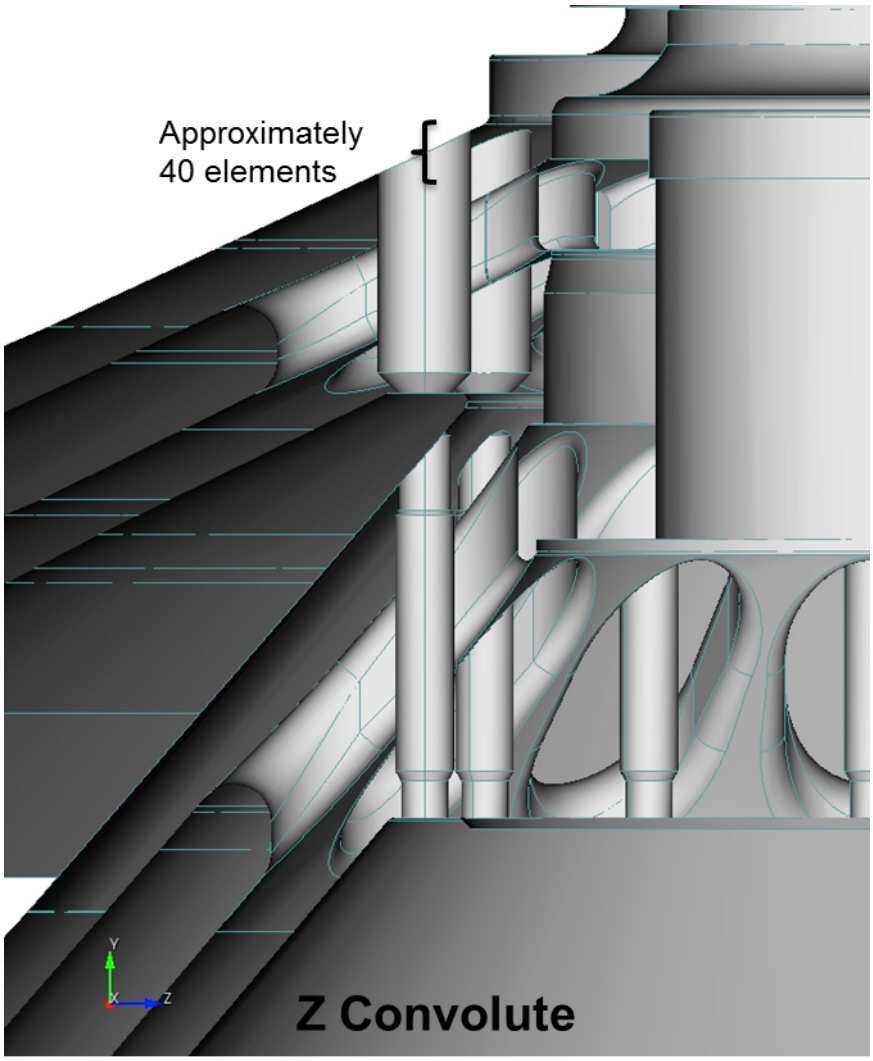

Figure 2. Z Convolute meshing in EMPHASIS.

From the simulations, field emission from the cathode shows little current loss, while field emission combined with secondary ion emission from the anode, along with a secondary yield that produces space charge limited ion emission from the anode, shows a lot of current loss (see figure 3). This latter model is the limiting case, i.e. the maximum amount of current loss that can occur if plasma formation only occurs at the surface; however, if neutrals are formed at either the cathode or the anode, then additional losses can occur. All of these results depend on having a representative model for the changing inductance on the load, as the inductance is quickly increasing during the simulation. These calculations show the importance of modeling both the electron and ion flow in the power flow region.

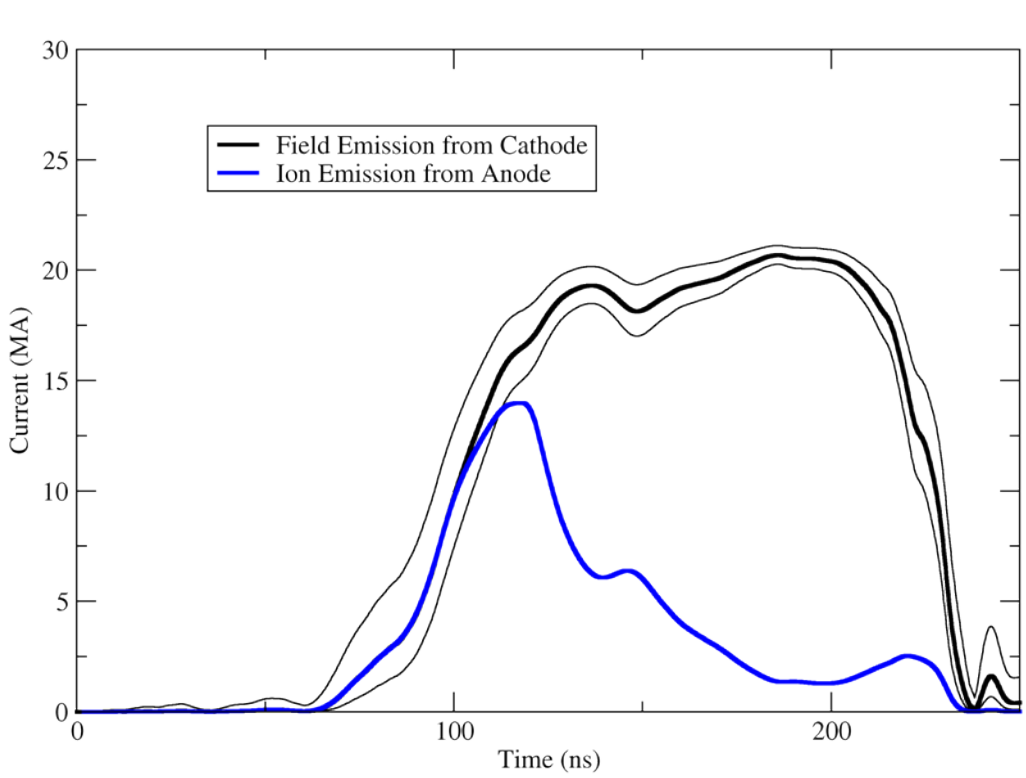

Figure 3. Simulated Z current profiles.

The simulations for this LDRD can be divided into two categories: first, applying the code (EMPHASIS) to power flow on Z, and second, improvements and verification of the code. The calculations were started using the Z MITL/post-hole convolute geometry for high inductance radiation sources (SATIRE series). Several proof of principal calculations demonstrated plasma formation and subsequence current loss; however, the Initial Graphics Exchange Specification (IGES) file was difficult to mesh. To further test the plasma generation models both the geometry and geometry specification were changed to a Magnetized Liner Inertial Fusion (MagLIF) [12] using STL (STereoLithography). Both of these geometries demonstrate current losses, and are important loads fielded on the Z accelerator; however, it was easier to show mesh convergence (solution verification) using the STL format with Cubit's mesh generator.

In summary, the models used for plasma formation in power flow of Z have been verified in a cylindrically symmetric co-axial geometry under surface conditions similar to the conditions found in the full MITL/post-hole geometry simulations discussed above. Surface models for plasma generation have been implemented in EMPHASIS for energy deposition time scales and

magnitudes that occur on Z. These models have been tested in large simulations of the post-hole convolute, as well as the final feed section, with symmetry planes to reduce the computational burden. The geometry used was for MagLIF hardware. The models that have been tested are: thermal desorption, thermo-field emission, secondary electron and ion emission, associative desorption, sputtering, and stimulated ion emission. These models were developed in EMPHASIS for other applications (mostly SGEMP) so several model inadequacies were discovered and repaired. There is still work to be done to integrate the multiple emission models together, as well as to implement a post-processing tool to get the spectral output from the simulations; however, this work is ongoing and will continue beyond this LDRD project.

3. RITS DIAGNOSTICS

3.1 Introduction

LDRD experiments were performed on the RITS-6 accelerator [13]. RITS (Radiographic Integrated Test Stand) is a large, pulsed-power accelerator located at Sandia National Laboratories in Tech. Area IV, Bldg. 970. The accelerator is a Marx-driven, inductive voltage adder (IVA), with six induction cavities surrounding a magnetically insulated transmission line (MITL). Depending on the configuration, the accelerator is capable of producing 5-11.5 MV electron beams with currents ranging from 120-200kA for a 70 nanosecond pulse duration. These parameters are suitable for driving a variety of pinched electron beam diodes that can be used as flash x-ray radiography sources [14].

One of the electron beam diodes studied extensively on RITS was the Self-Magnetic Pinch Diode (SMP) [15]. This diode consisted of a small, hollowed, cylindrical metal cathode facing a flat planar metal anode, with a vacuum gap of approximately one centimeter. With this geometry, an electron beam, produced at the tip of the cathode, is focused by its own azimuthal magnetic field to a few millimeters in diameter. The beam is incident onto a high atomic mass anode target, which generates high intensity bremsstrahlung x-rays to be used for flash x-ray radiography. Because of the intense nature of the electron beam, and the very high 10MA/cm^2 current densities, plasmas formed on the electrodes can migrate out into the A-K gap on the timescale of the pulse. Investigations were conducted to study these plasmas, and their role in the overall behavior/performance of the diode. As part of this LDRD project, the anode plasmas were investigated spectroscopically to determine the magnitude of the azimuthal magnetic field generated, and from this determine the local current distribution at the target.

3.2 Diagnostic Overview

Figure 4 shows the diagnostic layout in and around the RITS-6 test cell. For x-ray shielding, the test cell is surrounded by 2ft. thick concrete walls. Diagnostic lines of sight are drilled through these walls to allow direct optical access to the RITS vacuum chamber and the SMP diode. In addition to the optical diagnostics, the locations of several x-ray diagnostics are also shown in the figure. The optical diagnostics are positioned at three primary locations. The spectrometers are inside the main RITS-6 shielded screenroom, along with the Avalanche Photodiodes (APDs)

and data acquisition system (DAS). Next to the RITS screenroom, a smaller screenroom housed an NSTec Los Alamos Operations Generation IV optical streak camera [16]. This camera was used to image plasma motion in the diode along a 1D chord. In the northwest corner, another small screenbox contained either a spectrometer with direct imaging capability or a gated ICCD camera. All of the diagnostics were used in combination on the SMP diode, and below is a brief description of each.

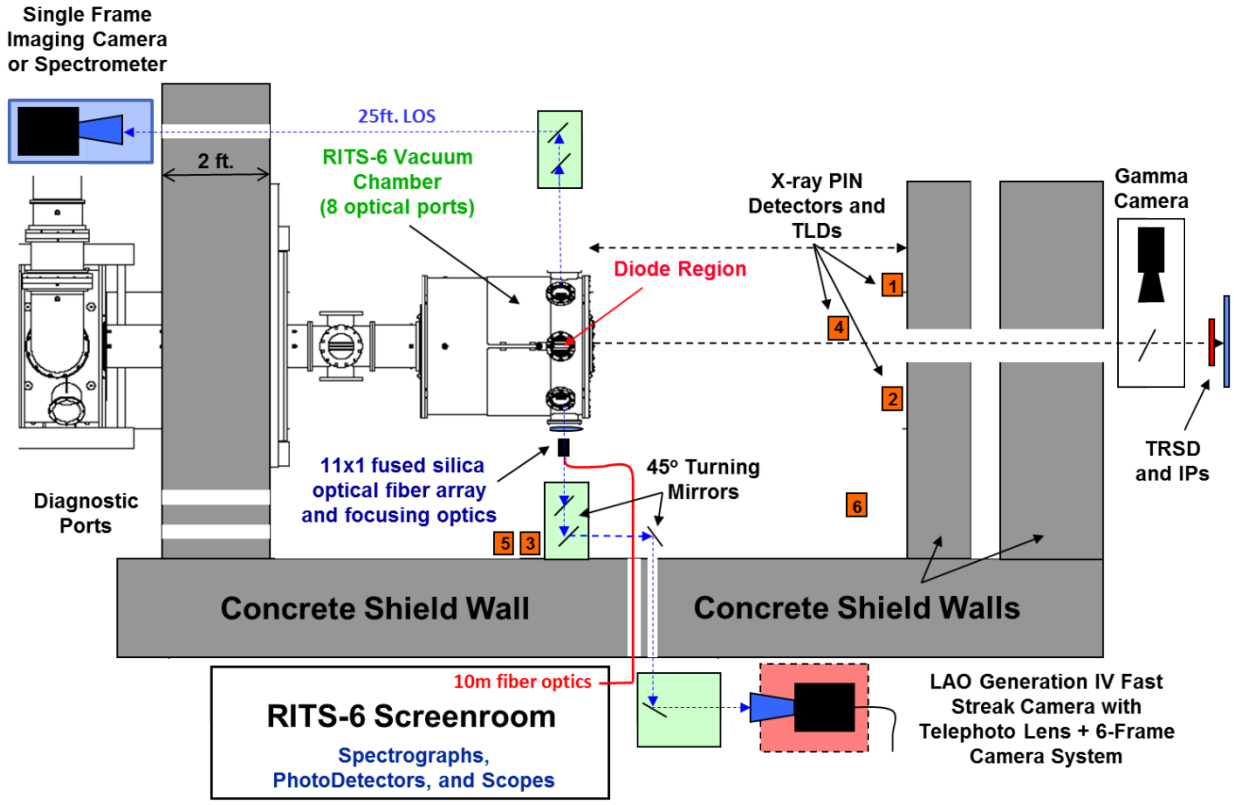

Figure 4. Diagnostic layout at RITS-6 test cell.

3.3 Spectra

The spectroscopy data were collected using both gated and streaked systems, on a variety of spectrometers, depending on the resolution and throughput required. The detectors were either a fast-gated (<7ns) Princeton Instruments PI-Max ICCD camera or an NSTec Los Alamos Operations Gen. IV streak camera coupled to a Spectral Instruments SI-800 CCD camera [17]. The majority of the data for this LDRD was collected using mulitfiber arrays, lens coupled to gated spectrometer systems. Several different spectrometers were used during the course of these experiments, with the majority of the gated spectra collected using either a 0.125m

Princeton Instruments model SP-2150 Czerny-Turner spectrometer [18] or a 0.32m Princeton Instruments IsoPlane model SCT-320 Schmidt-Czerny-Turner, aberration corrected spectrometer [19] (see figure 5). The SP-2150 was used with a 150g/mm grating and a 50 micron entrance slit width to give a resolution of 50 Å. The SCT-320 was used with a 2400g/mm grating and a 50 micron slit, and gave a resolution of 0.65 Å, which was need to be able to measure the magnetic field splitting.

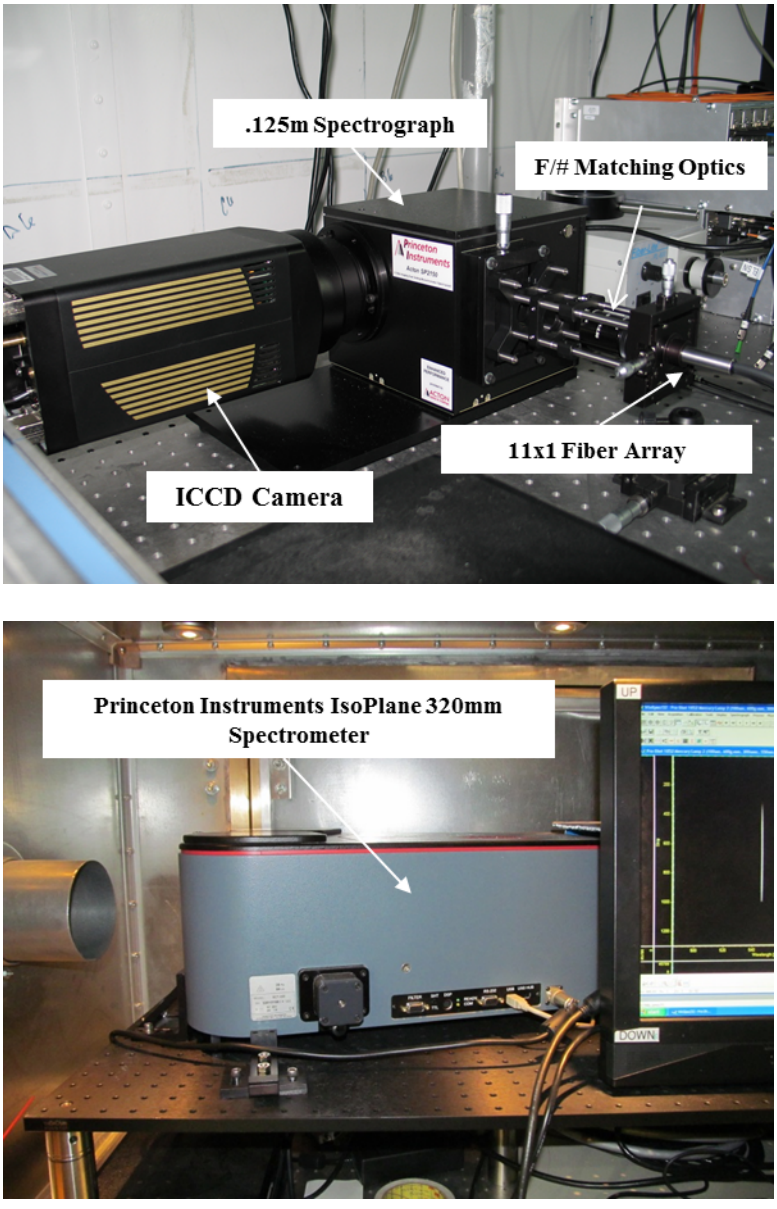

Figure 5. PI-Max ICCD camera with Princeton Instruments Spectrometers.

Steaked spectra were collected using either a 1 meter McPherson Model 2061 monochromator (S/N 70) with a 120x140mm, 150g/mm diffraction grating blazed at 500nm (figure 6), or a 0.5 meter Princeton Instruments SpectraPro 2500i Czerny-Tuner spectrometer (S/N 25580557) with a 150g/mm grating blazed at 500nm (15Å resolution with a 100 micron slitwidth) (figure 7). Both instruments were coupled to an NSTec Model L-CA-24 streak camera (S/N 220) [20] which was swept at 5ns/mm across a 50mm diameter streak tube mounted to a 40mm diameter microchannel plate (MCP) intensifier and recorded onto a 4K x 4K Spectral Instruments SI-800 CCD camera.

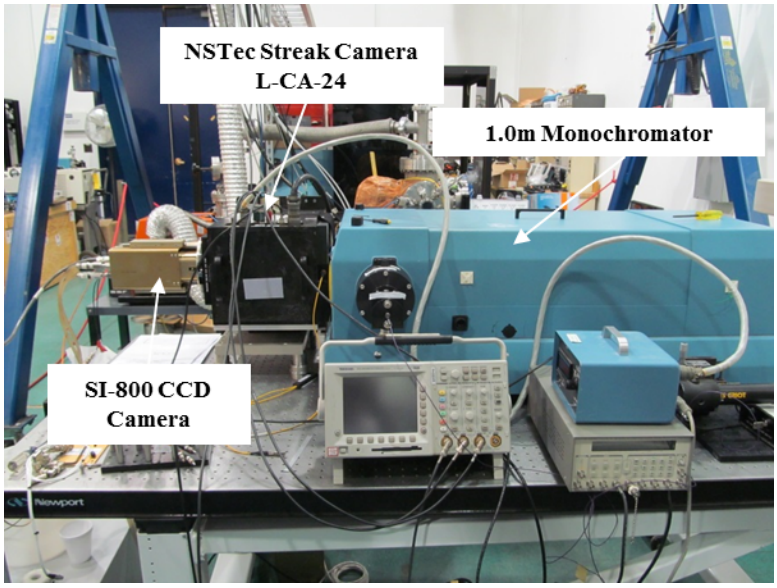

Figure 6. McPherson 1 meter monochromator with NSTec L-CA-24 streak camera.

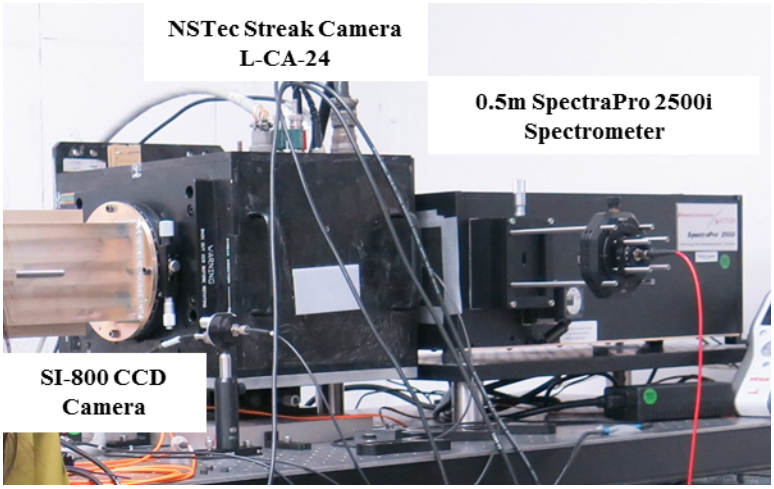

Figure 7. Princeton Instruments 0.5m spectrometer with NSTec L-CA-24 streak camera.

3.4 Imaging

The detector used for the gated spectra was a Princeton Instruments PI-Max ICCD camera (figure 8) [21]. This camera used a Generation III filmless GaAsP photocathode bonded to a 25mm diameter image intensifier with a P43 phosphor screen. The phosphor output tapers down to a 1340x1300 pixel, front-illuminated CCD, with 20 micron pixel sizes. This camera was typically gated at 10ns and had a peak quantum efficiency in the visible of >50%.

This same camera was also used to take 2D images of the plasma self-emission at the spectral gate time. These images were taken at the same time as the spectra, allowing for comparison of the plasma size and uniformity to that obtained from the multifiber array.

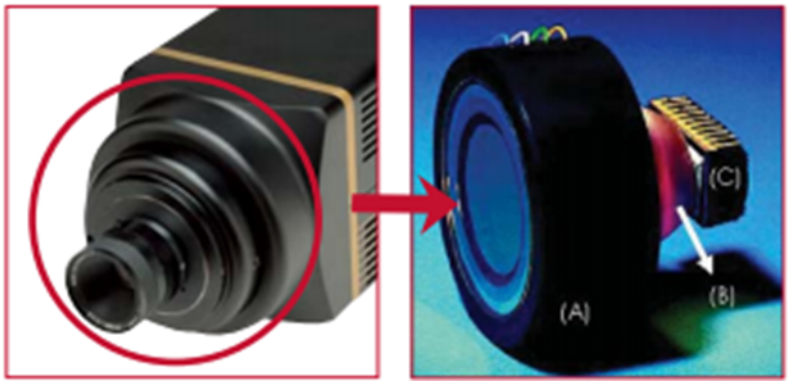

Figure 8. PI-Max ICCD camera showing image intensifier (A), fiber optic face-plate (B), and CCD (C).

Finally, a set of avalanche photodiodes (APDs) (figure 10) were used to look at plasma light emission in time and space. The NSTec Model H-EO-53 APDs [22] are built around the Hamamatu Model S5343 Silicon Photodiode (response curve shown below) [23]. These detectors have a responsivity of 0.33-20kV/W, with a 5% linearity, and a 1-50x gain factor. They have a quantum efficiency of 80% at 620nm and a photosensitivity of 0.42A/W at 620nm. These detectors proved very useful when studying plasma expansion and uniformity of lower density, wispy plasmas which propagate ahead of the more dense electrode plasmas.

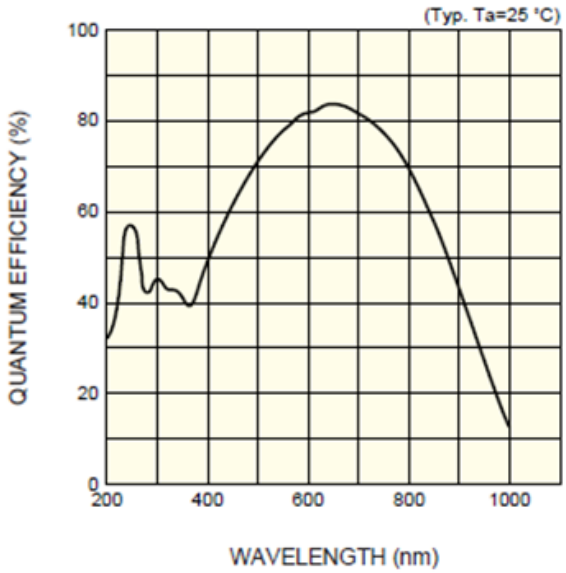

Figure 9. Response curve for the Hamamatu Model S5343 Si Photodiode.

Figure 10. NSTec Model H-EO-53 Avalanche Photodiodes.

Finally, we took some multiframe images of the 2D plasma evolution in time using a Photek Ultra8 camera system (figure 11) [24]. The Ultra8 camera uses a 40mm diameter, 8-way segmented, GenII intensifier which reads out onto a single 2Kx2K CCD array, with individual frames being 650x650 pixels each. The camera is capable of 2ns minimum exposures with any prescribed delay between frames. This camera proved useful in measuring plasma expansion rates and uniformity of the more dense electrode plasmas (see figure 27).

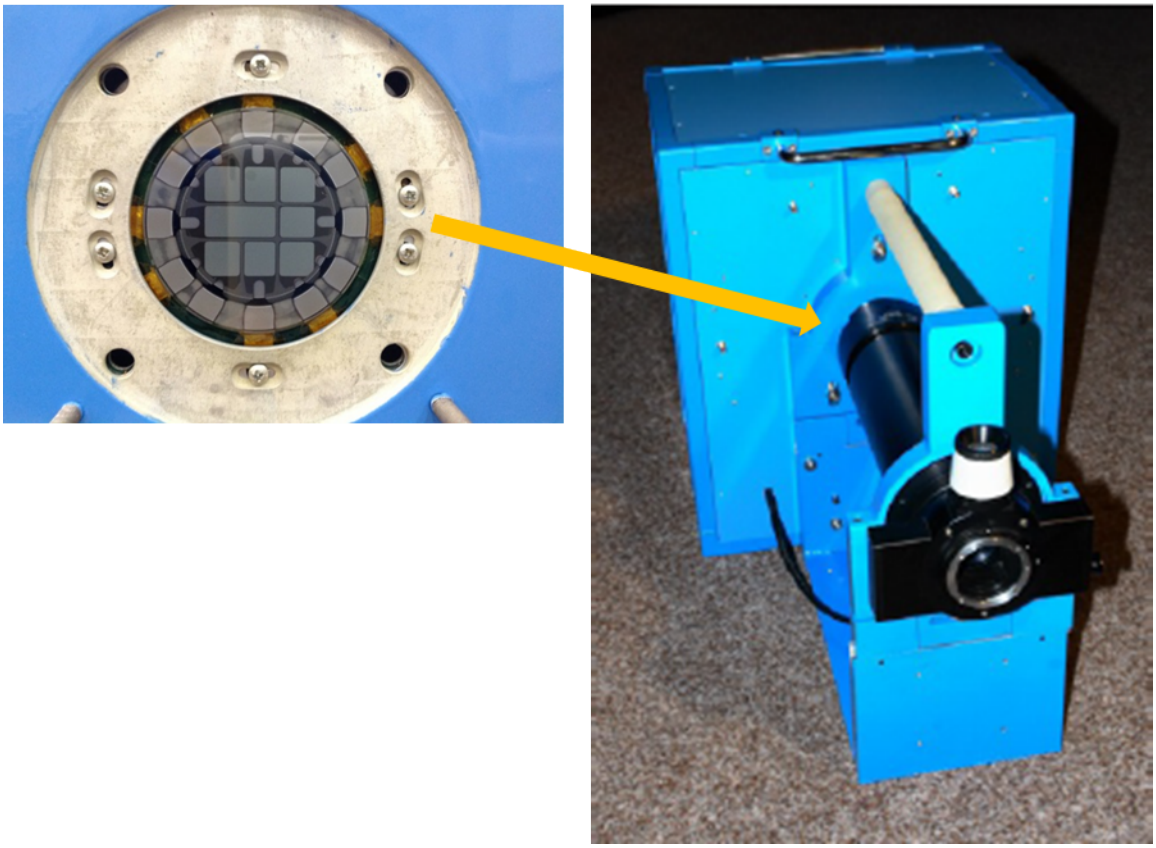

Figure 11. Photek Ultra8 Multiframe, Fast-Gated Camera System.

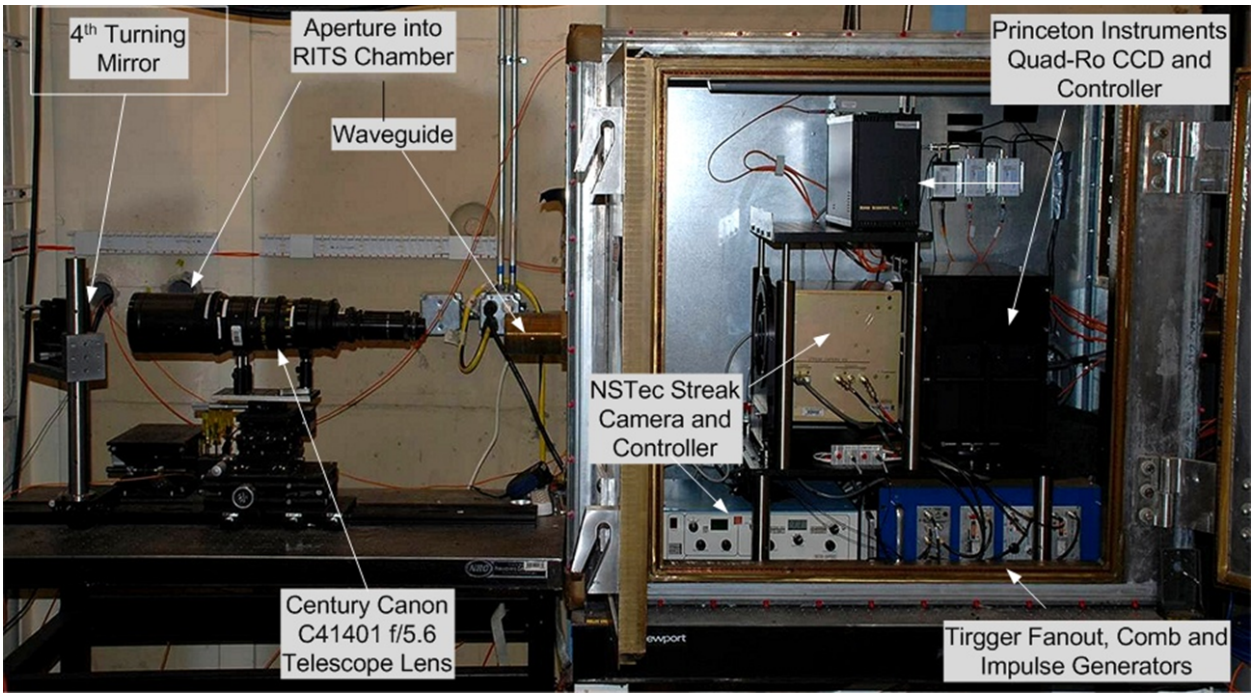

Figure 12. NSTec Los Alamos Operations, Gen. IV Optical Streak Camera setup on RITS.

Finally, 1D plasma imaging was done using an NSTec LAO Generation IV Optical Streak camera (S/N 678) [16]. This camera imaged a 1D chord showing either axial or radial electrode plasma expansion in time, depending on the setup. These images in conjunction with the 2D single frame images were used to construct the electrode plasma geometry that was then used to unfold the spectral data, i.e. the line of sight plasma volume. This camera used a large-format Photonis streak tube with a peak QE of 16% at 475nm. The streak tube was coupled to 50mm x 50mm Princeton Instruments Quad-Ro CCD camera (S/N 2111020009) with 24 micron pixel sizes [25].

3.5 Optics

Light was collected from the SMP diode using a using a 50mm, 150mm focal length, glass achromat (Edmund Optics Part #49-285). This optic was positioned outside of the RITS vacuum chamber, looking in through a glass window (Edmund Optics Part # 43-894). The fiber array was positioned so that it imaged light from a focus at the center of the diode, 31cm away. The fiber array consisted of either 100 or 200 micron diameter Polymico FVP, high –OH, silica, step-index fibers [26]. These fibers have a numerical aperture of 0.22, giving a 25.4 degree acceptance cone. There was a demagnification of 5x from the imaged plasma light to the collection fiber outside the chamber, resulting in a collection area of 1mm or 0.5mm, respectively, in diameter through the plasma volume. Figure 13 shows a photo of the hardware attached to the RITS vacuum chamber and Figure 14 provides a drawing of the optics.

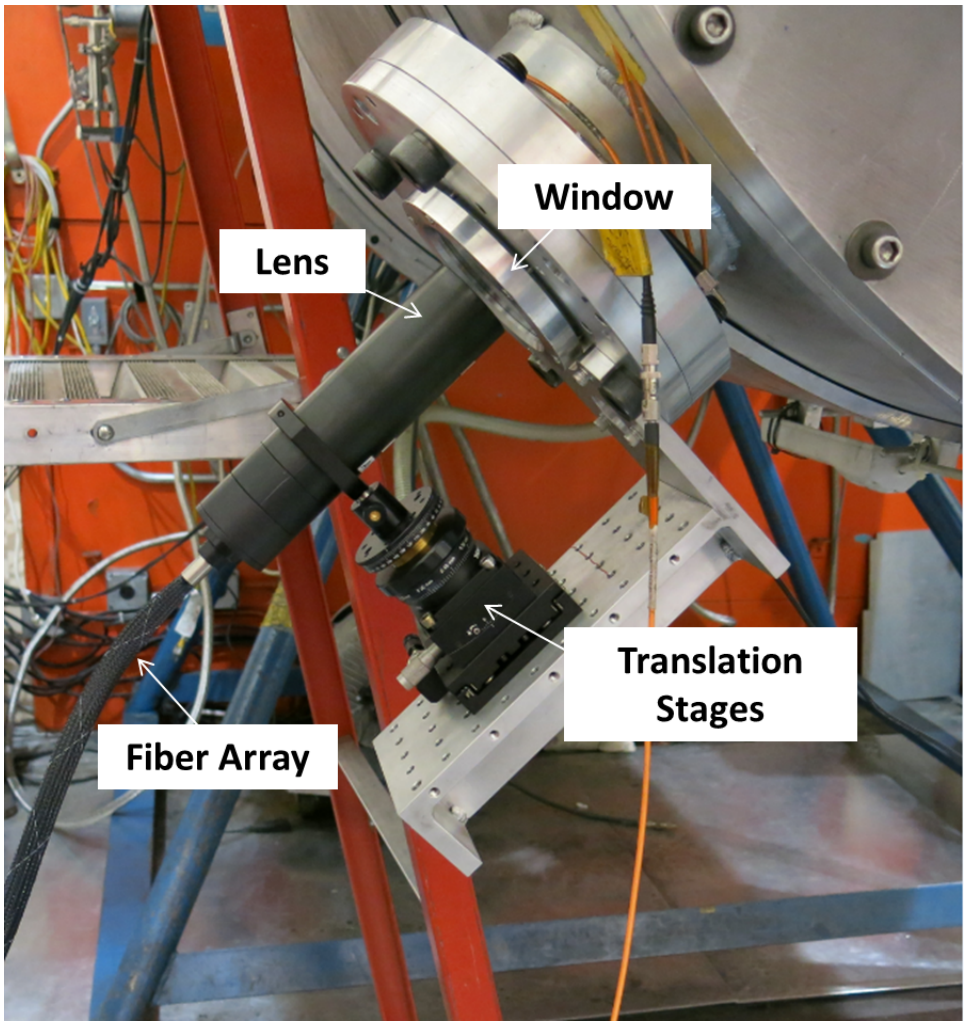

Figure 13. Fiber optic mounted on RITS vacuum chamber.

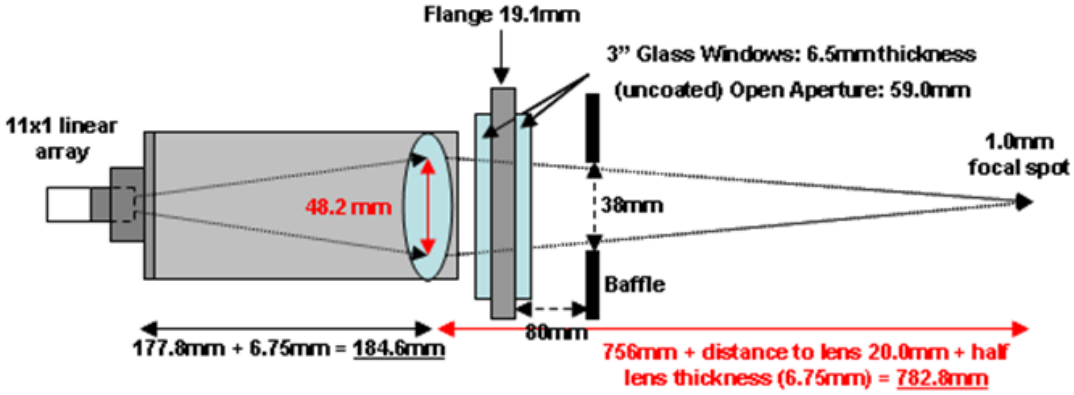

Figure 14. Illustration of the optics used on RITS for imaging plasmas.

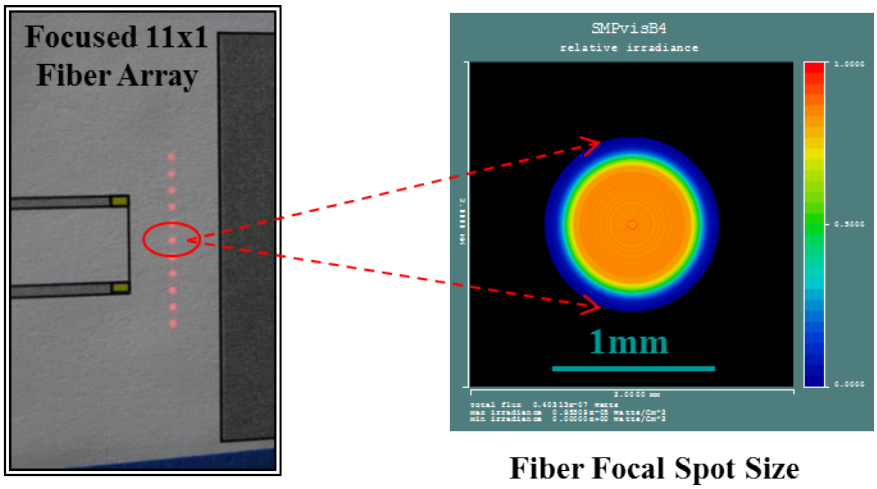

Figure 15. Image of single focused fiber array relative to the A-K gap on the SMP diode.

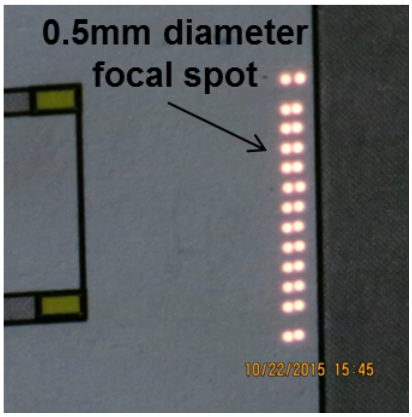

Figure 16. Image of double focused fiber array relative to the A-K gap on the SMP diode.

Light was transmitted through 10 meters of optical fiber into the RITS screenroom, where it was reimaged using an f/# matching double achromatic pair onto the slit of the spectrometer. Figure 17 shows how the spectra looked for both the 200 micron, 11x1 array, and the 100 micron, 13x2 double array, when collected by the PI-Max ICCD camera (1340 x 1300 pixel image). Each line represents one fiber in the array, looking at a specific spatial location at the diode. Using this technique, we were able to observe spectral changes with distance within the diode for a single 10 nanosecond gate time. When combined with the streaked camera, we were then able to observe both time and space resolved spectra on the same shot. The spectra in figure 17 were taken using a continuous white light source (the bottom axis is wavelength).

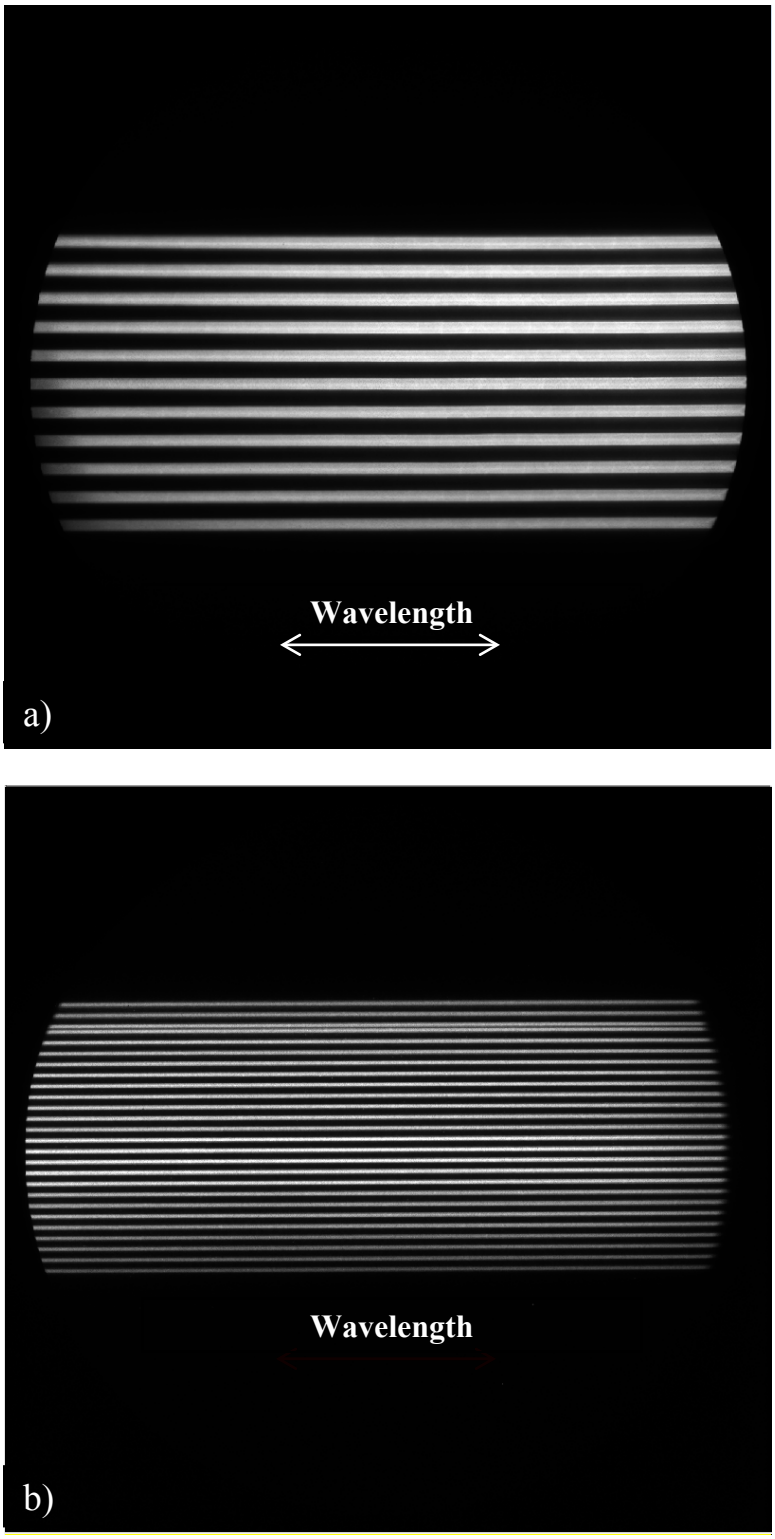

Figure 17. a).200 micron, single fiber array spectral output imaged on PI-Max ICCD. b) 100 micron, double array spectral output imaged on PI-Max ICCD.

4. DENSITY AND TEMPERATURE MEASUREMENTS ON RITS

4.1 Introduction

Analyzing spectra obtained from the SMP diode can be challenging. Lineshapes are integrated across a line of sight through plasma, which often have significant density and temperature gradients, in addition, these lineshapes are a convolution of several different broadening mechanisms, each of which must be properly taken into account. On top of this, the spectra are rapidly changing on a timescale that is comparable to that of the spectral gate time. Often these signals are on top of strong continuum backgrounds, giving poor signal to noise characteristics. Besides this, several different models and approximations exist for analyzing plasma parameters from spectral lineshapes, which make interpreting the data very difficult. For this LDRD, we employed the most up-to-date modelling available to calculate both plasma parameters as well as electric and magnetic fields from spectral lineshapes obtained from the SMP diode. The data was analyzed using time-dependent, collisional radiative (CR), and radiation transport calculations. The majority of these calculations were done by Professor Yitzhak Maron and his group at the Weizmann Institute in Rehovot, Israel. In some instances, calculations and approximations were also obtained using PrismSpect or tables from the literature, and where applicable, these values have been given as well. In general, we have tried to use the most current methods for determining the fields.

4.2 Plasma Species and Charge States

Before the analyses can be done, the spectra must be collected. On RITS we measured spectra using the techniques described in the previous section. Typical spectra for the SMP diode contained lines from electrode materials and contaminants such as water vapor and hydrocarbons. These contaminant species were used for the majority of the measurements made; however, additional species (dopants) were added to the system on some shots, to either take advantage of a particular line for a certain measurement (ex. Li I 6708A), or to try and isolate the location from where the line(s) were originating. Using the inherent lines in the system was convenient, but it didn't allow for precise determinations of the locations of the plasmas. Still, we were still able to derive accurate descriptions of the plasma based on the different charge states and densities observed using multiple chords through the plasma on a single shot. This

combined with optical imaging data obtained from framing cameras of the plasma position and shape in time, allowed a fairly accurate picture of the plasma to be revealed.

From the spectra obtained on the SMP diode, it was found that several ionization states were present. For example, on the same spectrum we could measure neutral hydrogen and carbon +3. This was due to variations in temperatures that were being integrated along the chordal lines of site. These differences were interpreted as different regions within the plasma, extending in rings outward from the axis (see figure 18), with the central portion being a hotter, denser region,

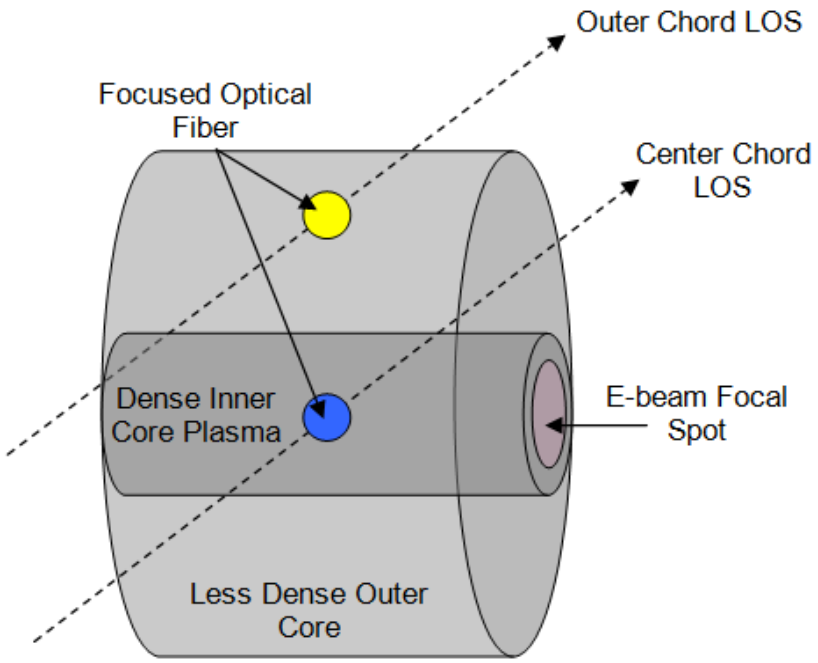

Figure 18. Representation of different plasma regions within the SMP diode.

followed by progressively cooler outer rings, decreasing in charge states. This complicates the analyses somewhat as lineshapes often required multiple densities, temperatures, and/or fields to be fit properly. On average, the charge state of the SMP plasma was found to be +2.5 +/- 0.5. Much of the spectral analyses for both density and temperature were done using C IV, C III, or Al III lines. Except for close to the axis where only continua were present, lines would typically be seen extending outward up to a radius of 10mm.

4.3. Electron Temperature:

The two main parameters that need to be determined to accurately describe the conditions within the plasma are the electron density and temperature. Both of these parameters were determined as part of this LDRD for the SMP diode plasma, and the methods used to obtain these values are described herein, starting with the electron temperature. Electron temperatures can be determined by comparing relative line intensities from the same or subsequent ionization states. This is based upon the assumption that the plasma is optically thin (visible light can be transmitted through it), the electrons can be described by a Maxwell-Boltzmann distribution, and the transition coefficients and energy levels are accurately known. For a series of lines, a Boltzmann plot can be generated, the slope of which gives the inverse of the electron temperature ($1/kT_e$). For only two lines, electron temperature can be determined from a direct ratio of the line intensities using the following relationship [27]:

$$\frac{I_{ki}}{I_{nm}} = \frac{g_k A_{ki} \lambda_{nm}}{g_n A_{nm} \lambda_{ki}} \exp\left(\frac{-(E_k - E_n)}{kT_e}\right) \tag{4-1}$$

where n = upper energy level and m = lower energy level of the second line transition. For the best results, it is important that the transition probabilities are accurately known and that the separation between the upper energy levels of the two lines measured is as large as possible, preferably >0.5 eV.

Another useful method to calculate the electron temperature involves the ratio of line intensities from subsequent ionization states of an element [28] as shown below:

$$\frac{I_n^z}{I_k^{z-1}} = \frac{4}{N_e}\left(\frac{m_e kT}{2\pi\hbar^2}\right)^{\frac{3}{2}} \frac{A_{nm}\lambda_{ki} g_n^z}{A_{ki}\lambda_{nm} g_k^{z-1}} \exp\left(\frac{-\left(E_n^z + E_\infty - E_k^{z-1} - \Delta E_\infty\right)}{kT_e}\right) \tag{4-2}$$

where, n is the upper energy level of the higher ionization state and k is the upper energy level of the lower ionization state. This ratio can be used to determine the electron temperature (T_e) based upon the emission intensities of two lines from subsequent ionization states of the same element. It is important to note that knowledge of the electron density (N_e) is required to use this

equation. These equations are derived assuming the plasma is in Local Thermodynamic Equilibrium (LTE) [29]. Unfortunately, the LTE approximation is not a good assumption for the plasma conditions in the SMP diode, so instead, temperature determinations were made using a collisional-radiative (CR) model [30] such as that found in the PrismSPECT code [31]. In order to determine the electron temperatures, CIV and C III lines are fit with Voigt profiles [32], and the ratio of the two lines are compared in PrismSPECT, using a non-LTE, optically thin model for a pure carbon plasma. Since electron density measurements from the CIII Stark-broadened linewidths are difficult to obtain, the temperature ratio here assumes a uniform electron density along a chord, based on just the C IV linewidths. Figure 18 shows the electron temperatures obtained using this method. The electron temperatures range from about 5.6eV-6.3eV, and increase approximately linearly towards the beam axis.

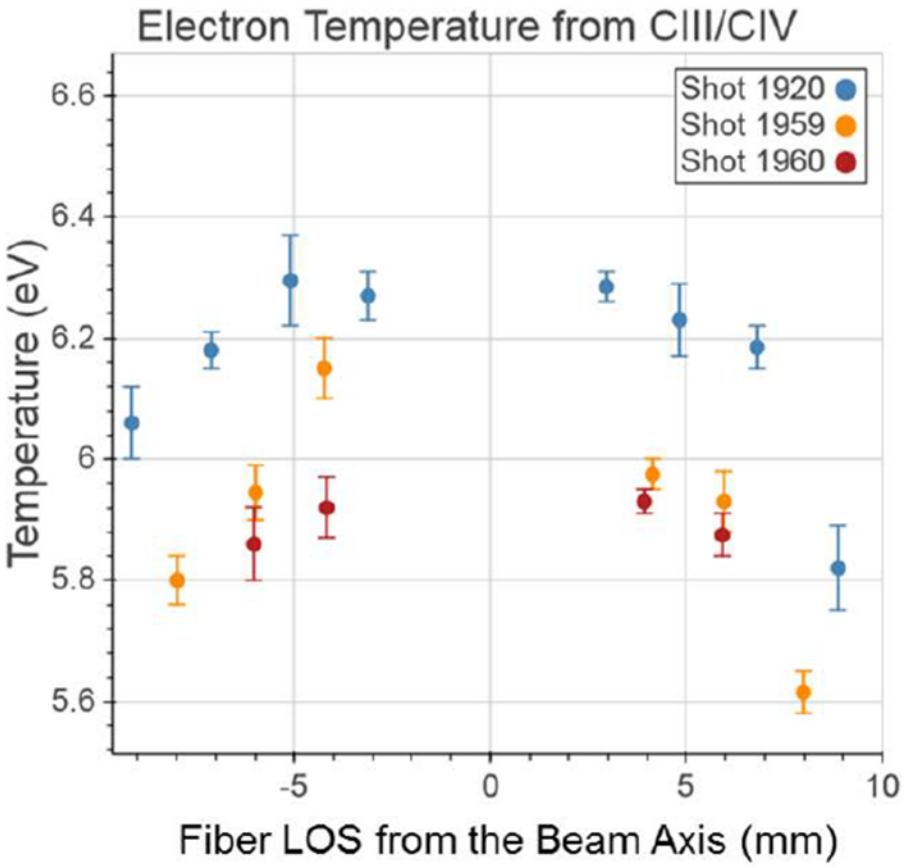

Figure 19. Plot of electron temperature versus radius in the SMP diode, as determined from CIII/CIV line ratios.

4.4. Electron Density:

In order to determine magnetic fields from Zeeman splitting of spectral lines, the plasma densities and temperatures must be known. Electron densities were determined from Stark broadening of spectral lineshapes. In particular, due to the integrated lines of sight, several different lines were used to determine the electron densities. Several models have been proposed for determining electron densities from Stark widths, with varying degrees of accuracy, depending on the plasma conditions. The most basic version is the semi-classical approximation [29], followed by the semi-empirical [33], and the modified semi-empirical [34] There are also more complex models which take into account ion motion [35].

Similar to the electron temperature determinations, the degree of the broadening depends on the specific transition being measured, the local plasma conditions, and the models or approximations used, thus variations in the calculated densities can occur. For this work, densities were determined from hydrogen, carbon, and aluminum lines. Hydrogen, the simplest and most studied element, is often used for determining electron densities; however, being a neutral line, it is often not present in higher charge state plasmas, such as those close to the beam axis (<6mm) on RITS. In that case, other lines such as C IV and Al III were used, for which the data is more limited and the errors larger.

For the hydrogen alpha line (6563Å), linewidths have been calculated using Griem's standard theory [29]. This theory assumes an electron impact approximation and a quasistatic ion field approximation. The electrons are assumed to have a Maxwellian distribution of energies. Griem's tabulations are assumed to be accurate to within ~10%. The electron density is weakly dependent on temperature, but within the range of these calculations, that error is only on the order of ~5%. Figure 20 shows an experimental lineout of the H-alpha line along with the neighboring CII lines (6578Å and 6583Å). The lines are fit with Voigt profiles, from which the Gaussian instrumental width is deconvoluted. Since these spectra are integrated along a chord which traverses several density regions, the lineshapes are fit using two profiles, one for the narrower central peak and one for the broader wings.

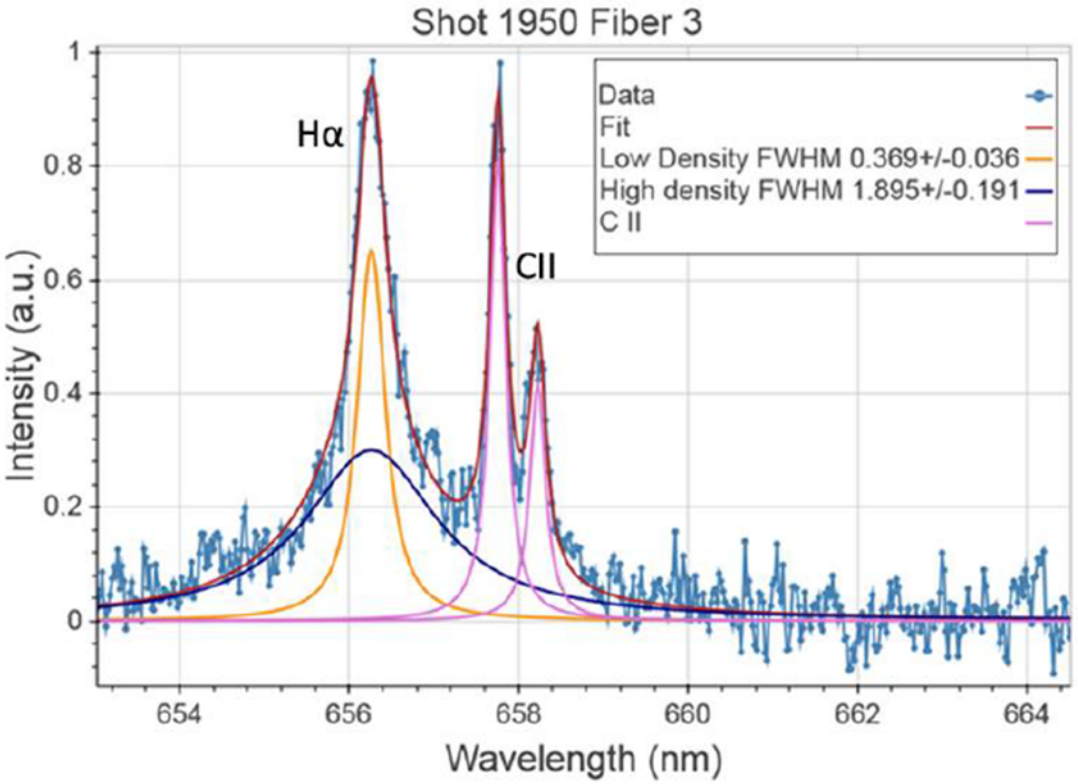

Figure 20. Lineshape fits for the H-alpha and C II transitions.

For the C II lines, the Stark widths (FWHM) were measured to be 2.0Å and 4.5Å respectively, which correspond to electron densities of 2.0×10^{16} cm^{-3} and 4.6×10^{16} cm^{-3}. Figure 21 shows a plot of electron density versus radial position for the hydrogen alpha and C II lines for three shots for both the low and high density components. As can be seen, the lower densities obtained from the hydrogen alpha and C II lines are in the low 10^{16} cm^{-3} range, and remain relatively constant with distance from the axis, while the higher density component of the H-alpha line ranges from the low to mid 10^{17} cm^{-3}, increasing approximately linearly towards the axis. This suggests that the lower density component is from outside the 10mm radius covered by the fiber array, while the higher density component is from within the 10mm radius, and thus more accurately represents the true density at each radial location.

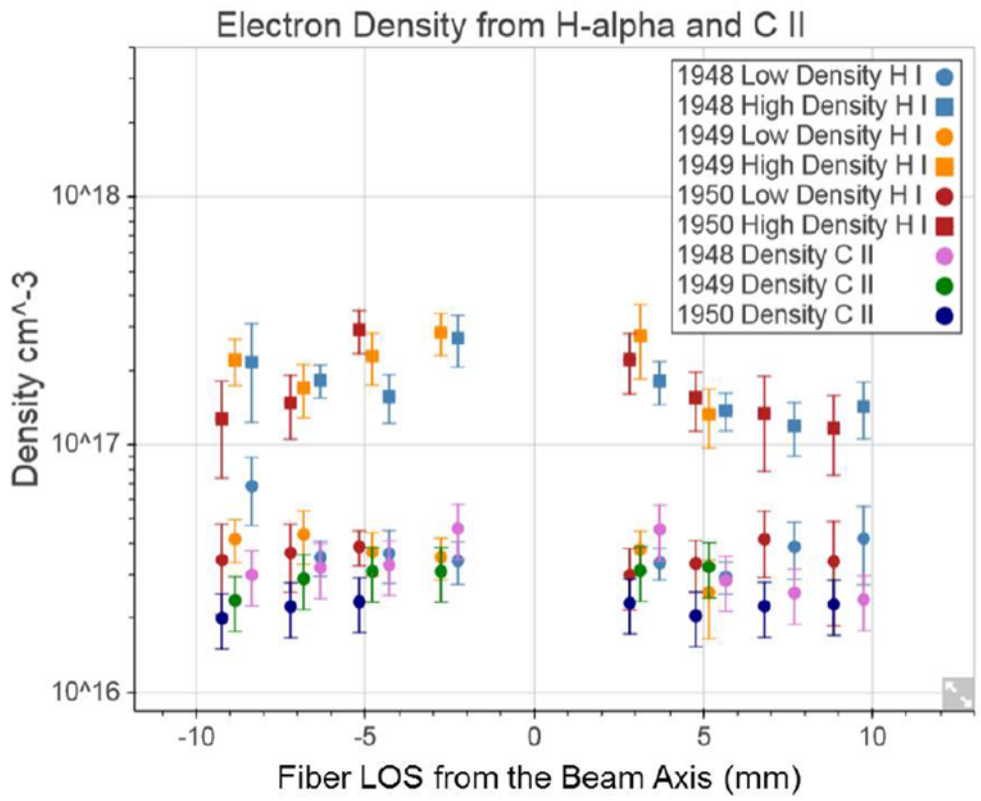

Figure 21. Electron density variations versus radius for both the high and low density components of the SMP diode plasma.

Temperatures for this lower density region can be inferred from CII/CIII line ratios which give an upper bound on the temperature of ~5 eV, with likely temperatures in the 3-4 eV range. Since there is a cooler, less dense outer plasma region, surrounding a more dense hotter plasma region, and the Zeeman measurements were taken from the C IV line, located within the hotter inner region, the electron densities obtained from the H-alpha and CII lineshapes, cannot be used in the calculations, as these would result in artificially higher calculated fields, so the electron densities have to be obtained from the C IV lines themselves.

Figure 22 shows two lineouts for the C IV doublet lines along with lineshape fits. Only the inner fiber (3mm radius) requires a two density fit, like that described earlier for the H-alpha line, while the further line (4mm radius) does not.

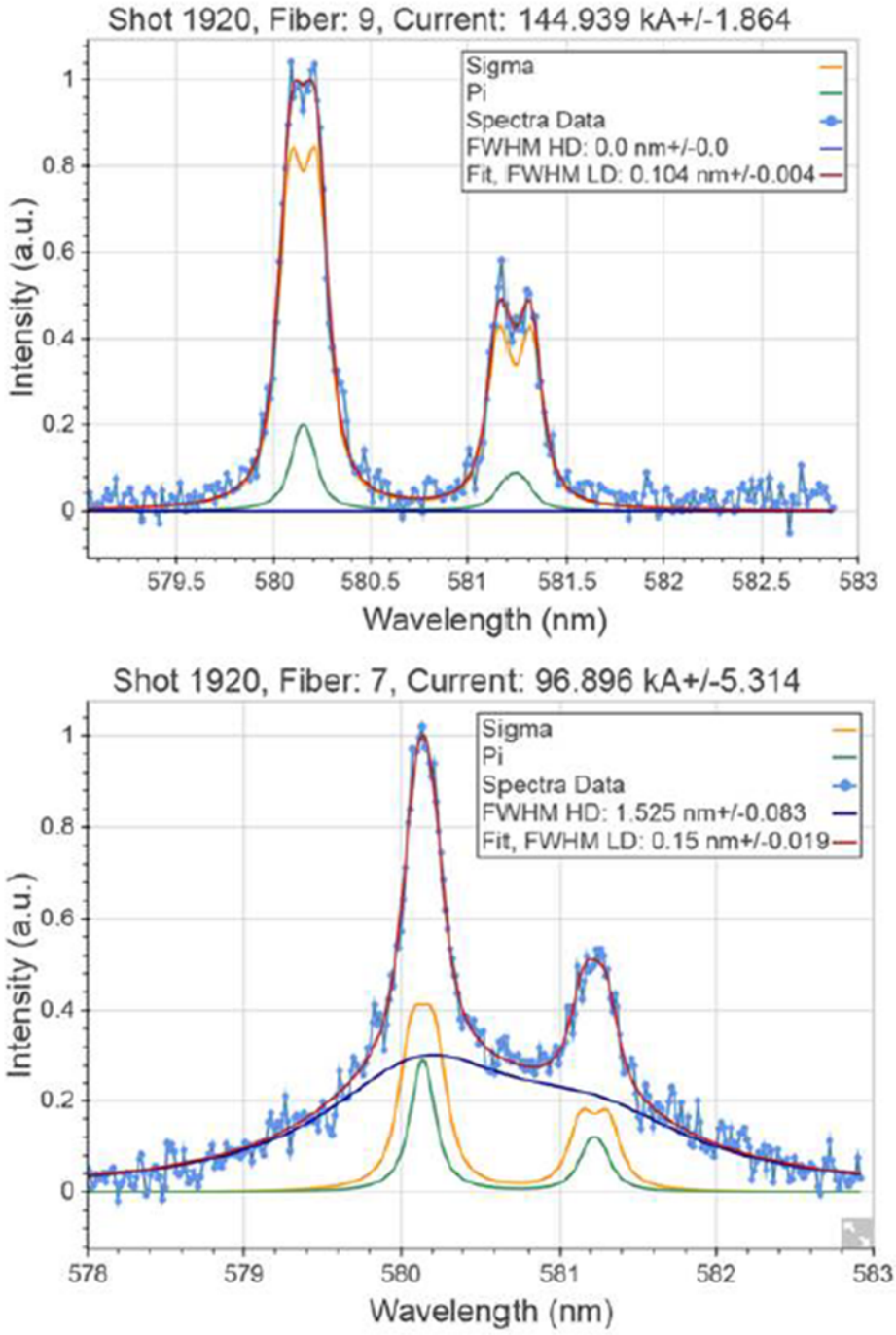

Figure 22. Spectral lineouts of the C IV (5801Å and 5812Å) doublet.

The electron density is determined from the Lorentzian component of the Voigt profiles. Figure 23 shows the results for 5 different shots. The lower density component is in the low to mid-10^{17} cm^{-3} (similar to the high density component of the H-alpha lines), while the higher density

component is approximately an order of magnitude larger in the low-10^{18} cm^{-3} range. The line widths were determined by Prof. Yitzhak Maron and his group at the Weizmann Institute.

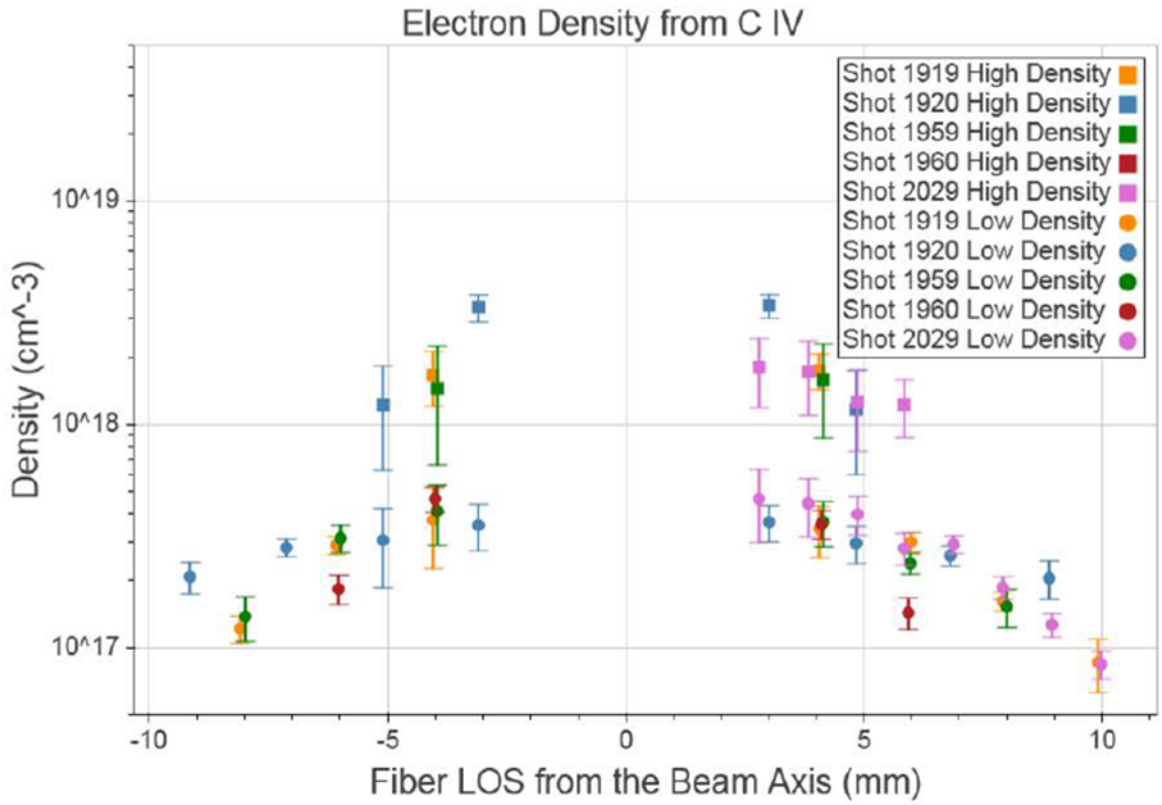

Figure 23. Electron densities versus radius determined from CIV linewidths.

The validity of this two density approach was experimentally verified using a double array (see figures 16 and 17) which had 100 micron diameter fibers that collected light over a 0.5mm spatial extent. This allowed two fibers to cover the axial distance that a single fiber had before. Figure 24 shows the effect of this fiber separation in the raw spectra for Shot 2028, which was an aluminum coated solid target (no foil).

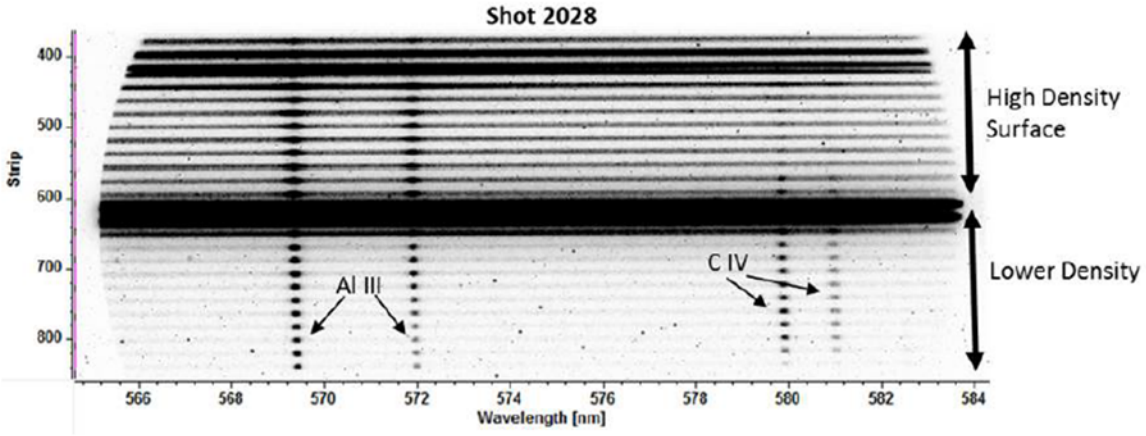

Figure 24. Spectral image of the double fiber array, showing the higher and lower density regions at the anode surface.

The spectra show both the Al III lines and the C IV lines; however, the inner array (closer to the surface), clearly shows greater continua and broader lines (also weaker C IV intensities). Figure 25 gives lineouts for two adjacent fibers located 3.5 mm from the axis, with the top lineout (fiber 5) being the closest to the surface.

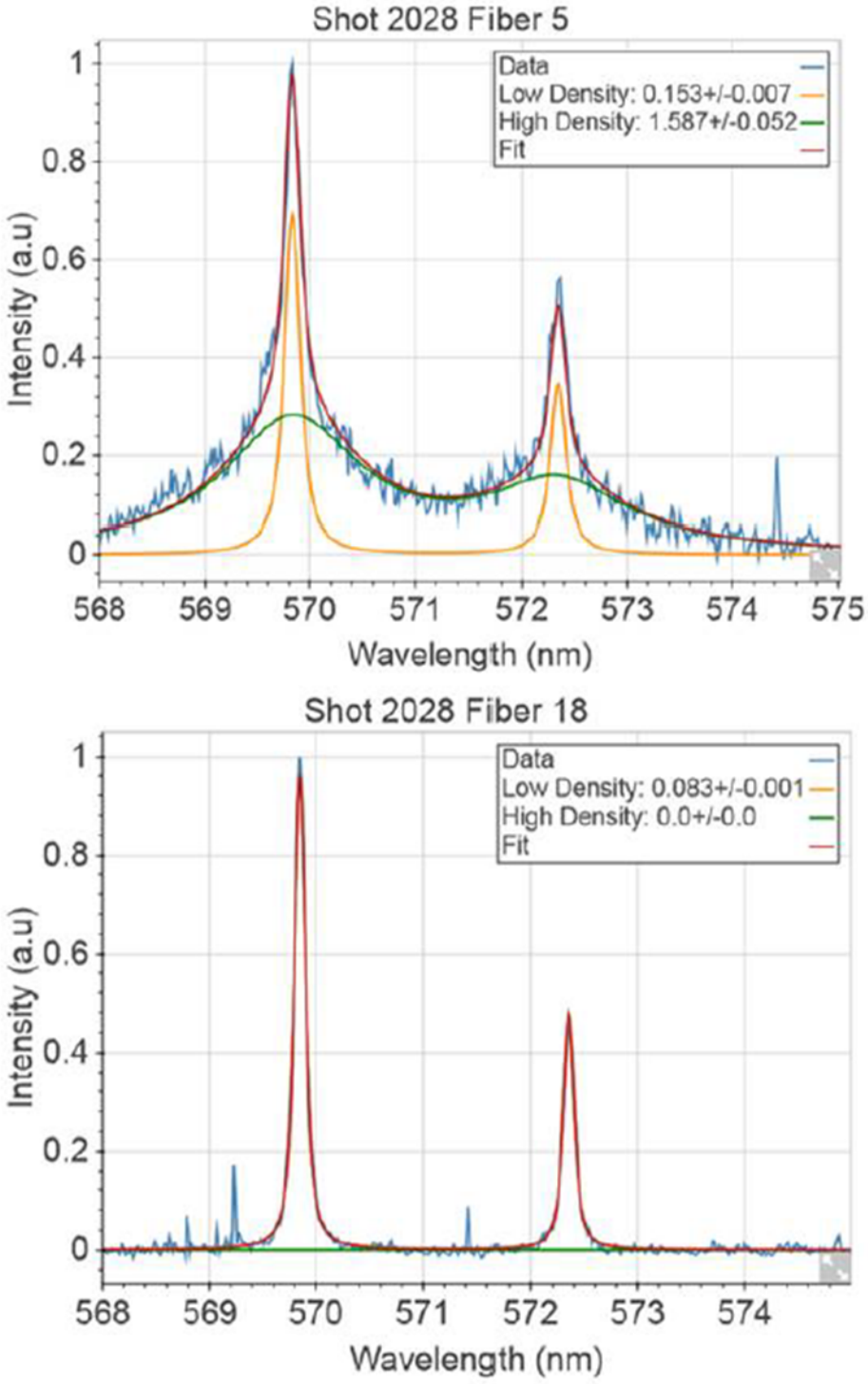

Figure 25. Experimental lineouts and fits of the C IV doublet for adjacent fibers in the double fiber array.

Using the calculations done at the Weizmann, the electron densities for the Al III lines and C IV lines are given in figure 26 below.

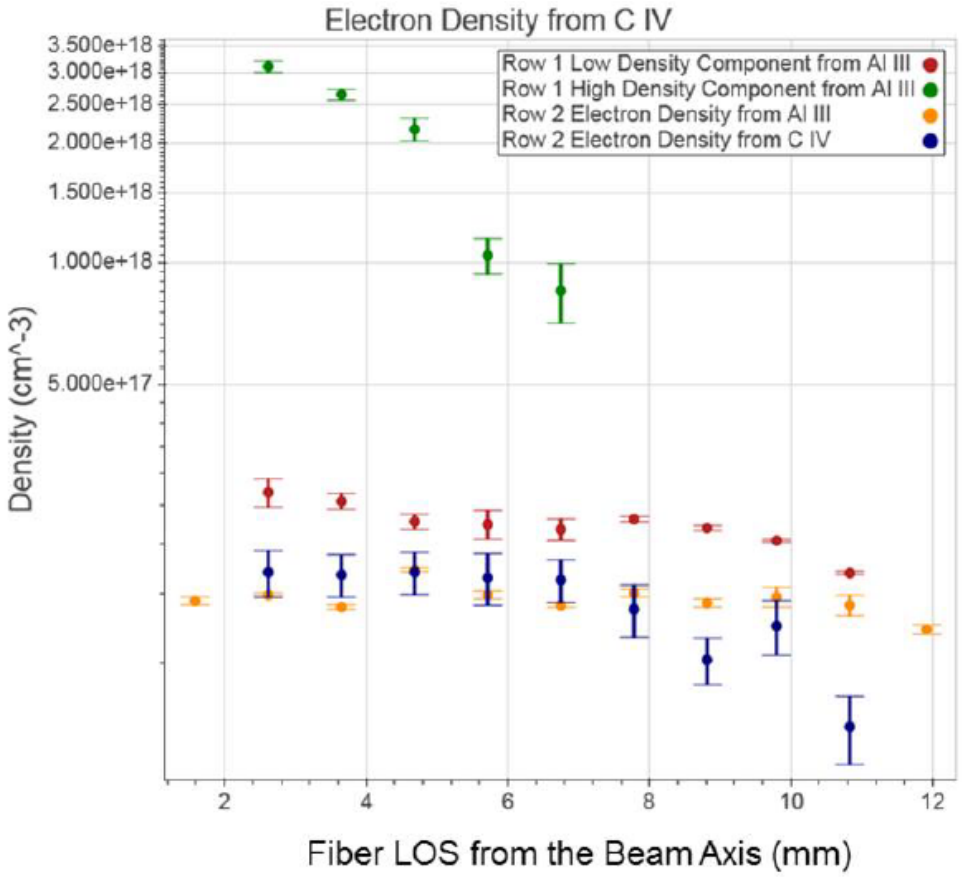

Figure 26. Electron density versus radius determined from the C IV and Al III lines from the double array showing higher and lower density regimes at the anode surface.

Within a radius of 8 mm from the axis, the electron densities calculated from the Al III and C IV lineshapes on the outer array (row 2) range from 2-3 x10^{17} cm^{-3}, suggesting the two lines are from similar locations. The electron density from C IV then begins to decrease after 8mm, while the Al III densities remain relatively constant. Spectra from the outer array (row 2) show splitting on the C IV lines, particularly at radii greater than 8 mm, while line splitting is not visible on the Al III lines for this shot, except at radii greater than 9.5 mm, most likely because the Stark width of Al III is about 40% larger than that for C IV, and thus masks any splitting. Consequently, an external magnetic field is included in the C IV fits, but not the Al III fits. However, as the density and therefore Stark width decreases, Zeeman splitting forms a larger

fraction of the total line width. By using the current estimates from C IV line splitting on the outer fibers and applying it to the Al III doublet, the electron density calculated from the two lines becomes nearly identical (6.7×10^{16} cm^{-3} for Al III and 6.9×10^{16} cm^{-3} for C IV), indicating they are likely from the same location. Additionally, the C III transition at 5696 Å is coincident with that of the Al III 3/2-1/2 transition, thus the carbon line is most likely adding to the Al III doublet, causing the ratio to be greater than 2 at radii larger than 7 mm. C III would also add to the Al III 3/2-1/2 transition, leading to a larger Lorentizian width.

4.5. Summary

Electron densities estimated from H-alpha are between 2-4 x 10^{16} cm^{-3} for the low density component and 1-3 x10^{17} cm^{-3} for the high density component, while for C IV, the low density component is 1-4 x 10^{17} cm^{-3} and 1-4x10^{18} cm^{-3}, for the high density component, and while the high density component is required to reduce all of the H-alpha lines (all radii), it is only need for C IV lines at radii less than 5-6 mm. Therefore, it is likely that the H-alpha line is located further from the axis than the CIV and Al III lines, with some overlap between the higher density portion of the H-alpha and the lower density portion of the C IV. In conclusion, the electron density calculations from Stark broadening measurements of hydrogen, carbon, and aluminum transition lines, using the double array positioned parallel to the anode surface of the SMP diode, show a dense plasma located within 0.5mm of the surface which decreases by approximately an order of magnitude, going outward 1.0mm from the surface.

5. MAGNETIC FIELD MEASUREMENTS ON RITS

5.1. Introduction

One of the main objectives of this LDRD was to determine the current distribution in the SMP diode. This was accomplished through a series of experiments fielded on RITS. In the SMP diode, an electron beam is focused by its self-magnetic field onto a solid metal anode. In the process, the anode surface is heated and a plasma is generated. At the beam focus (few millimeter diameter) high current densities rapidly ionize both surface contaminant and metal substrate layers. Further away from the beam focus, the surface is ionized primarily from thermal heating, which occurs from lower beam currents and radial sheath currents, flowing parallel to the surface, which result in lower density plasmas. These plasmas develop and expand during the pulsewidth of the diode (~70ns), decreasing the effective A-K gap, which causes the impedance of the diode to continually decrease [36]. These plasmas were measured using several spectroscopic systems described in section 3. Spectra were collected using multifiber arrays, oriented radially along the anode surface, which provided a spatial profile of the plasmas at a specific time during the pulse. The spectra were composed of continua and line emission. The continua observed near the axis were due to bremsstrahlung radiation, radiative recombination, and line broadening from high plasma densities. Some of the early spectra were collected using a 0.15m spectrometer (f/4) with a 1200g/mm grating and 50 micron slit width, giving a 4Å resolution. This provided survey spectra of the carbon (C IV) and aluminum (Al III) lines, which were then chosen for the Zeeman splitting measurements. The resolution of this instrument was insufficient to observe Zeeman splitting at the fields (few Tesla) encountered in the SMP diode, so in an attempt to get the highest signals with the best resolutions, spectra were collected at mid-to-late times during the pulse, and primarily on solid targets, rather than foil-covered targets. The solid targets generally produced greater amounts of plasma, earlier in time, and since the surface was flat, rather than recessed, as in the case of the aluminum foil, the plasmas could be measured sooner in time, rather than having to allow for expansion into the field of view of the optical fibers. Using a solid target, tended to reduce the pulsewidth by 10-15nsec, but other than that, the SMP beam dynamics appeared to be the same. High resolution spectra were obtained using the Princeton Instruments SCT-320 IsoPlane spectrometer (f/4.6) with a 2400g/mm holographic grating blazed at 5000Å, and an entrance slit width of 50 microns

(see figure 5). This instrument, combined with aberration correcting optics, provided a useful means of obtaining the required resolution (0.65Å), at sufficient intensity levels.

Magnetic fields were determined from the splitting of the C IV doublet lines at 5801Å and 5812Å Angstroms. These are the 3s-3p transitions. The Zeeman effect is greater on the ½ - ½ C IV 5812Å line, which leads to a slightly broader linewidth. While the pi/sigma ratio on the ½ - ½ transition is smaller, this transition has a slightly larger energy shift in the presence of a magnetic field. All other broadening mechanisms for the lines (Stark, Doppler, and Instrumental) are the same, so any width differences are due to Zeeman magnetic field effects. Even in instances where splitting is not observed, lineshapes often have a flat-top profile, which can also only be fitted by assuming a magnetic field.

The spectra were collected by imaging chords at various radii, looking perpendicular to the beam axis. Depending on the location of the chord, some amount of both pi and sigma components of the Zeeman splitting were observed, and these contributions were often obscured by the Stark broadening of the lines. Therefore, multiple fields and angles needed to be considered. In addition, the intensities needed to be corrected for the chordal path through the plasma using an inverse-Abel transform. This was accomplished by dividing the line of sight into many points, calculating the magnetic field at each point, determining the relative intensities of the lines due to radial position, and then incorporating the angle between the line of sight and the aximuthal magnetic field. The lineshapes were fit to Voigt profiles, with Stark broadening giving the Lorentzian component and Doppler plus Instrumental broadening giving the Gaussian component. The individual lineshapes were then summed and fit to the experimental lineshape using a fitting algorithm. The magnetic field at each point is calculated using Ampere's Law [37]:

$$B = \frac{\mu_o I}{2\pi r} \qquad (5-1)$$

where I is the enclosed current, r is the distance from the axis, and μ_o is the permeability of free space. The fine structure splitting is calculated based on the weak-field approximation given in Equation 2 [41].

$$\Delta E = g\mu_B m_j B \qquad (5-2)$$

where g is the Lande factor, μ_B is the Bohr Magneton, m_j is the magnetic quantum number, and B is the magnetic field. The calculations assume cylindrical symmetry of the electron beam and an azimuthal magnetic field. For a tightly focused beam at the axis, carrying all of the current, the magnetic field should decrease as 1/r according to Ampere's law. The ratio of the pi and sigma components of the fine structure depends on the quantum numbers, m and J. The intensities of the fine structure depend on the viewing angle relative to the magnetic field. When looking parallel to the magnetic field, only the sigma components are visible, and when looking perpendicular, both sigma and pi components are observed. In between, the relative intensities of the sigma and pi components are determined from the Stokes parameters for polarized light [42]. All of the calculations assume the plasmas are optically thin, which is a good assumption, since the experimental ratio of the line transitions is two, as is the ratio of the oscillator strengths. If the plasma were optically thick, that ratio would deviate from 2.

From the inverse-Abel transforms, chordal line intensity is determined as a function of radius; however, from the previous section it was found that the electron temperature is higher closer to the beam axis, so that the C IV line intensity may decrease due to the presence of higher ionization states. The outer fibers in the array, those showing C IV line emission, are fitted with a Gaussian profile, which represents the distribution of the raw C IV line intensities with radius. This profile is then Abel-inverted, giving intensity vs. radius for the outer fibers of the array. This intensity ratio is then multiplied by the simulated spectra to account for the differences in C IV line strength across the anode. The data are assumed to be integrated over 20mm chords (the anode surface is 50mm in diameter).

Doppler broadening was investigated for its possible contributions to the overall line shape. Doppler broadening occurs due to plasma species motion towards or away from the observer in an optically thin plasma, which produces a Gaussian profile, that needs to be deconvoluted from the overall Voigt profiles. Both plasma 2D images (figure 27) and photodiode signals of plasma light emission in time (figure 28), provide information into the radial plasma motion.

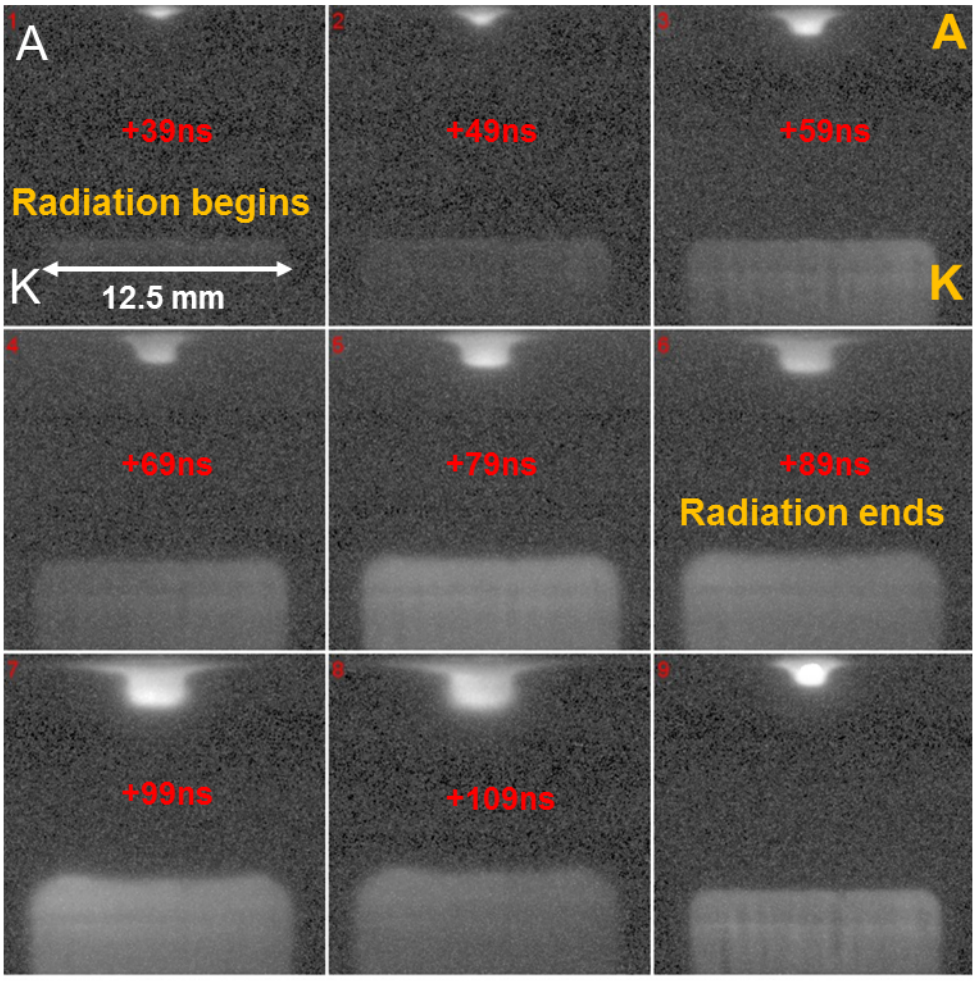

Figure 27. Plasma light emission images captured with the Photek Ultra8 Multiframe camera.

From these signals, the dense continua plasma shows a radial expansion velocity of 1.6 +/- 0.2 cm/μs, and the avalanche photodiodes (APDs), which measure much lower density plasmas, give a radial expansion velocity of ~6.5 cm/μs. The APDs cannot clearly distinguish what fraction of the signal is due to radial expansion of plasma beginning near the axis, and what fraction is due to axial expansion from the surface at larger radii, thus this value represents an upper limit on the velocity. In either case, the results shows a progression in time for the development of plasmas outward from the beam axis. From calculated lineshapes assuming a variety of velocities, it can be shown that a radial expansion velocity of > 8 cm/μs would be required to measure any Doppler shifts on the outer fibers used for the Zeeman splitting measurements [39] Since this is

greater than either of the measured radial expansion velocities, Doppler effects are not considered

.

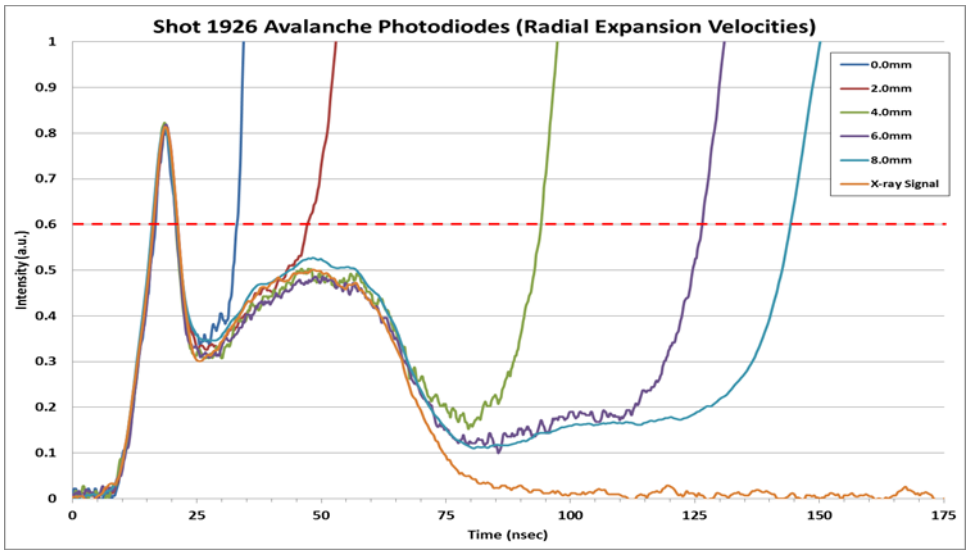

Figure 28. Avalanche photodiode signals showing radial expansion of plasma light emission.

5.2. Lineshapes:

Figure 29 shows lineouts of the C IV doublet lines at 5801Å and 5812Å taken at two radial locations. For fiber 7, the 5812Å line is wider than the 5801Å line by a factor of 1.15x. At the temperatures measured from the C III/ CIV line ratios, thermal Doppler broadening adds a small, but appreciable, Gaussian component to the lineshape. Using an average temperature of 6eV, the Doppler broadening is 0.3Å, or about one-half that of the instrumental broadening. Once the spectra are deconvoluted, using the methods described in the previous section, the current profiles are determined using Ampere's Law.

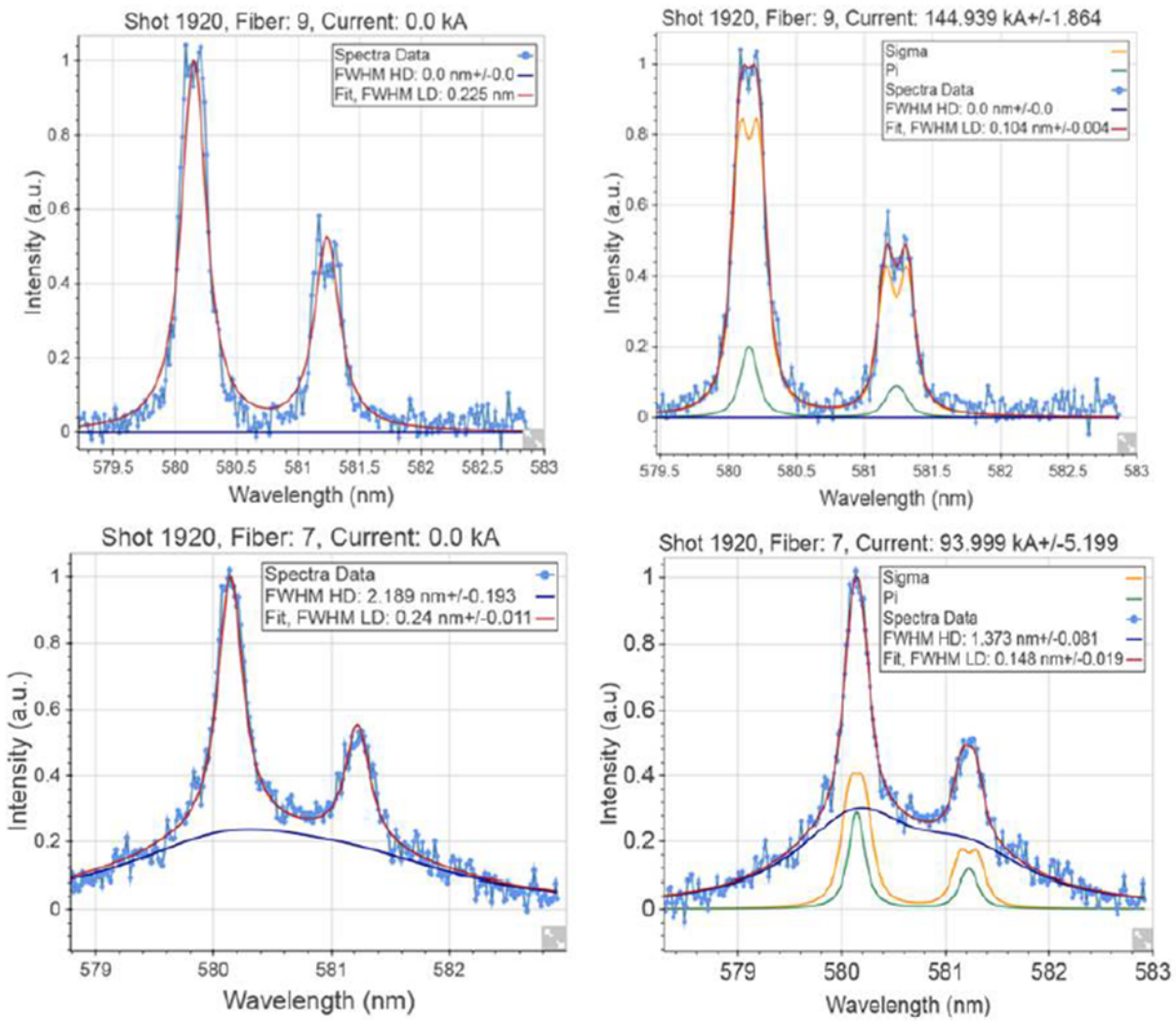

Figure 29. Spectral linefits for the C IV doublet lines, with (right) and without (left) an azimuthal magnetic field.

Figure 30 shows the enclosed current plotted as a function of radius for six shots. Because the spectral lines of sight look across multiple radii, the lineshape is influenced by the exact location of the C IV species, because of this, the plot represents the maximum enclosed current at each location. A more accurate determination could be done by selectively doping specific locations of the target, and this was attempted in a few shots using a 3mm wide stripe applied to the anode surface. The results of these shots are described in Sonal Patel's thesis [39]. The figure suggests that the enclosed current increases linearly as a function of radius out to 10mm, and perhaps beyond, which is in contrast with LSP simulations, shown in blue, that suggests all of the current is contained within just a few millimeters at the beam axis.

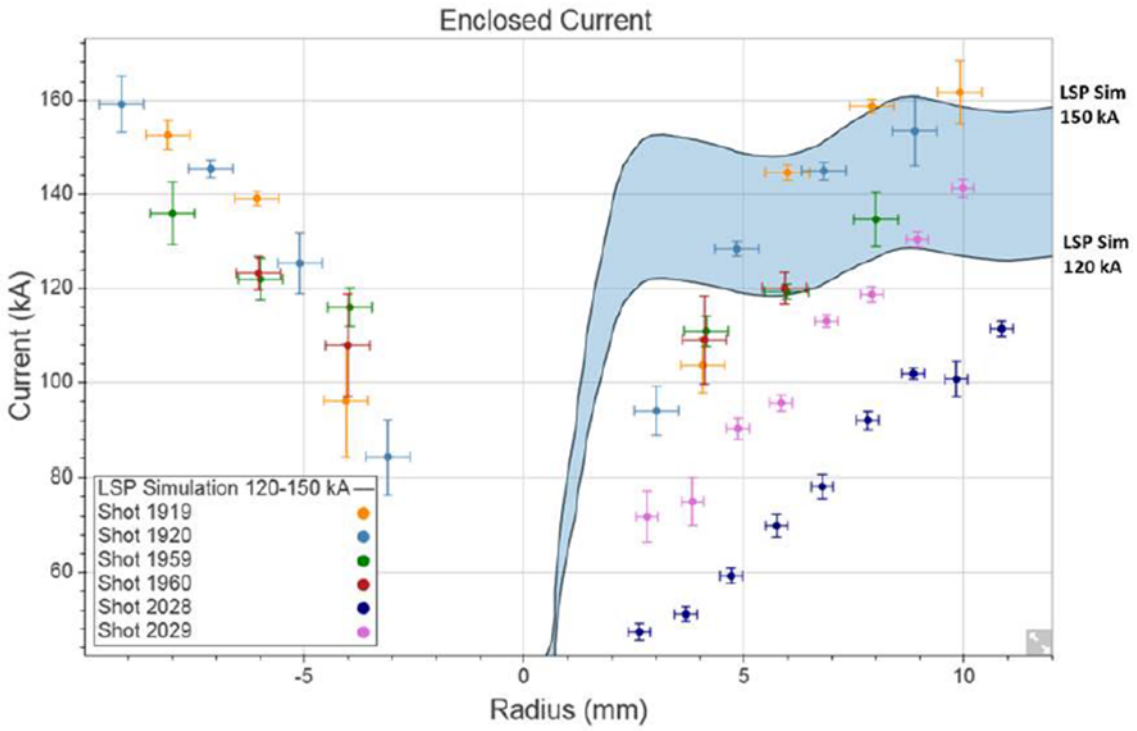

Figure 30. Plot of enclosed current versus radius as determined from C IV linesplitting, shown with LSP simulation results.

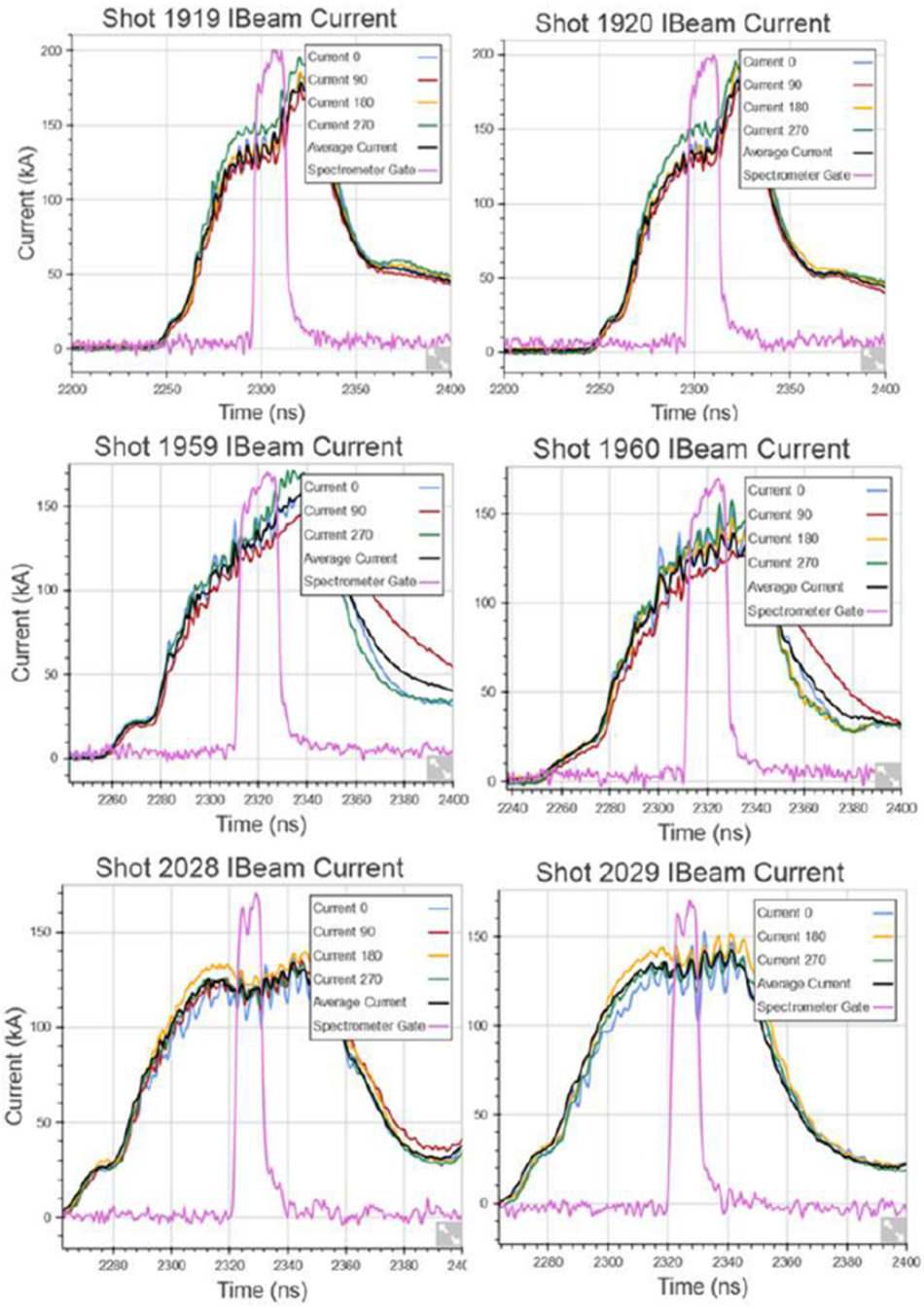

Figure 31. Current measurements obtained from four B-dot monitors located symmetrically, at a radius of 6.5 cm outward from the base of the 12.5 mm diameter cathode stalk, along with the gate times for the ICCD camera.

LSP simulations suggest that all of the diode current is located within a 2.5mm radius from the axis [40]. To test this, figure 32 shows the calculated lineshapes obtained when all of the

measured current, for shot 2028, is located within a radius of 2.5mm from the axis. The relative sigma and pi contributions for the C IV lines are determined based on the method described earlier. As can be seen, the resultant lineshapes clearly don't represent those measured experimentally. The line-splitting is much more pronounced, and only by reducing the current or increasing the radius it is contained within, can this disagreement be resolved.

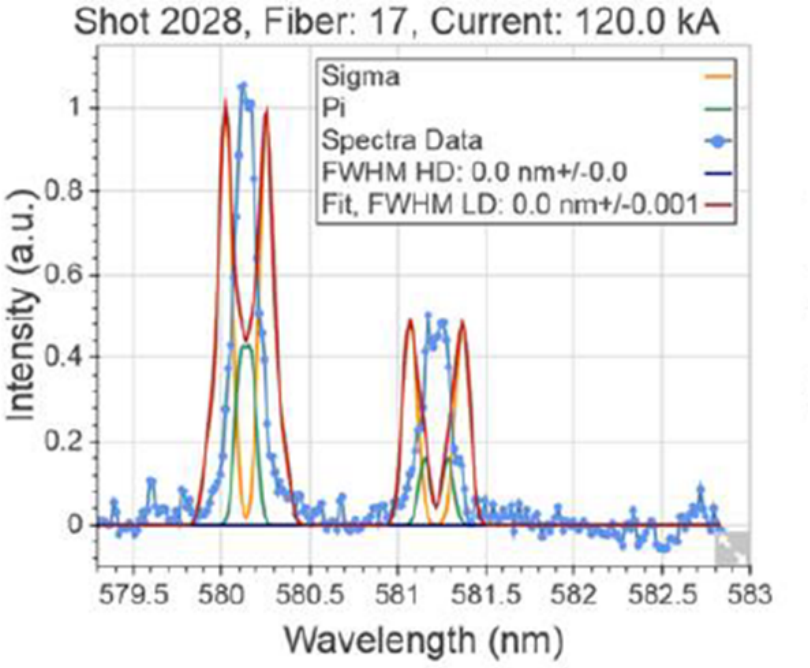

Figure 32. Lineshape calculations based on the full B-dot current (120kA) being enclosed within a 2.5 mm radius from the axis, as compared with experimental data (blue).

Even though a significant portion of the current appears to lie outside the x-ray spot size region, the current density (kA/cm^2), increases exponentially towards the axis, as expected (figure 33).

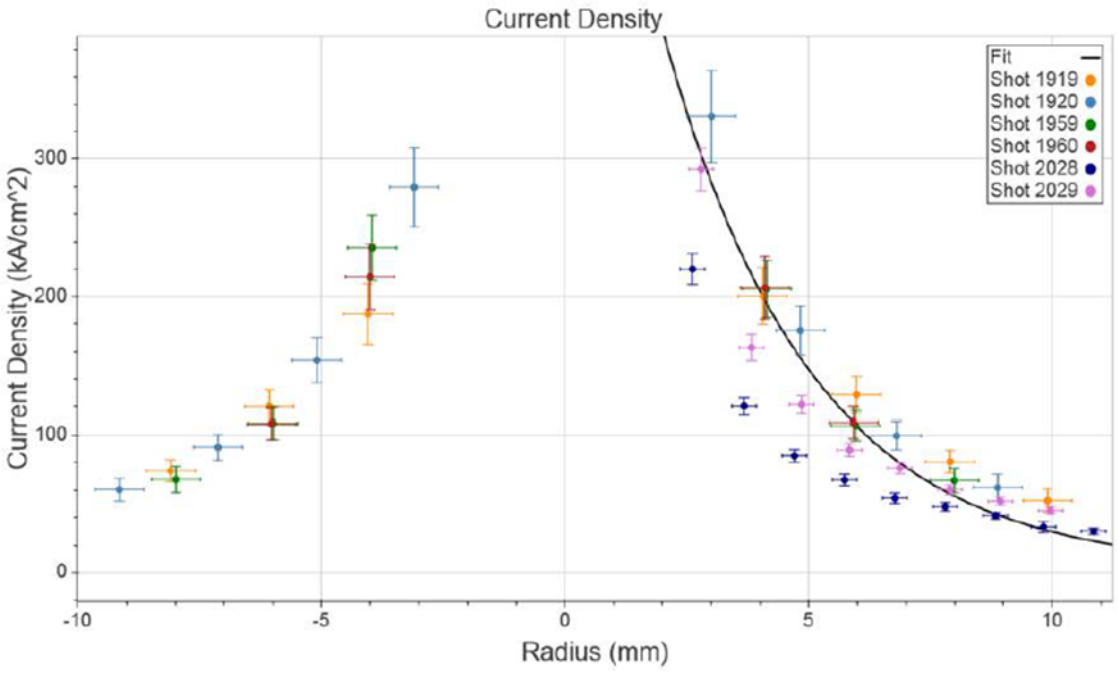

Figure 33. Current density versus radius calculated from enclosed current and fit with an exponential decay function.

There are several possible explanations for the differences between the LSP simulations and the spectroscopy measurements. One explanation proposed by Sonal Patel in her Ph.D. thesis [39] is the diamagnetic effect, in which large density and temperature gradients can partially shield the magnetic field. The density and temperature gradients across the plasma boundary observed in the framing camera images at a radius of ~2 mm are about a factor of 5x in temperature and 50x in density. If we assume just the density gradient (constant temperature), the diamagnetic effect indicates the enclosed current should be contained within a 5 mm radius, rather than 2 mm, giving the overall lower current values shown in figure 34. While not conclusive, there is certainly compelling evidence to suggest that other factors exist, which are not included in the simulations, but should be considered.

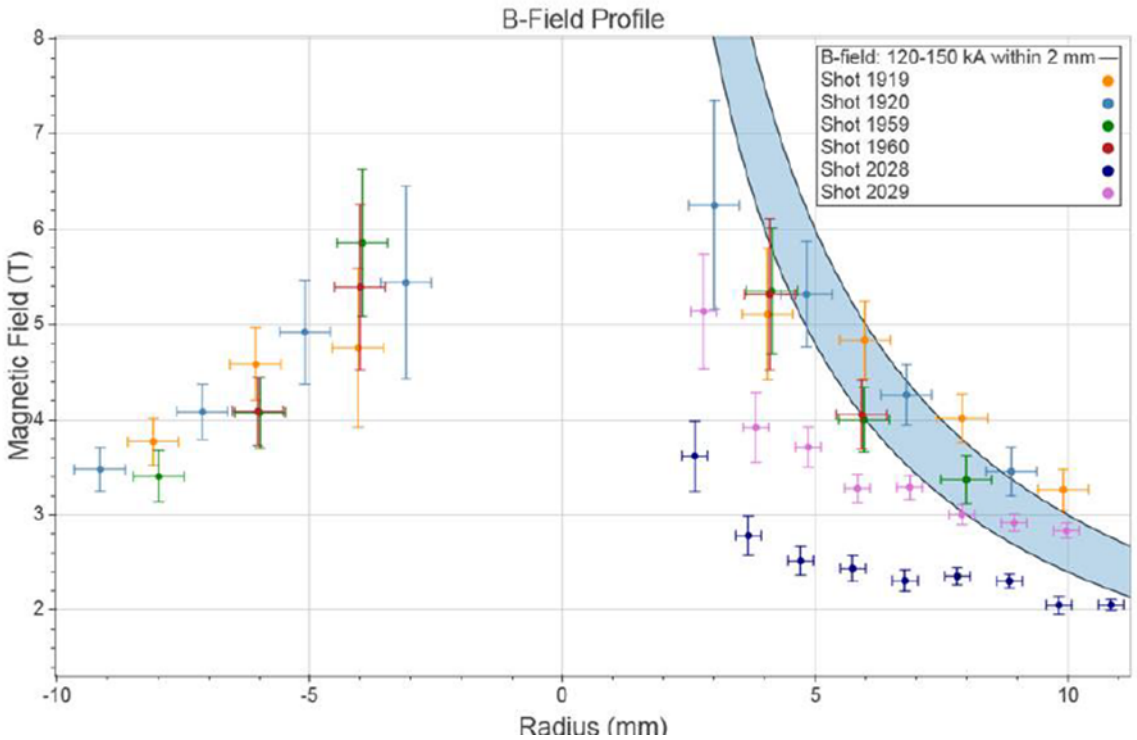

Figure 34. Experimentally determined magnetic fields versus radius, plotted together with a blue band obtained by assuming all current is enclosed within 2 mm of the axis.

Several different dopants were tested on RITS in an attempt to measure specific transitions that were particularly susceptible to Zeeman splitting. While some success was achieved, many of the lines were either undetectable or too weak to obtain useful lineouts. Additionally, some coatings had a negative effect on the radiation pulsewidth of the diode, causing it to end prematurely. Since most of the spectral data was collected from mid to late in the pulse, shortening the pulsewidth often meant the spectra was collected during a time when the voltage in the diode was collapsing and the e-beam expanding. However, there were some interesting observations made regarding the effects of different coatings on the SMP diode pulsewidth, in particular differences between salt coatings, transition metals, and metal/semi-metals. These observations are discussed in Sonal Patel's thesis [39].

6. MAGNETIC FIELD SHIELDING MEASUREMENTS ON RITS

6.1. Introduction

As part of this LDRD, our colleagues at the Weizmann Institute studied the Zeeman effect on spectral emission lines in order to determine the radial distribution of the azimuthal magnetic field in the Self-Magnetic Pinch (SMP) diode on RITS, as a function of distance from the anode surface. Spectroscopic measurements based on Zeeman splitting have been used in the past to determine magnetic fields and their penetration into the anode plasma in the applied-magnetic-field ion diode [2]. For the SMP diode, Zeeman splitting cannot always be resolved due to large Stark broadening in the higher-density plasma at the anode surface. In this case, line-shape analysis [41-43] yields an upper limit of the magnetic field. Using this method, calculation of the line shapes, considering Stark and Doppler broadenings, instrumental response, and Zeeman effect contributions were made, which yielded information on the magnetic field and plasma density. For this analysis, the data provided the radial distribution of the azimuthal magnetic field near the anode during focusing of the electron-beam. Furthermore, measurements made across the ~1-mm-wide anode surface plasma, gave shielding of the magnetic field in the plasma as a function of the axial distance (< 1 mm) from the anode surface. These data allowed comparisons to be made with solutions of the magnetic-field diffusion equation. The plasma resistivity inferred from these measurements could then be compared to the Spitzer resistivity. The latter was estimated from the electron temperature (T_e), which was obtained from line-intensity ratios and the average ionic charge-state. The shielding of the B-field was found to be in agreement with the estimation of the Spitzer-resistivity. We note that the line shape modeling also yielded the electron density (N_e) in the plasma. This work represents the first measurements of the magnetic field in an electron beam diode, and the first experimental determination of the magnetic-field shielding in a particle-beam diode.

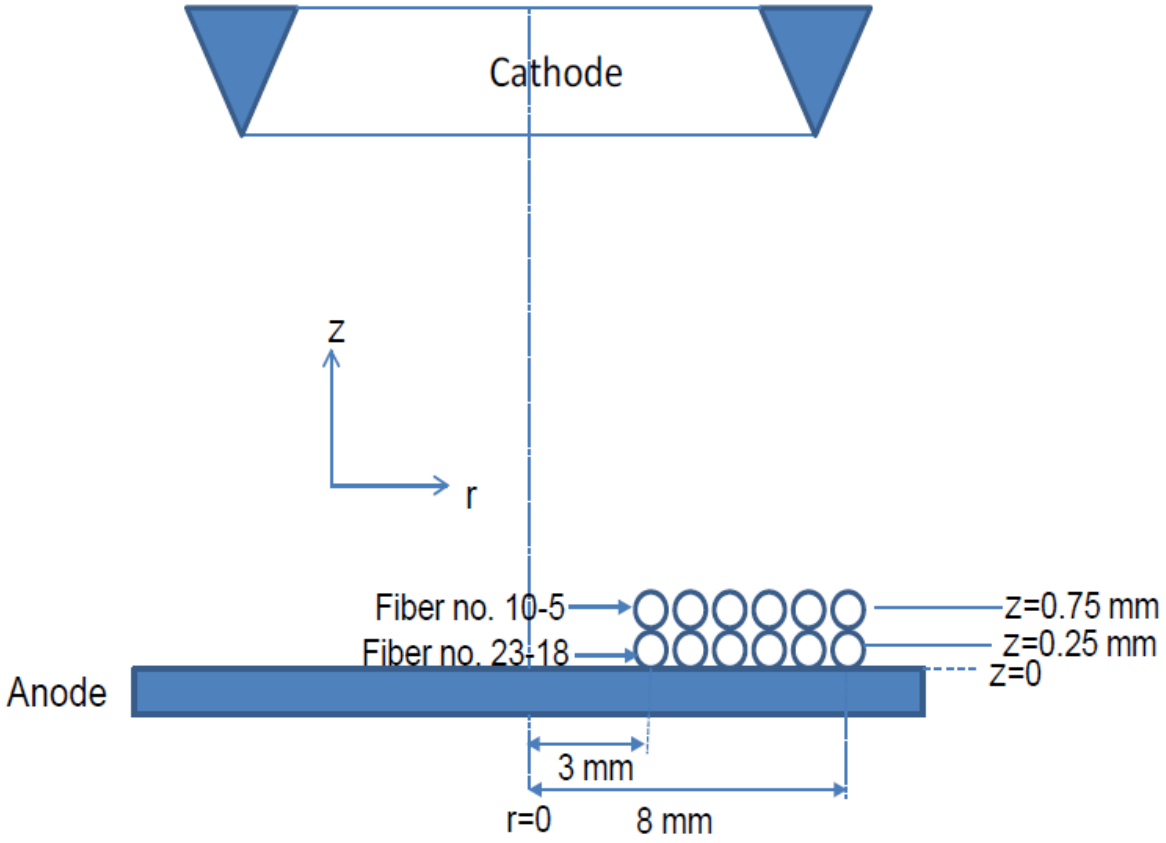

Figure 35. Schematic of the SMP geometry and fiber orientations.

6.2. Experimental Results

Light emission from the anode plasma of the SMP diode was recorded and used to obtain information on the plasma properties and spatial distributions of the azimuthal magnetic field (B_θ) of the diode. A schematic of the measurement is shown in figure 35. Two sets of fiber arrays were used to collect light from different radial and axial positions. As shown in figure 35, one set of fibers collected light from a 0.5 mm wide region near the anode surface ($0 \leq z \leq 0.5$ mm) and the second from a $0.5 \leq z \leq 1.0$ mm region, where $z = 0$ is the anode surface. The output of the fibers was imaged onto the input slit of the spectrometer, and the spectrometer's output was recorded on an ICCD camera using a 10 ns gate to obtain spatially and temporally resolved spectra.

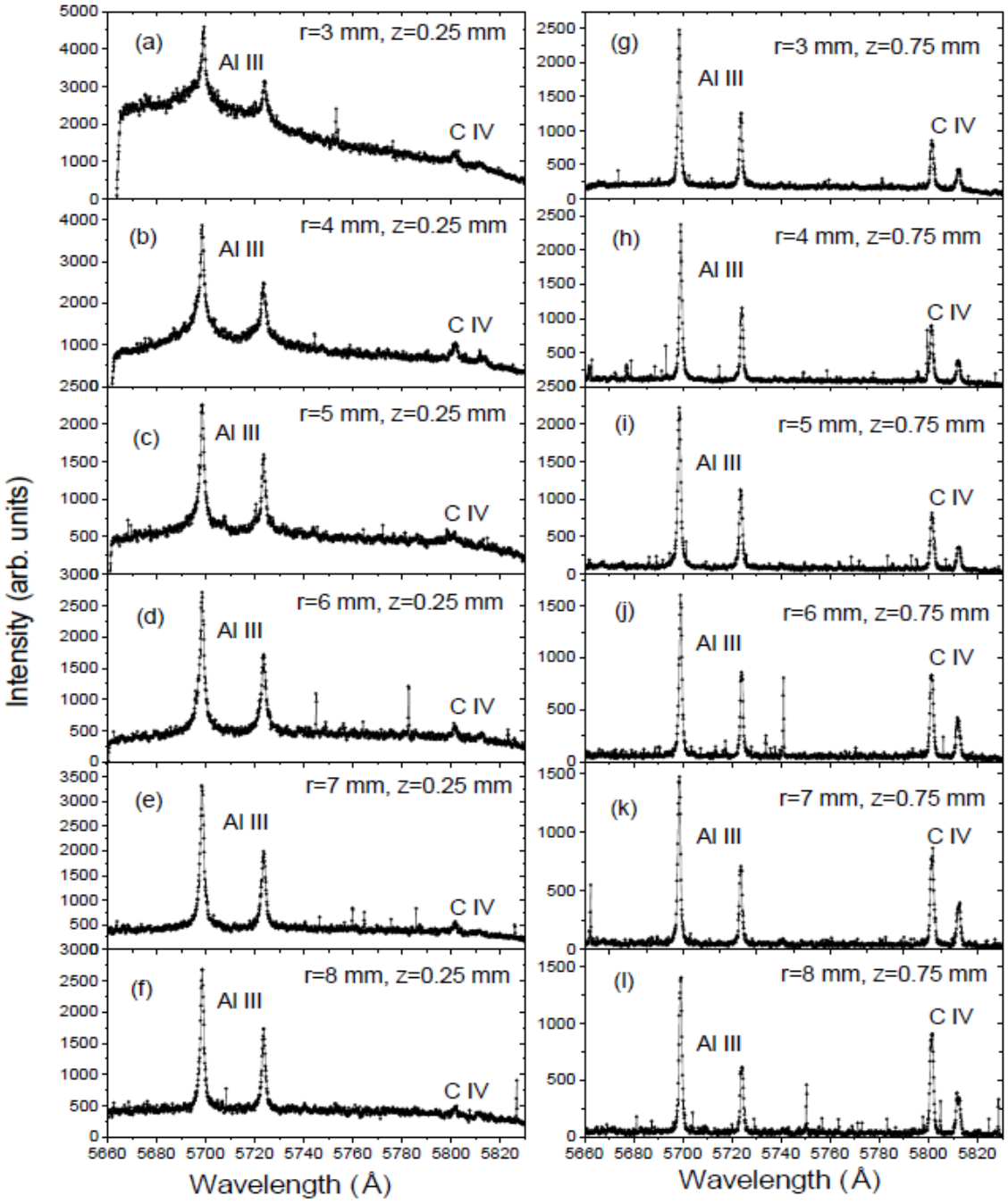

Figure 36. Spectra recorded at different radial positions using the double fiber array. The spectra on the left (a)-(f), are from the region adjacent to the anode surface, and the spectra on the right (g)-(l) are from the region 0.75 mm off the anode surface.

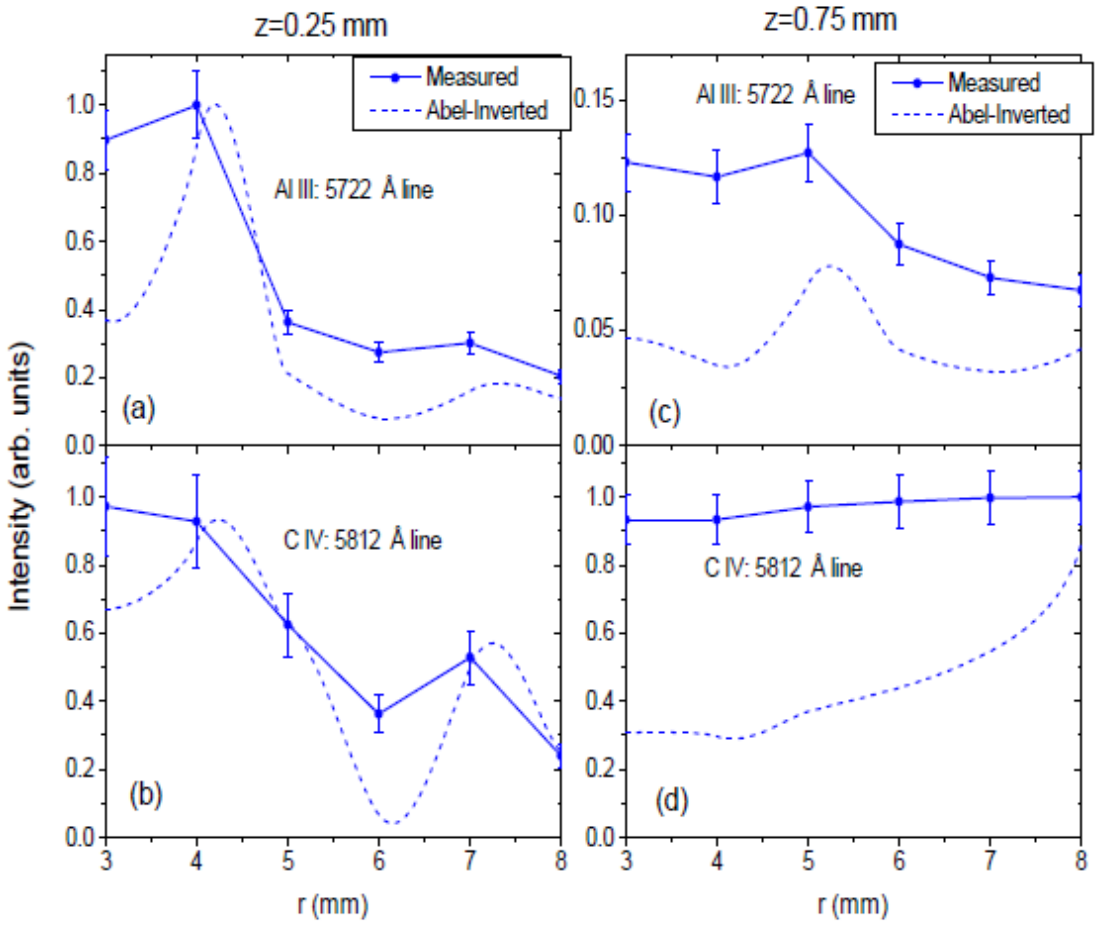

Figure 37. Radial distribution of the relative line intensities of Al III 5722Å and C IV 5812Å. The left and right plots represent emission from z = 0.25 mm and z = 0.75 mm distances, respectively. The solid lines and the dashed lines represent the measured chordally-integrated and Abel-inverted intensities.

Figure 36 shows the spectra recorded at different radial and axial (z) positions. The left side shows the spectra from the region at $0 \leq z \leq 0.5$ mm, and the right side shows the spectra recorded from the further region, at $0.5 \leq z \leq 1$ mm. The spectra farther from the anode surface (Fig. 36 (g)-(l)) clearly show the Al III doublet transition 4s-4p (5996Å and 5722Å) and the C IV doublet transition 3s-3p (5801Å and 5812Å), whereas in the spectra from near the anode surface, only the Al III 4s-4p doublet is clearly observed, and the C IV 3s-3p doublet is very weak. The radial distribution of the relative intensities of the Al III 5722Å and C IV 5812Å emissions are shown in figure 37. Both the line-integrated data and the inverse-Abel transforms are given. For the inverse-Abel transform, we assume the intensity falls linearly to 0 at r = 10 mm. The

intensities of each transition are normalized to their maximum values. The figure illustrates that near the anode surface, at $0 \leq z \leq 0.5$ mm, the intensities of both Al III and C IV lines peak at r = 4 mm. While at $0.5 \leq z \leq 1.0$ mm, the intensity of the Al III line is nearly constant throughout r, and the intensity of the C IV line is maximum at the edge (r = 8 mm) and falls towards the center. It can also be seen that near the edge of the plasma, in the radial direction, the Al III is mainly emitted from a region close to the anode surface (small z-values), whereas the C IV is from larger z. This is probably due to the fact that the carbon is absorbed on the aluminum anode surface, and when the electron beam hits the anode surface, the carbon comes out first and ionizes, forming C IV. In addition, C IV tends to expand faster due to its higher charge-to-mass ratio.

6.3. Data Analysis

Spectral line-shapes are used to determine the magnetic field and electron density. Since the experimental spectra are line-integrated chords across the anode surface, in order to obtain the line-shape as a function of r, an inverse-Abel transform has to be performed. We employ an "onion-peeling" approach, assuming the plasma boundary is at r = 8 mm. In this approach, the line-shape at each radius is obtained by subtracting from each line-integrated spectrum the signal emitted from radii that are larger than the distance of the chord to the axis. The subtracted contribution from each successively larger radius is the simulated spectrum (emitted for that radius) weighted according to its relative volume (relative to the total volume observed for the corresponding chord), taking into account the angle between B_θ and the direction of the observation. For example, the line shape at r = 7 mm is obtained by subtracting from the spectrum integrated along the chord corresponding to r = 7 mm (figures 36e and 36k), and the spectrum simulated for r = 8 mm, multiplied by a factor of 0.57 (obtained by geometric considerations), and modified according to the change in the angle between B_θ at r = 8 mm to the observer, accounting for the line-of-sight changes from a chord at r = 8 mm to a chord at r = 7 mm. To determine B_θ, first the Zeeman profile for all the different fields is calculated. Subsequently, each Zeeman profile is convolved with a Lorentzian (Stark broadening) and a Gaussian (instrumental FWHM of 0.5Å). Doppler broadening, considering $T_i = T_e \cong 5$ eV (T_e is measured from the C III and C IV line-intensity ratios), is negligible. The simulated spectrum is compared with the Abel-inverted spectrum, and the value of B_θ and the Stark width are then

varied to obtain the best fit (minimum of χ^2) to the spectrum, using the same procedure as in [41,43].

In the analysis, we only fit the (1/2 – 1/2) component of the doublet, owing to its higher sensitivity to the magnetic field. The experimental intensity ratio (1/2 - 3/2) / (1/2 - 1/2), expected to be 2, is found to be between 2.0-2.2. The deviation from a value of 2 can be either due to errors in the measurement or impurities contributing to the (1/2 – 3/2) component. For the case of Al III, a C III impurity at 5696Å can affect the (1/2 – 3/2) component line-shape. Under these conditions, simulating the (1/2 – 3/2) does not help to constrain B_θ. Figure 38 shows the experimental data for the Al III 4s-4p component at different radii for $0.5 \leq z \leq 1.0$ mm (after inverse-Abel transform), together with their best fits. Figure 39 gives the same for the C IV 3s-3p component. The inverse-Abel procedure introduces additional uncertainties into the experimental data, and reduces the signal-to-noise ratios (SNR) for $r < 8$ mm. The latter effect is particularly strong for C IV due to the decreased intensity with decreasing r (see Fig. 37d). Therefore, for C IV, the fitting is done on the experimental data obtained by averaging the data for r = 4 and 5 mm, and for r = 6 and 7 mm. The SNR in r = 3 mm is too poor and is not useful. The parameters that yielded the best least-square fits are given in figures 38 and 39. The electron density (N_e), that corresponds to each Stark-Lorentzian width [44,45], is also given in that figure. The values of N_e are between $\underline{1\text{-}2 \times 10^{17}\ cm^{-3}}$. Close to the anode surface ($0 \leq z \leq 0.5$ mm) and for $r < 8$ mm, the line shapes are Stark dominated (due to the higher density), prohibiting the B-field determination with a reasonable error bar. At the outer region (r = 8 mm), N_e is relatively lower and an upper limit of the magnetic field can be determined from the analysis of the detailed shape of the Al III 5722Å line. A blow up of Al III 5722Å line at z = 0.25 mm and r = 8 mm along with different fits, obtained by varying the

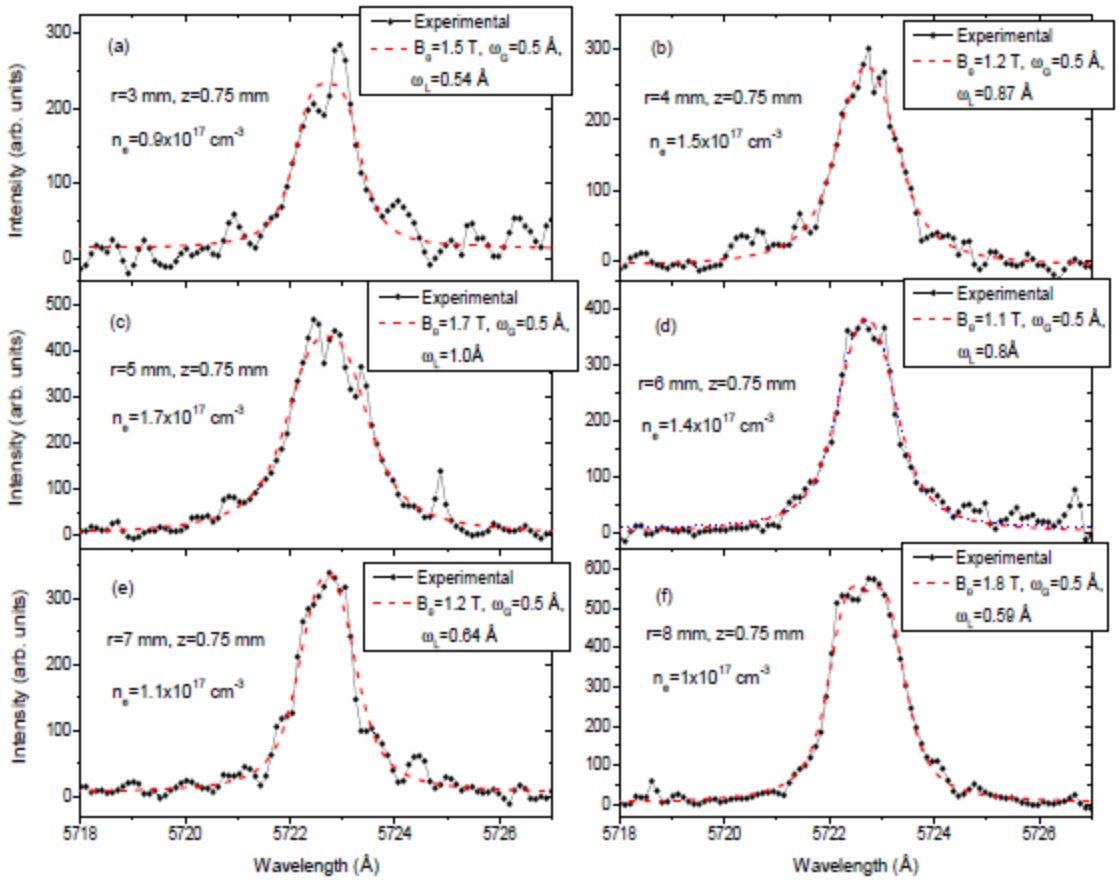

Figure 38. Al III 4s-4p component from the region $0.5 \leq z \leq 1.0$ mm at different radii after Inverse-Abel transform. Dashed (red) curves are the simulated spectra obtained by convolving the Zeeman pattern with the Stark-Lorentzian, and Instrumental-Gaussian profiles. In the figure, B_θ, ω_L, and ω_G are, respectively, the azimuthal magnetic field value, Stark FWHM, and instrumental FWHM used for the fit; and n_e is the electron density corresponding to ω_L.

Lorentizian component and assuming B_θ = 0.8, 1.2, and 1.5 T, are shown in figure 40. As demonstrated in the figure, the fits do not change much up to B_θ = 1.2 T, and assuming B_θ = 1.5 T, a reasonable fit cannot be obtained for any Lorentzian. Therefore, at this point, only an upper limit of the field ($B_\theta \leq 1.2$ T) can be determined. Figure 41 shows the values of B_θ obtained for various radial positions. It is seen that the B_θ values obtained from the C IV line are higher than those obtained from the Al III lines, even though the spectrum of the two ions is collected by the

same fiber focused at z = 0.75 mm. It was shown in an earlier section that the intensity ratio of the C IV to Al III lines increases with the distance from the anode. Thus, the Zeeman effect of the C IV line tends to reflect the B-field farther from the anode than the Al III line. For simplicity, we assume that the Al III line gives the B_θ value over the half of the fiber's field of view in the z-direction that is closer to the anode surface, namely z = 0.625±0.125 mm, whereas the C IV line gives B_θ at z = 0.875±0.125 mm.

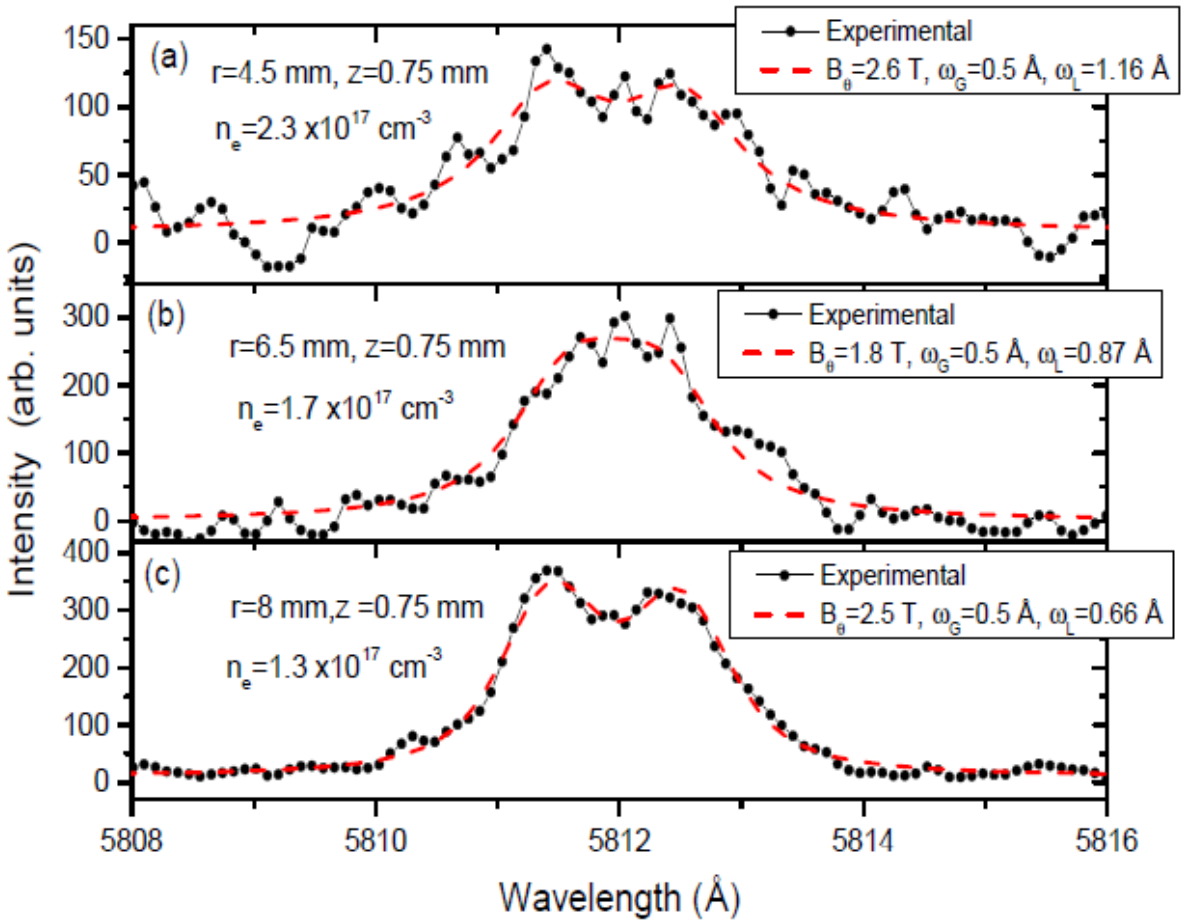

Figure 39. C IV 3s-3p, $^3S_{½}$ - $^3P_{½}$ component, from the region 0.5 ≤ z ≤ 1.0 mm at different radii after Inverse-Abel transform. Dashed (red) curves are the simulated spectra obtained by convolving the Zeeman profile with the Stark-Lorentzian and Instrumental-Gaussian profiles. In the figure, B_θ, ω_L, and ω_G are, respectively, the azimuthal magnetic field value, Stark FWHM, and instrumental FWHM, used for the fit; and n_e is the electron density estimated from ω_L.

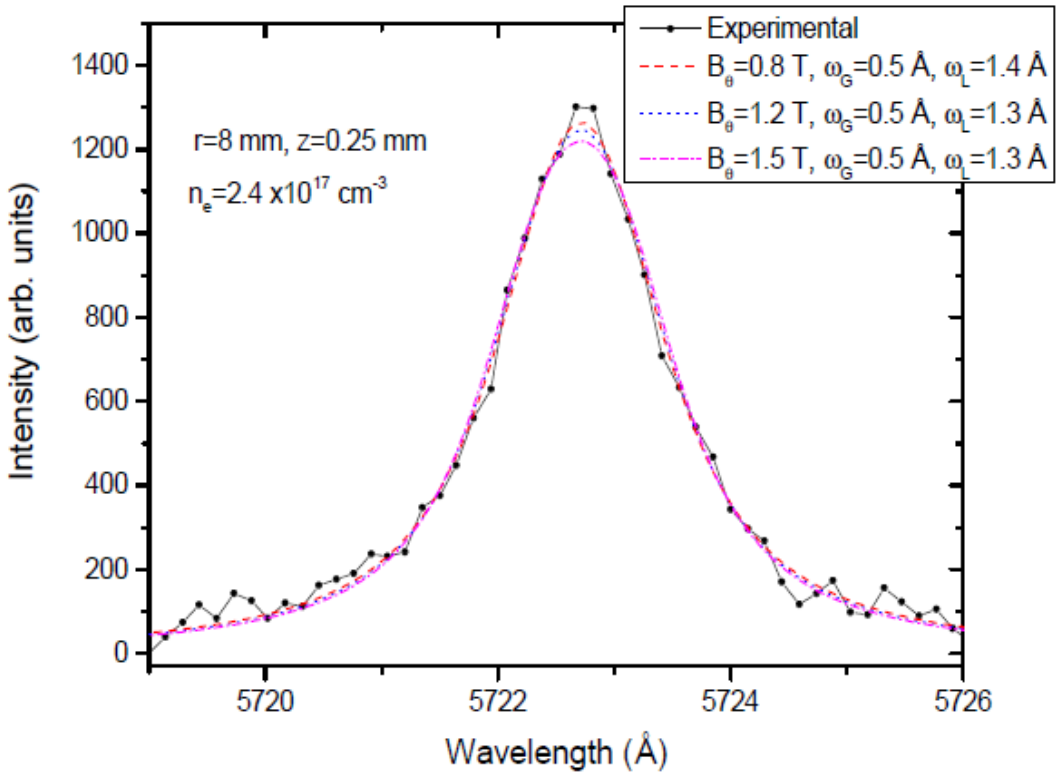

Figure 40. Al III 4s-4p, $^3S_{½}$ - $^3P_{½}$, 5722Å line, along with different fits, recorded from the region of $0 \leq z \leq 0.5$ mm at r = 8 mm.

We now discuss the errors in the measurements. The errors indicated in the figure represents the uncertainties in determining the Zeeman splitting (for r = 8 mm and z = 0.75 mm) or in the fit of the line shapes. B_θ corresponding to the best fit (minimum of χ^2) of the line-shape is represented by the symbols in the figure. The lower and upper values of B_θ correspond to an increase of 20% in χ^2. For r < 8 mm, we find that a reasonable fit can be obtained even when $B_\theta = 0$ is assumed. This can be understood by the fact that when no Zeeman-split pattern is observed, the broadening of the spectral line due to the Zeeman effect can be reasonably reproduced by Stark broadening. However, the absence of an observed splitting provides a clear upper limit on the assumed B_θ.

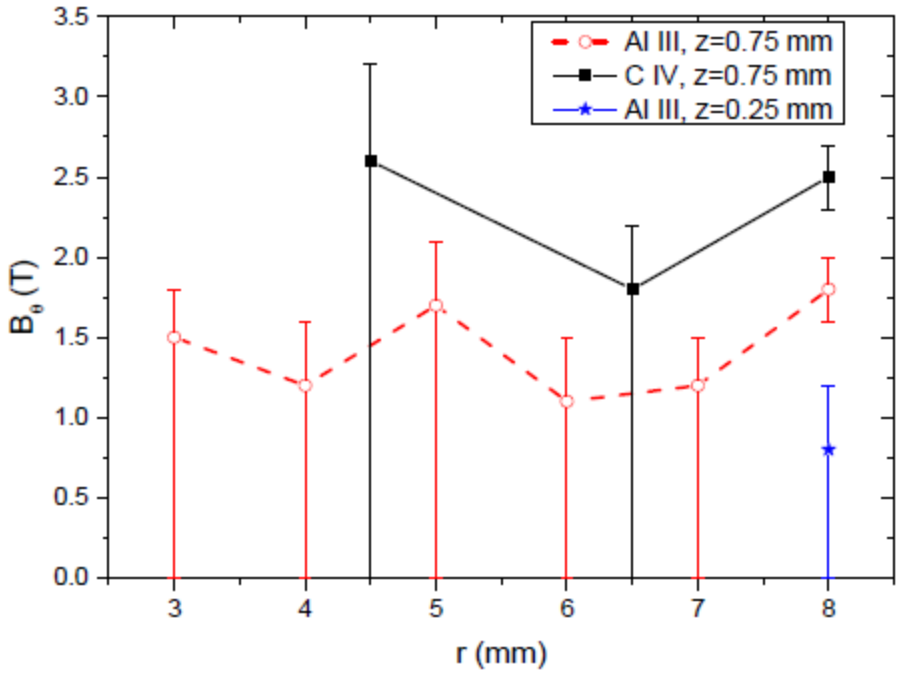

Figure 41. Radial distribution of B_θ obtained from the fit of the lineshapes of C IV 3s-3p and Al III 4s-4p transitions.

6.4. Magnetic Field Shielding

The lower value of B_θ towards the anode surface, seen in figure 41, demonstrates the shielding of the magnetic field by internal currents in the anode plasma. The low B_θ values obtained from the Al III line recorded from the region z = 0.25±0.25 mm, i.e. fibers viewing the region closest to the anode surface, are consistent with the expected stronger shielding effect deeper in the anode plasma. We now attempt to explain the shielding effect of B in the anode plasma by considering the measurements for r = 8 mm, since at this radial position B_θ is determined with the highest accuracy. Here, at z = 0.875 mm, the observed B is 2.5 T, giving a current of 100 kA within this radius (out of the total 120 kA measured at this time). The true total current within r = 8 mm can be 100 kA, if no shielding effect occurs for the data point at r = 8 mm and z = 0.875 mm, or it can be between 100 to 120 kA, if shielding occurs to some extent. In either case, if the total current within r = 8 mm is < 120 kA, it means that part of the current in the diode flows to the anode surface outside the r = 8 mm region (note that the cathode

radius is ~6 mm). For simplicity, we assume that the total current flows within r = 8 mm, namely the unshielded-B value at this radius, and at the plasma edge, in the z-direction, is 3 T. Also, for simplicity, we assume that the anode-plasma thickness in the z-direction at r = 8 mm is ~ 1 mm and is constant in time. Thus, the B_θ field at r = 8 mm and z = 1 mm rises in time to a value of 3 T (corresponding the value of 120 kA at the time of measurement), where the rise in time can be obtained from the measured current waveform. With these assumptions we can consider the diffusion equation [46]:

$$\frac{\partial B}{\partial t} = -\frac{c^2}{4\pi}\nabla \times (\eta \nabla \times B) \qquad (6-1)$$

where η is the plasma resistivity and c is the speed of light in free space. Here we have neglected the convective and Hall terms, which is justified for our plasma conditions. Equation 6-1 can be rewritten as:

$$\frac{\partial B}{\partial t} = -\frac{c^2}{4\pi}\left[-\eta \nabla^2 B + \nabla \eta \times (\nabla \times B)\right] \qquad (6-2)$$

For a uniform plasma resistivity (η), the second term on the right hand side of equation 6-2 vanishes and the equation for $\mathbf{B} = B_\theta \boldsymbol{\theta}$ becomes:

$$\frac{\partial B_\theta}{\partial t} = \frac{c^2 n}{4\pi}\left[\frac{1}{r}\frac{\partial}{\partial r}\left(r\frac{\partial B_\theta}{\partial r}\right) + \frac{\partial^2 B_\theta}{\partial \xi^2} - \frac{B_\theta}{r^2}\right] \qquad (6-3)$$

here, $\xi = z - z_o$, is the distance from the plasma boundary at $z = z_o$. Assuming a realistic current density J(r) near r = 8 mm, it can be shown that equation 6-3 can be approximated to within very few percent by:

$$\frac{\partial B_\theta}{\partial t} = \frac{c^2 \eta \partial^2 B_\theta}{4\pi\ \partial \xi^2} \qquad (6-4)$$

which is the one-dimensional diffusion equation. The boundary conditions for B_θ for

these experimental conditions are:

$$B_\theta(\xi\,, 0) = 0, \qquad (6-5)$$
$$B_\theta(\xi = 0\,, t) = B_\theta(t)$$

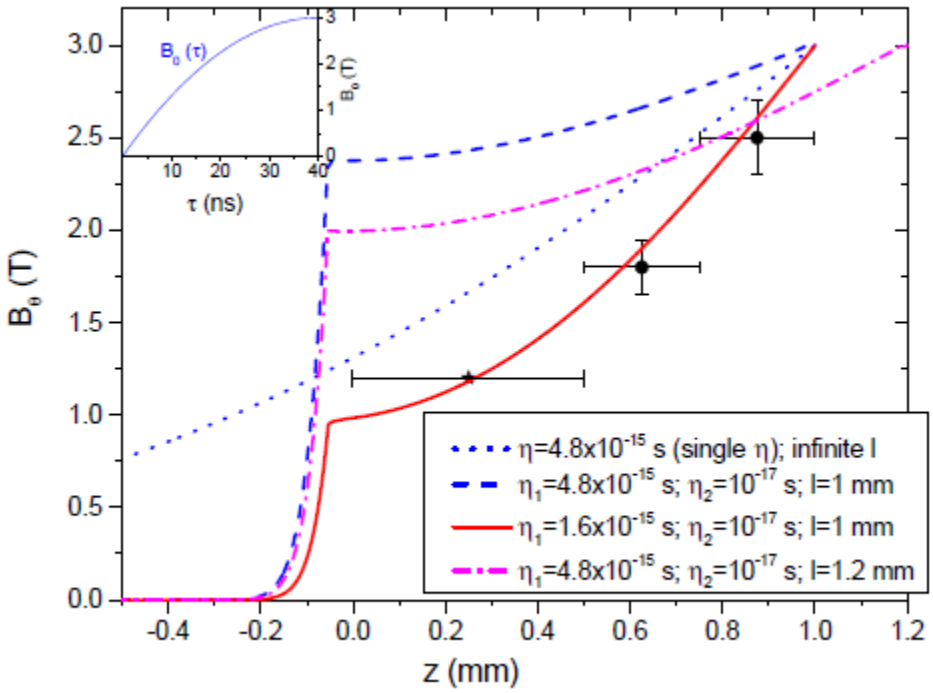

Figure 42. Solution for the magnetic field diffusion in the plasma. Dotted (blue)-line represents the solution for infinite plasma thickness with resistivity η = 4.8 x 10-15 s (corresponds to Spitzer resistivity at T_e = 5 eV). Dashed (blue) and solid (red) lines represent the solution considering the plasma and the metallic anode (z = 0 is the interface of the anode surface and the plasma). η_1 and η_2 are, respectively, the resistivities of plasma and of the Al-foil-anode. l is the plasma thickness assumed to be 1.0 or 1.2 mm, where B_θ at the plasma edge is always assumed to be 3 T at time of measurement. Symbols with the error-bars are the measured values and the "*" denotes the estimated upper limit of B_θ. Solutions are obtained by taking the parabolic waveform of B_o, shown in the upper left corner of the figure.

A simple solution of equation 6-4 can be made for an infinite plasma thickness (i.e., plasma thickness, l >> skin depth, δ). However, in the present case l ~ δ Therefore, B_θ is not zero at the conductive anode surface, which affects the B_θ distribution in the plasma. Since the resistivity of the anode is much less than that of the plasma, η = η(z) is taken as a step function, where η_1 and η_2 are, the resistivities of the plasma, and of the conductive anode, respectively. η_1 is estimated from the electron temperature in the plasma, determined to be 5-6 eV from line intensity ratios

that were measured in the experiment. This analysis also yields an average Z in the plasma of 2.5±0.5, which, together with n_e obtained in this work ($n_e \cong 2 \times 10^{17}$ cm^{-3}), yields a Spitzer resistivity of $(4.8 \pm 1.4) \times 10^{-15}$ s [47]. For the conductive anode, we use $\eta_2 = 1 \times 10^{-17}$ s. Substituting $\eta = \eta(z)$ into equation 6-2, it becomes,

$$\frac{\partial B_\theta}{\partial t} = \frac{c^2}{4\pi}\left[\eta \frac{\partial^2 B_\theta}{\partial \xi^2} + \frac{\partial \eta \partial B_\theta}{\partial \xi \, \partial \xi}\right] \qquad (6-6)$$

Equation 6-6 is solved numerically with the boundary conditions described in equation 6-5. Here, $B_0(\tau)$ is taken to be parabolic in time, approximately reflecting the true current waveform, and is assumed to rise to 3 T, as discussed above. Figure 42 shows the solution for a plasma of thickness $l = 1.0$ mm (constant in time), using η_1 and η_2 as stated above. Also shown is the solution for a plasma resistivity that is 3x lower than the Spitzer value (for comparison, the solution for an infinite plasma thickness, assuming the plasma resistivity $\eta = 4.8 \times 10^{-15}$ s is also shown). The sensitivity of the solution to l is also shown in the figure by assuming $l = 1.2$ mm, which is also consistent with the data. Within the uncertainties, a plasma resistivity that is close to Spitzer is found to be consistent with the magnetic field diffusion observed.

The distribution of the maximum (unshielded) B-field value cannot be determined for each radius from these data since shielding may occur to some extent at each position viewed in the anode plasma. However, the expected value for r = 3 mm can be evaluated from the x-ray dose emitted from the beam focus region (r < 3 mm), giving at least 60 kA of current. This means that the unshielded-B value at r = 3 mm is 4 T, nearly 2x larger than the measured value at z = 0.5-1 mm. This demonstrates that the shielding of B at r = 3 mm is much stronger than that for r = 8 mm, which is expected due to the larger plasma thickness at r = 3 mm, as seen from the visible imaging data (figure 27).

6.5. Conclusions

Simultaneous measurement of the B_θ and n_e near the anode surface of a relativistic SMP diode is determined from detailed line shape calculations of the Al III 4s-4p and C IV 3s-3p doublet emissions. The measurement of B_θ as a function of r, for different distances from the anode

surface, yielded information on the shielding of the B-field by the anode plasma, and on the plasma resistivity. However, the unknown extent of the field shielding at each radius does not allow a unique determination of the radial distribution of the current-density; therefore, more measurements are needed.

7. ELECTRIC FIELD MEASUREMENTS ON RITS

7.1. Introduction

Spectroscopic measurements were made on the Self-Magnetic Pinch (SMP) diode on RITS to investigate Stark shifting of spectral lines as a means of determining local electric field profiles. In high electric fields (MV/cm), excited state electron orbits are perturbed, resulting in a shift (second-order Stark effect) of the spectral lines. The amount of this shift is dependent on the magnitude of the field strength and its orientation relative to the observer. These types of measurements were conducted at Sandia in the 1990's on PBFA-II in support of the ion fusion program [48,49]. The PBFA-II experiments (20TW, 2cm gap) measured lithium neutrals from charge exchange of Li I in the gap of a 10 MeV lithium ion beam diode. These experiments measured electric fields in the gap of up to 10 MV/cm which at the time were an order of magnitude larger than any previous measurements, and remain to this day the highest E-field measurements in a pulsed-power diode. The results from these experiments were instrumental in helping to understand the physics of ion beam diodes and were used to benchmark the 3D PIC simulation code, QUICKSILVER. Prior to this, electric field measurements were made on a 0.1TW, 1 MeV ion diode at Cornell [50,51], where fields up to 1.5 MV/cm were measured across 0.5-1cm gaps from Al ++ ions (ex. 4529Å) emission spectra. The RITS experiments used the same Li I (6708Å) line transition that was used by Jim Bailey on PBFA II.

7.2. Experimental Configuration

Figure 43 shows the fiber orientation relative to the anode and cathode gap that was used for these measurements. The fibers collected light from a 0.5 mm diameter region just off the anode surface, at different radial locations. For this analyses, we will concentrate on the fibers located at r = 4.5 mm and r = 9.5 mm from the beam axis. The full fiber array spanned 13mm from the axis outward and contained 11 individual fibers.

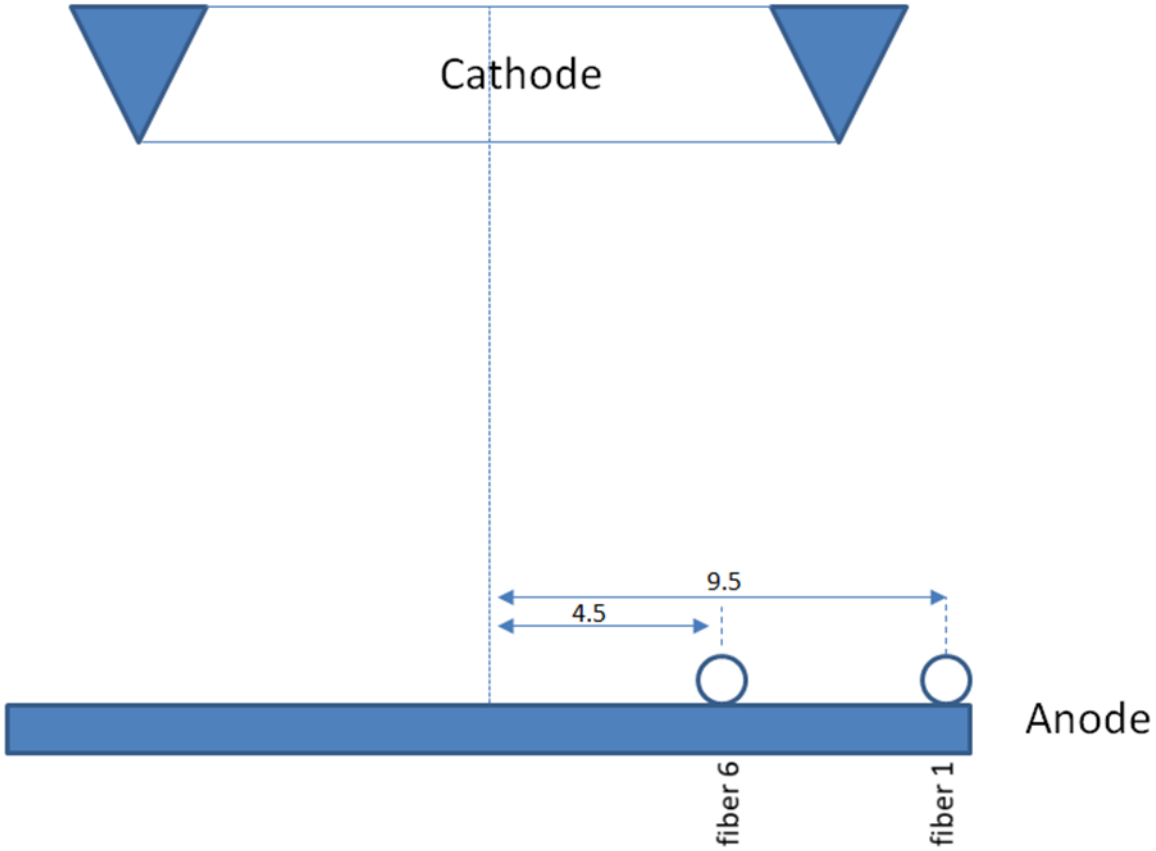

Figure 43. Schematic of the SMP geometry and fiber orientations for the single array.

Due to the large continua emission observed close to the axis, only the outer fibers can be used for this measurement, see figure 44.

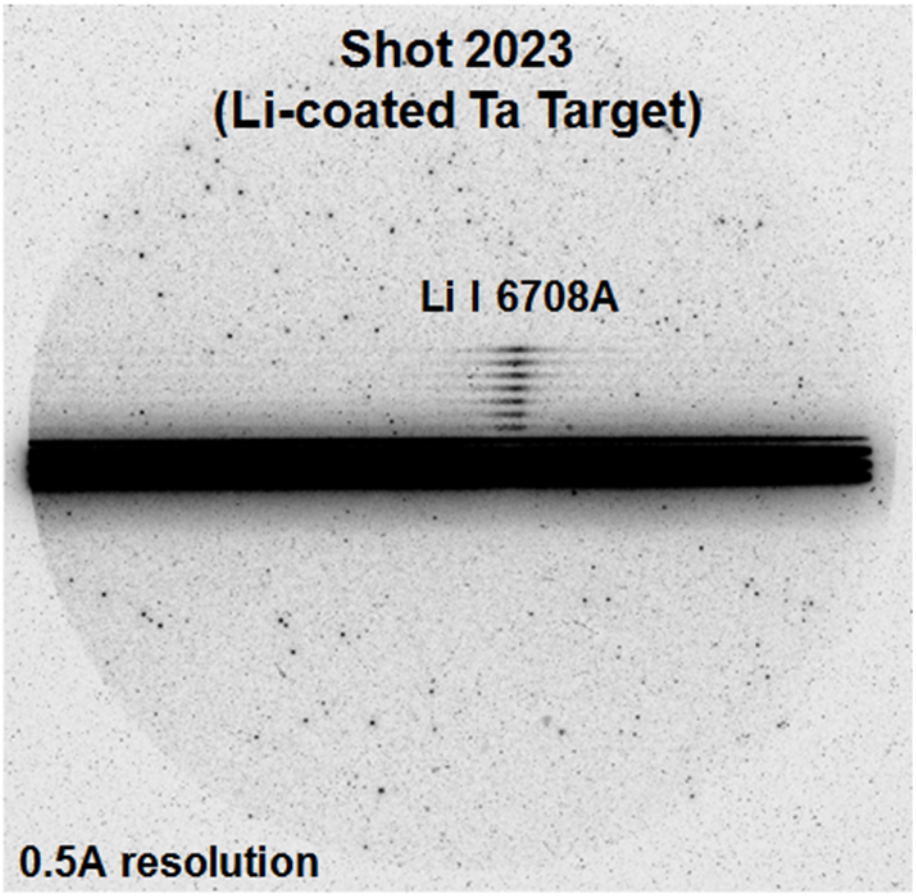

Figure 44. Raw spectral image of Li I (6708Å) spectra from Li-coated Ta target.

The spectrometer resolution for these measurements was 0.5Å and the spectra were collected over a 10ns window during the middle of the ~50nsec SMP radiation pulsewidth. Figure 45 shows the raw lineouts for the two fibers positions. As can be seen, fiber 6 (closer to the axis) has an asymmetric lineshape as compared to fiber 1. Electric field gradients can cause asymmetries due to shifts of the energy levels that are quadratic in E. Because the integrated line of sight is along a chord looking across the entire anode surface (figure 46), the resultant lineshape can be a convolution of several lineshifts due to varying E-fields across the target.

7.3. Data Analysis and Results for Radial Fiber Locations

The line studied was Li I 2s—2p transition at 6708Å. For the expected temperature and density values for the SMP diode (outlined in previous sections), the width of the Li I line should be 0.52Å at $n_e = 1x10^{17}$ cm^{-3} and $T_e = 3.5eV$, which is proportional to n_e, and varying with T_e as $T_e^{½}$.

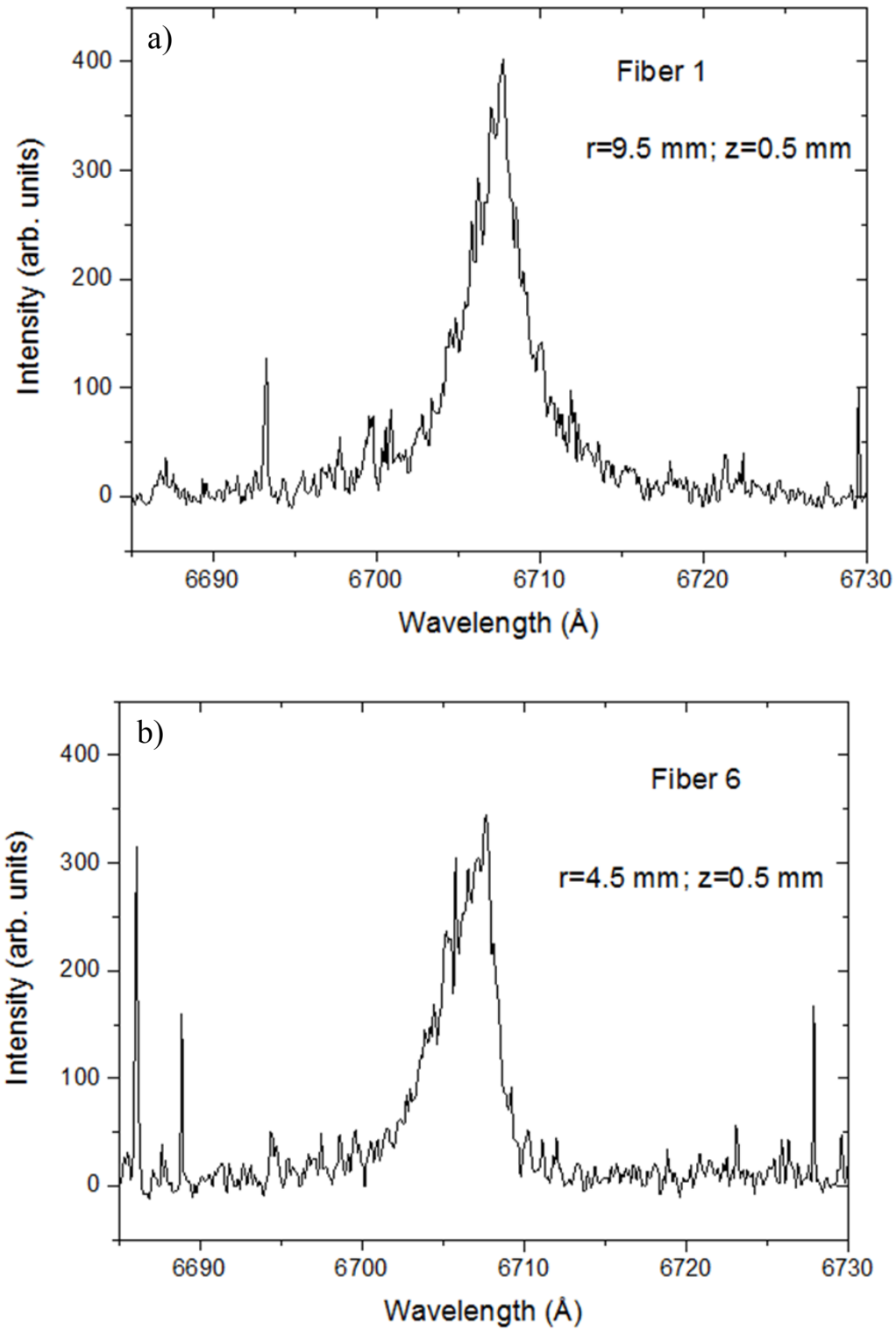

Figure 45. a) Lineout of the Li I 6708Å line at r = 9.5 mm from the axis. b) Lineout of the Li I 6708Å line at r = 4.5 mm from the axis.

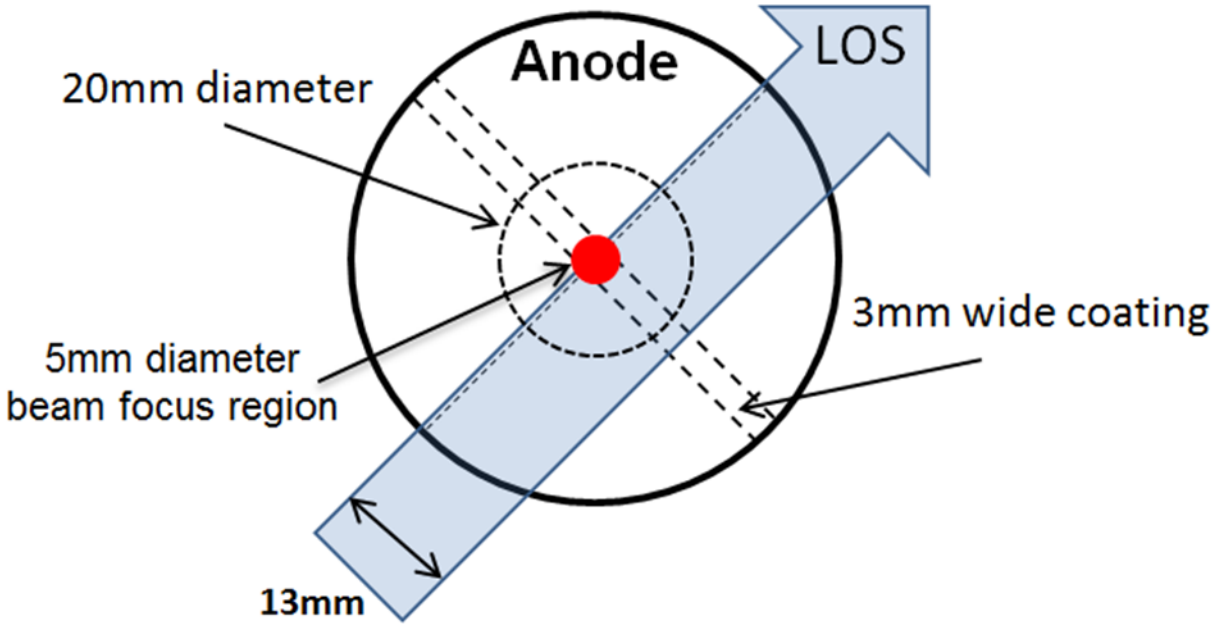

Figure 46. Orientation of fiber array LOS across target surface.

For fiber 1, we can fit a Lorentizian profile to the Stark broadened lineshape (figure 47). The line is symmetric and can be fitted with a single Lorentzian with a FWHM of 3.9Å. The fit gives a blue shift of 0.43±0.11Å, with the error bar based on the uncertainty of the wavelength calibration. A width of 3.9Å corresponds to $n_e \sim 7.3 \times 10^{17}$ cm^{-3}.

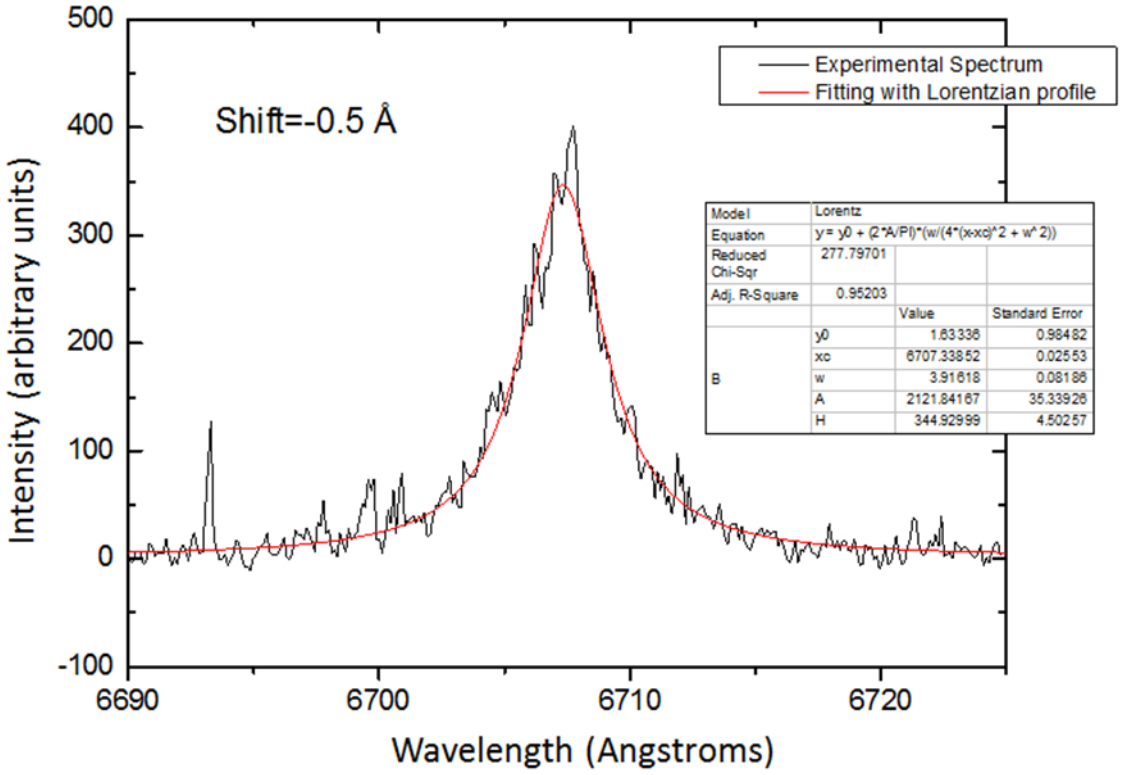

Figure 47. Lorentzian fit to experimental lineshape for Fiber 9 at r = 9.5 mm.

The stark shift at this density can be ~0.25Å, but the observed shift is higher, which indicates the presence of an electric field. The shift due to the electric fields would then be ~0.18Å. Figure 48 shows calculated Stark shifts due to electric fields for the Li I 6708Å line. A shift of 0.81±0.11Å corresponds to an electric field amplitude of ~1.55±0.55 MV/cm. Therefore, the average electric field at r = 9.5mm and z = 0.5mm is ~1.55±0.55 MV/cm. While this line could be fit assuming a single electric field, the asymmetric lineout at r = 4.5mm cannot.

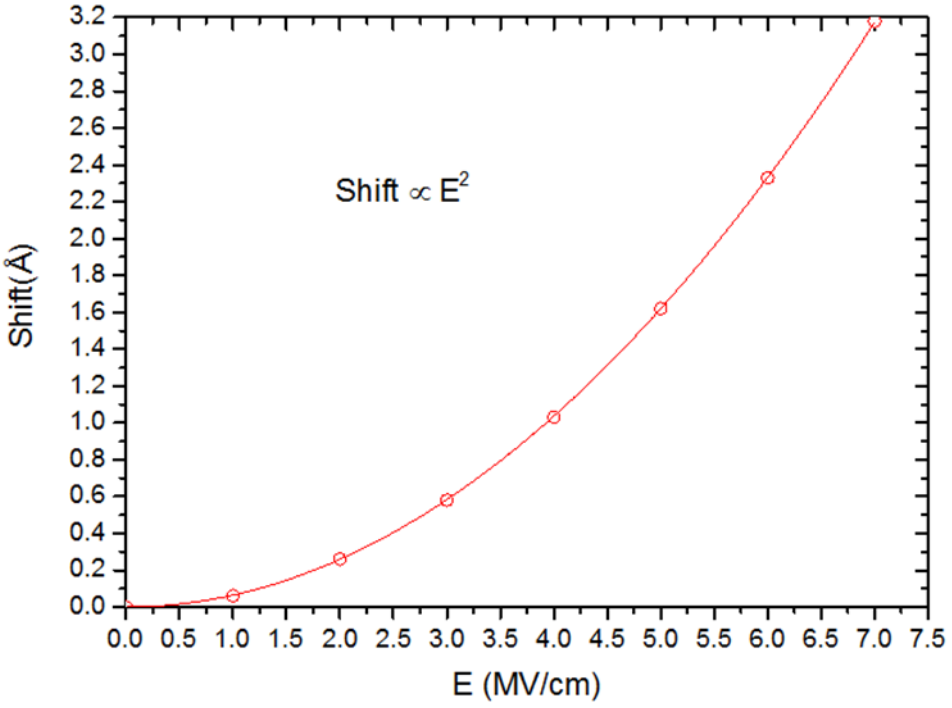

Figure 48. Calculated Stark shifts due to electric fields for the Li I 6708Å line.

For this lineout, three electric fields were assumed. These fields can be a result of different radial positions (integrated along the line of sight), axial variations across the 0.5mm wide region along the anode surface, and/or the collection time (10ns) of the spectra. Figure 49 shows the lineshape for the r = 4.5mm location, along with lineshapes for three different electric field strengths (3.0 MV/cm, 6.0 MV/cm, and 7.5 MV/cm), together with a Gaussian instrumental width of 0.5Å.

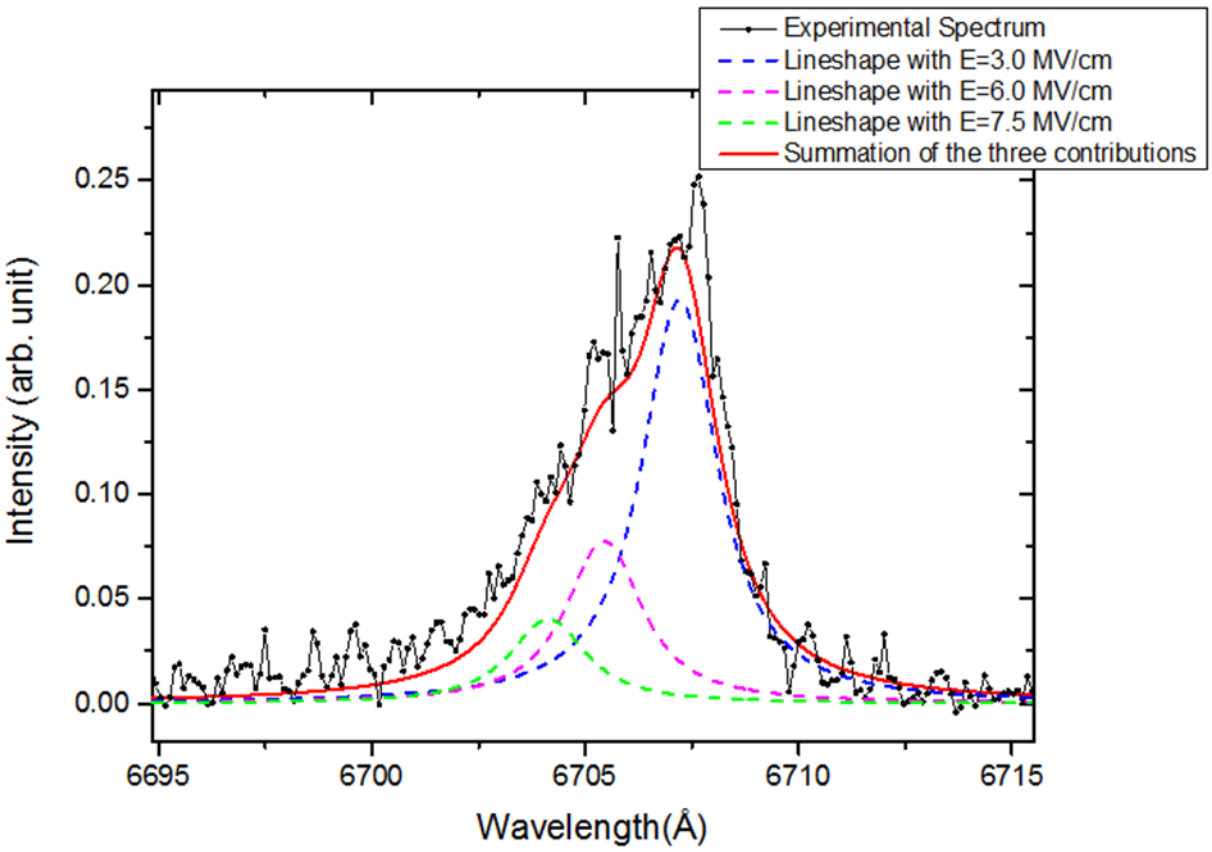

Figure 49. Lineshape obtained from the convolution of three different E-field strengths compared with the experimental profile.

Each lineshape is convoluted with a 2Å stark width, determined from a fit of the unaffected red side of the line. The summation of the three lineshapes with intensity ratios of 62:25:13, gives a good fit to the data. The Stark width of 2Å, corresponds to an electron density of ~3.8×10^{17} cm^{-3}. At this density, the Stark shift will be 0.13Å, which is much less than the observed shift of 0.64Å. Therefore, the E-field values obtained from the fits, will be little effected by this. The uncertainty of ±0.11A in the wavelength gives an error of ±10% for the lower field values (E_1), the error will be less for the higher fields.

In conclusion, the electric field near the anode surface for the SMP diode was determined using emission spectra from the lithium neutral line (6708Å). Spectra from the outer region (r = 9.5mm) is symmetric and can be fit using a single Lorentzian profile. The blue shift of the line gives an upper limit of the electric field of ~1.5±0.5 MV/cm; however, this does not mean that

the fields are this low, as the lithium line emission may not occur outside of the dense surface plasma, where the electric fields would be unshielded. At r = 4.5mm, the spectra shows an asymmetry which cannot be explained with a single electric field. This asymmetry is due to the overlapping of multiple fields, of varying amplitudes. Electric fields in the range of 3-7.5 MV/cm give a good fit to the data. Due to spatial and temporal variations in the line of sight and gate time for the spectra, it is not possible to determine with any greater certainty from where the different fields are emanating in this shot.

7.4. Data Analysis and Results for Axial Fiber Locations

In an attempt to try and better locate the field distribution, another shot was attempted with a double fiber array, where two rows adjacent fibers were positioned along the surface as illustrated in figure 50.

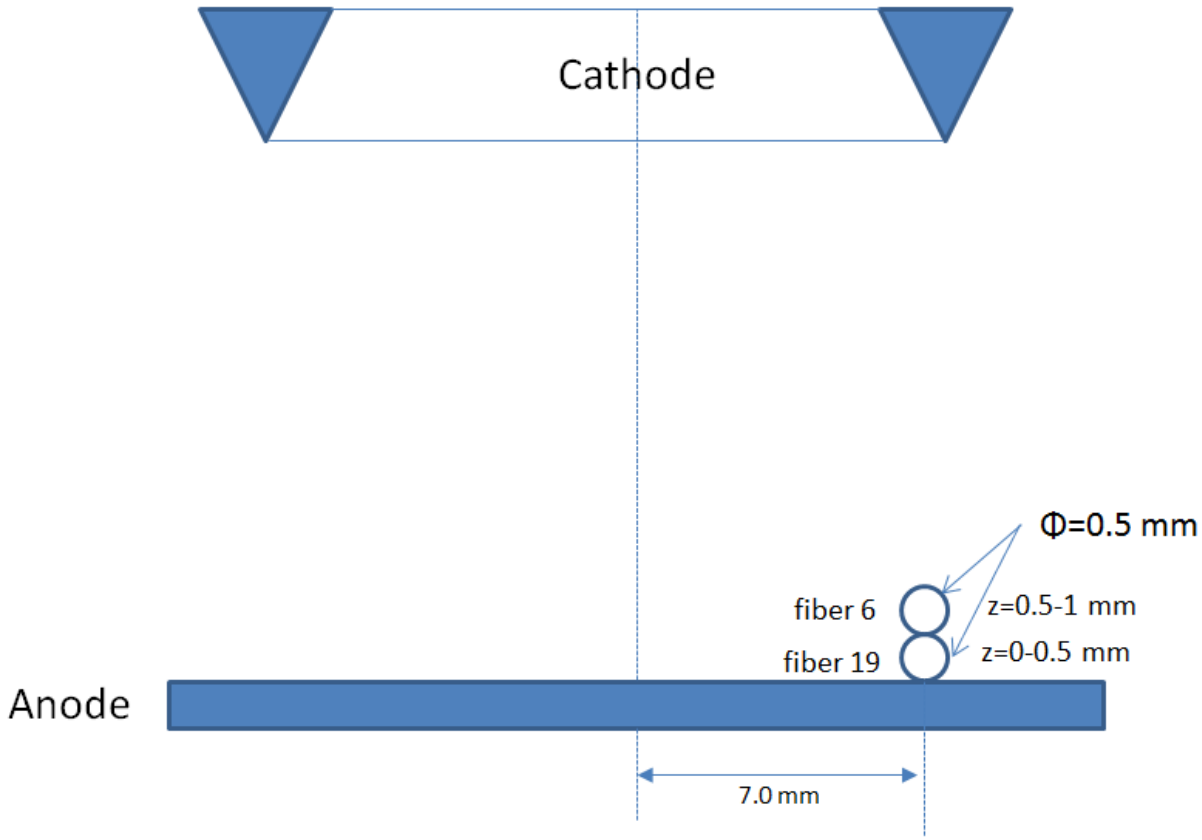

Figure 50. Orientation of the double fiber array across the target surface.

The spectrometer resolution in this case was slightly improved as well (0.4Å). Figure 51 shows two lineouts at r = 7.0 mm, at two axial locations, separated by 0.5 mm. Both spectra have asymmetric shapes, and the spectrum further from the anode surface is shifted more towards the blue due to higher (less shielded) fields there.

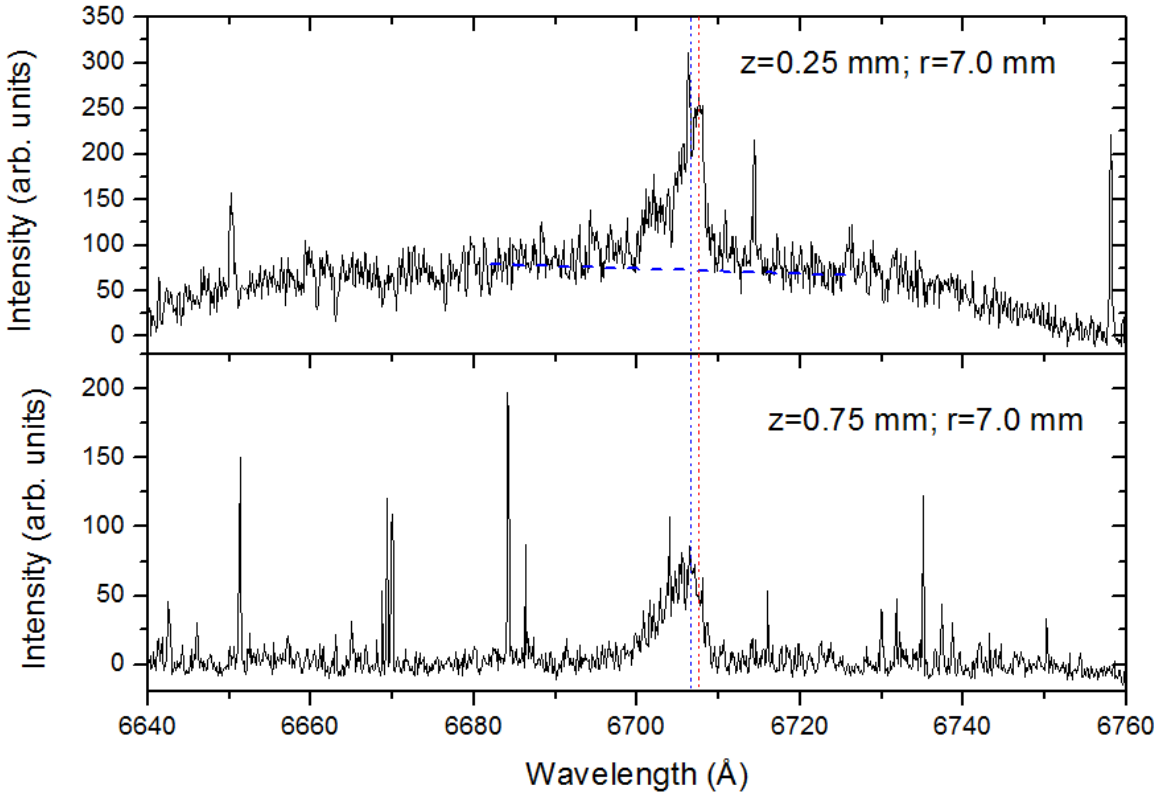

Figure 51. Spectral lineouts of adjacent fibers from the double array at r = 7.0 mm.

Figure 52a shows the lineout for the fiber further (0.75mm) from the surface with the corresponding lineshape fits for three electric field strengths (4MV/cm, 7MV/cm, and 9MV/cm), convoluted with a 0.4Å Gaussian instrumental width, as well as a 2.5Å Stark width obtained from the unaffected red side of the spectrum. The three lineshapes have an intensity ratio of 27:14:9, ranging from lowest to highest field. The stark width of 2.5Å corresponds to an electron density (n_e) of ~4.7×10^{17} cm^{-3}. This density gives a Stark shift of 0.16Å, which is much less than the observed 1.13Å, meaning the E-field values obtained from the lineshape fits are less affected than in the previous case. Figure 52b shows the lineprofile for the inner fiber (r = 0.25mm). This line shape was fit with four different electric field profiles (1.5MV/cm, 5.5MV/cm, 7.5MV/cm, and 9.5MV/cm), together with a Gaussian instrumental width of 0.4Å.

For this case, the Stark width was 2Å, which corresponds to a density of ~3.8×10^{17} cm^{-3}, which gives a Stark shift of ~0.13Å. This can cause a decrease of the 1.5MV/cm lineshape to 1.0MV/cm, but will have little effect on the other fields. The summation of the intensity ratios is 26:10:7:7.

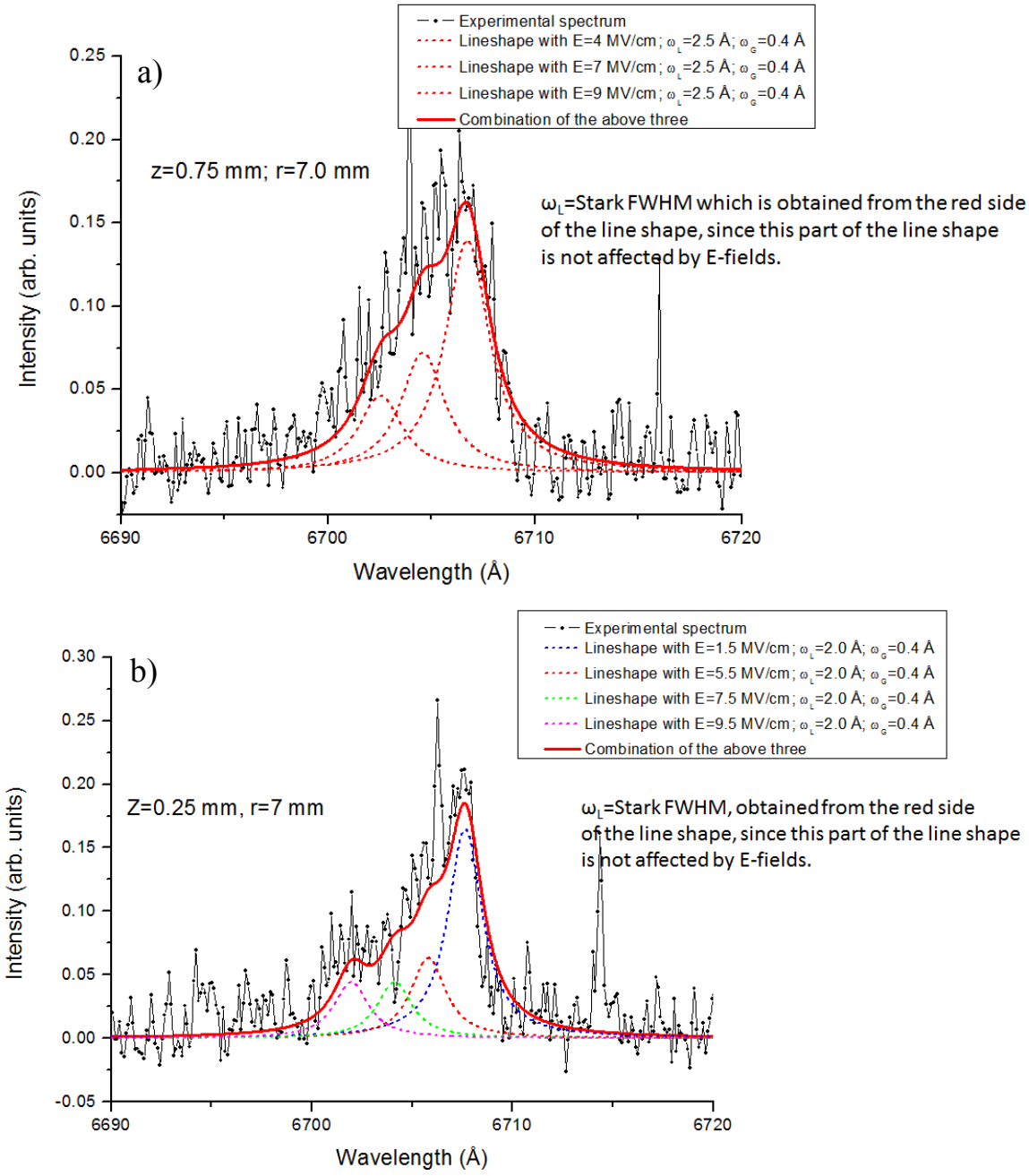

Figures 52. Lineouts for two adjacent fibers at r = 7.0 mm, fit with lineshapes convoluted from different E-field strengths.

In summary, for the two fibers positioned at different axial positions off the anode surface at the same radii, electric fields of 1.5-9.5 MV/cm were measured in the region closest to the anode, while fields of 4-9 MV/cm were measured in the region farther from the anode surface. One expects the electric fields to be higher further from the surface, and the average electric field is indeed higher further from the surface. Again, the spectra are gated over a 10 ns period, and it is possible that the magnitude of the E-field is changing over this time period. As the plasmas propagate outward from the surface, the E-field at the surface can drop while it remains higher further out; this is likely the reason for the low 1.5 MV/cm fields, which are only measured on the inner fiber.

7.5. Conclusions

As shown on RITS, this method provides a powerful technique to determine MV/cm E-fields within pulsed-power devices. While these shots used the lithium neutral line at 6708Å, which was applied as a dopant to the anode, other lines from higher charge states can be used as well (ex. Al III 4529Å), depending on the plasma conditions. Since the electric fields are greatly shielded by the dense electrode plasmas, suitably strong lines are necessary to be able to measure further out into the vacuum gap, where the plasma densities are much lower. This type of measurement is also conducive to such techniques as active dopants, where plasma is injected into the gap, prior to the main drive pulse. This type of technique (figure 53) is currently being studied for applications on Z in the not too distant future.

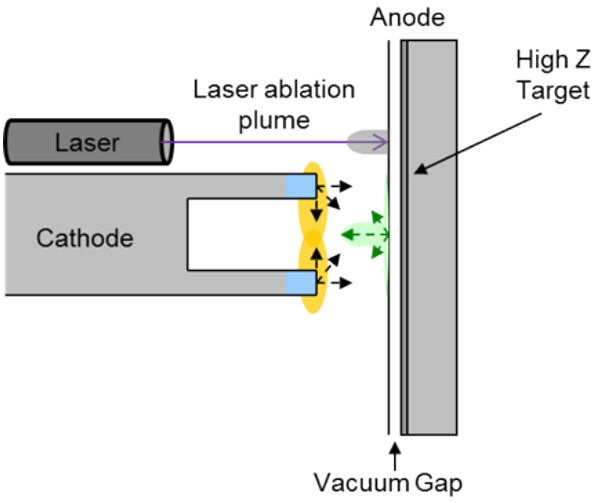

Figure 53. Illustration of one method proposed for injecting plasma into the A-K gap of a pulsed-power diode prior to the main pulse.

8. Z MACHINE EXPERIMENTS

8.1. Introduction

Part of this LDRD involved experiments on the Z machine which is located at Sandia National Laboratories [52]. The Z machine is a large pulsed-power device, which consists of 36 Marx banks oriented in a circular fashion. Each Marx bank is connected to a pulse-forming network which compresses and combines the individual lines into one line that drives an experimental load at the center of the machine. The Z machine can deliver current loads of up to 27MA with voltages between 1-2 MV at the load. These types of currents are used to create conditions suitable for a variety of high energy density physics experiments, including: dynamic material studies, inertial confinement fusion, and various astrophysical phenomena associated with black holes, stars, and large planets. Power is delivered on the Z machine by use of magnetically insulated transmission lines. These lines are joined together near the load by the use of a post-hole convolute setup, which combines four MITLs into one [53].

Data was collected using the Streaked Visible Spectroscopy (SVS) systems on Z [4]. There are presently four active systems being used on Z. All four systems use the same 1 meter McPherson spectrometers, but two systems have NSTec L-CA-24 streak camera detectors that output onto Kodak T-Max 400 film, while the other two systems use a Sydor streak camera output onto an SI-800 CCD [54]. Two different ruled grating configurations were used for these measurements, a 150g/mm grating which covers a useful wavelength range of ~220nm, with a resolution of 10 Angstroms, and a 600g/mm grating which covers a useful range of ~55nm with a resolution of 2.5 Angstroms. The implementation of the Sydor systems on Z corresponded with this LDRD, and so these experiments became the first on Z to use the new systems (figure 54). The new Sydor streak cameras have a Photonis P510 series streak tube with up to 5 picosecond temporal and 10 lp/mm spatial resolution. The 35mm photocathode is S20 on a sapphire window, with a P22N phosphor output. The photocathode sensitivity peaks at 45mA/W at 500nm. The dynamic range has ~100x gain. The output is recorded on a 2048 x 2048 pixel Spectral Instruments SI-800 CCD camera, with 13.5 microns pixel size and 90,000 electrons full well. Adding these systems has greatly increased the efficiency of the SVS diagnostic on Z. The collection and calibration of the data is all done electronically in real-time, eliminating the need for film development and calibration.

Light was collected using an achromatic lens and transmitted through approximately 74 meters of optical fiber. Detailed results from the 26 shots fielded on Z as part of this LDRD project will be given in a separate SAND report currently in preparation.

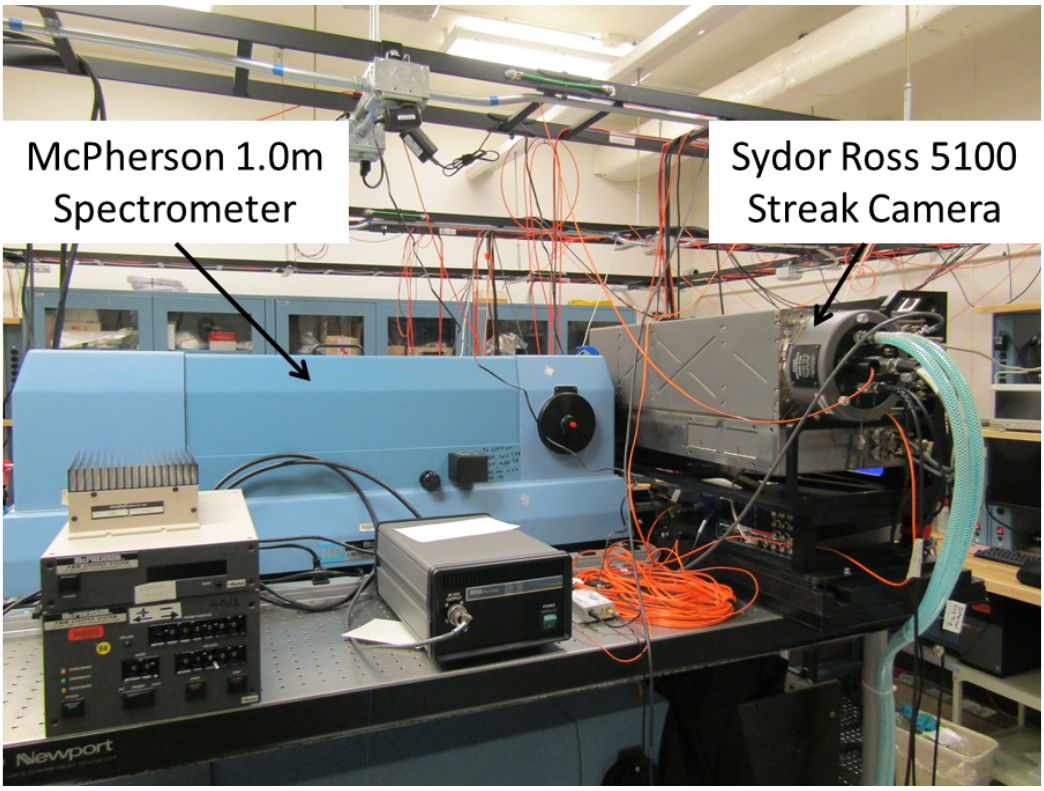

Figure 54. 1.0 meter McPherson Model 6061 Monochromator with Sydor Ross 5100 Streak Camera.

9. CONCLUSIONS

This LDRD resulted in the development of diagnostic methods and capabilities to measure plasma parameters and fields in pulsed-power diodes such as RITS and Z, using visible spectroscopy. While relatively common in the laboratory setting, the ability to field such diagnostics in the hostile environments encountered on large pulsed-power machines such as Z, has been limited. Intense x-ray and neutron backgrounds, large high energy particle fluxes, electromagnetic noise, combined with small and inaccessible geometries, make fielding these diagnostics extremely challenging. In addition, rapidly changing plasmas with large density and temperature gradients, viewed along integrated lines of sight that are surrounded by highly reflective metal surfaces, not only make the collection of data difficult, but unfolding and deconvolution extremely challenging as well. By tapping the knowledge and expertise of many years of combined research in these areas, this LDRD was able to make significant steps forward in the ability to diagnose plasmas and fields in pulsed-power environments. It is the hope that these types of measurements will continue in the years to come, as optical spectroscopy is likely the only practical means available for studying plasma formation, field strength, and current loss in pulsed-power diodes.

While not everything originally envisioned as part of this LDRD was able to be completed, we did accomplish several important things regarding B-field measurements in pulsed power diodes. As part of this LDRD, the first localized B-field and current distributions measurements were made on the SMP diode using Zeeman splitting techniques. Zeeman splitting of the C IV 3s-3p and Al III 4s-4p lines was used to determine the azimuthal magnetic fields generated in a pinched electron beam diode. Using Ampere's Law, the enclosed current at multiple radial locations was determined. From the data, it was shown that current extends radially outward beyond what was predicted based on the e-beam focus, deduced from the x-ray spot size and total dose measurements. These techniques were then extended to the Z machine, where experiments are now proceeding to reproduce these measurements at the load and at various power flow locations.

This LDRD, was also the first to quantify shielding of the magnetic field by electrode plasmas in pulsed-power diodes. The radial distribution of the azimuthal magnetic field generated by the

electron beam in the SMP diode was determined as a function of distance from the anode surface. Results were compared with the magnetic-field diffusion equation which determined the plasma resistivity was consistent with Spitzer resistivity, estimated from the electron temperatures determined from line ratio analyses. This is the first experimental determination of magnetic field shielding in a particle-beam diode. Finally, electric fields were determined from shifts of the Li I 6708Å 2s-2p transition. The spectra show asymmetric shifts towards the blue, which vary radially outward from the beam axis. The line-shape fits to these spectra are a convolution of several e-fields crossed by the chordal lines of sight of the fiber arrays across the diode. Electric fields in the range of 1.5-9.5 MV/cm were measured with an uncertainty of 10%. In addition to fields, carbon line ratios were used to determine plasma temperatures in the SMP diode. The ratio of the CIII/CIV lines gave electron temperatures in the 5-6eV range. Electron densities were determined from Stark broadening of various lines, including Al III, C II , C IV, H-alpha. The lineshapes were deconvoluted into Gaussian and Lorentizian components from Voigt profiles to separate the individual contributions of instrumental, Doppler, and Stark broadenings. Close to the anode surface, lineshapes were fit using two densities, one for the higher density surface plasma (responsible for the magnetic shielding), and the other for the lower density off-surface plasma. Electron densities in the $1\text{-}4\times10^{16}$ cm^{-3} range were obtained for the lower densities and $1\text{-}5\times10^{17}$ cm^{-3} for the higher density components.

Many diagnostic firsts were achieved as part of this LDRD project, including the first fielding of a multifiber array for SVS on Z, with seven fibers in a 1D orientation, which allowed the entire A-K gap to be spanned in a single shot. This followed upon RITS work where 26 fibers were fielded on a single line of sight. Avalanche photodiodes were first fielded on Z as well, looking at time and space resolved plasma light emission in the power flow regions. These detectors exhibit a very high multiplication rate and gain, which allow them to measure the earliest light emitted, corresponding to the initial heating of the electrode surfaces. Sonal Patel (Org. 1656) is currently using these detectors to make measurements of the electrode surface temperatures early in the Z pulse, to be used as input for plasma computer modeling, providing initial conditions for electrode heating and desorption processes. Finally, while not glamorous, much work was also done on investigating focusing and collimating optics, as well as the use of windows to reduce particle fluxes onto the optics, and prevent unwanted surface plasma formation.

In conclusion, there is still a lot to be done, such as improved lines of sight, without geometric obstacles and walls, which will greatly reduce unwanted plasma light and reflections. As shown during the Power Flow shot series on Z, when walls were removed, emission lines were measured, rather than the usual absorption lines. Being able to measure emission lines, greatly increases the amount of information that can be collected, as many of the higher charge state transitions are not visible in absorption, due to the effects of a strong continuum backlighter. Additionally, improved alignment fixtures, which allow for accurate positioning of arrays within the Z hardware, would greatly increase the reliability and reproducibility of these measurements.
The authors are grateful to all of the support personnel on RITS and Z, without whom these experiments would not have been possible. Thank you.

REFERENCES

1. M. E. Cuneo, P. Griffin, D. Balch, K. S. Bell, *et al*., "Hostile Environments on Z Grand Challenge LDRD," SAND2016-11385, Sandia National Laboratories, Albuquerque, NM, December 2017.
2. Y. Maron, E. Sarid, E. Nahshoni, and O. Zahavi, "Time-dependent spectroscopic observation of the magnetic field in a high-power-diode plasma," Physical Review A, 39, pp. 5856-5862, 1989.
3. B. V. Oliver, K. Hahn, M. D. Johnston, and S. Portillo, "Advances in High Intensity E-Beam Diode Development for Flash X-ray Radiography," Acta Physica Polonica-Series A General Physics, 115, no. 6, 1044, 2009.
4. M.R. Gomez, R.M. Gilgenbach, M.E. Cuneo, C.A. Jennings, *et al*., "Experimental Study of Current Loss and Plasma Formation in the Z machine Post-hole Convolute," Physical Review Accel. & Beams, 20, 010401, 2017.
5. M.E. Cuneo, "The Effect of Electrode Contamination, Cleaning, and Conditioning on High-Energy, Pulsed Power Device Performance," IEEE Trans. Dielectric Electrical Insulation, **6**, pp. 469-485, 1999.
6. D.J. Griffiths, Introduction to Electrodynamics, 3rd ed., Prentice Hall, New Jersey, 1999.
7. LSP is a software product developed by ATK Mission Research, Albuquerque, NM 87110, with initial support from the Department of Energy SBIR Program.
8. D. V. Rose, D. R. Welch, T. P. Hughes, R. E. Clark, *et al.*, "Plasma evolution and dynamics in high-power vacuum-transmission-line post-hole convolutes," Phys. Rev. ST-Accel. & Beams, 11, 060401, 2008.
9. D. V. Rose, D. R. Welch, R. E. Clark, E. A. Madrid, C. L. Miller, C. Mostrom, W. A. Stygar, M. E. Cuneo, C. A. Jennings, B. Jones, D. J. Ampleford, and K. W. Struve, "ZR-convolute analysis and modeling: plasma evolutions and dynamics leading to current losses," IEEE Pulsed Power Conf. (2009).
10. C. D. Turner, T. D. Pointon, K. L. Cartwright, "EMPHASIS/Nevada Unstructured FEM Implementation Version 2.1.1.," SAND2014-16737, Sandia National Laboratories, Albuquerque, NM, August 2014.
11. D. J. Ampleford, C. A. Jennings, B. Jones, S. B. Hansen, M. E. Cuneo, *et al*., "K-shell emission trends from 60 to 130 cm/ls stainless steel implosions," Phys. of Plasmas, 20, 103116, (2013).
12. S. A. Slutz, M. C. Herrmann, R. A. Vesey, A. B. Sefkow, D. B. Sinars, D. C. Rovang, K. J. Peterson, and M. E.Cuneo, "Pulsed-power-driven cylindrical liner implosions of laser preheated fuel magnetized with an axial field," Phys. Plasmas, 17, 056303, 2010.
13. D. L. Johnson, R. Altes, V. Bailey, P. Corcoran, I. Smith, S. Cordova, F. Griffin, K. Hahn, D. Jaramillo, J. Maenchen, *et al*., "Rits-6, a 10-MV inductive voltage adder accelerator," Proceedings of the 13th International Symposium on High Current Electronics, pp. 115–118, 2004.

14. J.E. Maenchen, G. Cooperstein, J. O'Malley, and I. Smith, "Advances in Pulsed Power-Driven Radiography Systems," Proc. IEEE, 92, 1021, 2004.

15. K. Hahn, N. Bruner, M.D. Johnston, B.V. Oliver, *et al*., "Overview of the Self-Magnetic Pinch Diode Investigations on RITS-6," IEEE Trans. on Plasma Science, 38, 2652, 2010.

16. A. Lewis, J. Rohrer, "Gen IV Streak Camera Manual, Rev. A" Bechtel Nevada, Los Alamos Operations, Los Alamos, NM 87544, July 2015.

17. Spectral Instruments Inc. 420 N. Bonita Ave . Tucson, AZ 85745 . Ph. 520-884-8821 Fax 520-884-8803, Email info@specinst.com, Web www.specinst.com.

18. Princeton Instruments SpectraPro® 2150, 150 mm monochromator/spectrograph.

19. Princeton Instruments IsoPlane® SCT 320, 300 mm imaging spectrograph.

20. R.W. Olsen, "EG&G, Inc., Fast Streak Camera Operation," SPIE-High Speed Photography, Videography, and Photonics VI, 981, 71 (1988).

21. Pi-Max/Pi-Max 2 system, ftp://ftp.princetoninstruments.com/public/Manuals/ Princeton%20Instruments/PI-MAX%20System% 20Manual.pdf.

22. National Securities Technologies, LLC., Los Alamos Operations, P.O. Box 809 Los Alamos, NM 87544. Technical Specifications Form, 200MHz VISAR APD Receiver.

23. Hamamatsu Catalog Number KAPD1001E05, April 2004.

24. M. Ingle, "Ultra2 8-Way 500 Million Frame Per Second Intensified Camera," Manual # UMCCDULTRA8-1, Version 1, July 2011. Photek Ltd, 26 Castleham Road, St. Leonards-on-Sea, East Sussex, United Kingdom TN38 9NS.

25. Princeton Instruments Quad-RO: 4320 CCD camera manual

26. Polymicro Technologies, LLC, 18019 North 25th Avenue Phoenix, Arizona 85023 Phone: (602) 375-4100, Fax (602) 375-4110. URL: http://www.polymicro.com.

27. G.V. Marr, Plasma Spectroscopy, Elsevier Publishing Co., London, 1968.

28. G. Bekefi, Principles of Laser Plasmas, John Wiley & Sons, Ltd., New York, (1976).

29. H.R. Griem, Plasma Spectroscopy, McGraw-Hill, New York, 1964.

30. R.H. Huddlestone and S.L. Leonard, Plasma Diagnostic Techniques, Academic Press, New York (1965).

31. Prism Computational Sciences Inc., PrismSPECT, 1998.

32. J.T. Davies and J.M. Vaughan, "A New Tabulation of the Voigt Profile," Journal of Astrophysics, 137, 1302, 1963.

33. H.R. Griem, Spectral Line Broadening by Plasmas, Academic Press, New York (1974).

34. M. S. Dimitrijevi´c and N. Konjevi´c, "Stark widths of doubly-and triply-ionized atom lines," Journal of Quantitative Spectroscopy and Radiative Transfer, 24, no. 6, pp. 451–459, 1980.

35. M.A. Gigosos, and V. Cardeñoso, “New plasma diagnosis tables of hydrogen Stark broadening including ion dynamics,” Journal of Physics B: Atomic, Molecular, and Optical Physics, 29, 4795, 1996.

36. N. Bennett, D. R. Welch, T. J. Webb, M. G. Mazarakis, M. L. Kiefer, M. D. Crain, D. W. Droemer, R. E. Gignac, M. D. Johnston, J. J. Leckbee, *et al*., “The impact of plasma dynamics on the self-magnetic-pinch diode impedance,” Phys. of Plasmas, 22, no. 3, p. 033113, 2015.

37. D. J. Griffiths, Introduction to Quantum Mechanics. Pearson, 2013.

38. D.H. Goldstein, Polarized Light, 3rd ed., CRC Press, Boca Raton, FL, 2011.

39. S. Patel, Optical Spectroscopy and Magnetic Field Profile Measurements on the Self Magnetic Pinch Diode, Ph.D. thesis, University of Michigan, 2016.

40. N. Bruner, D. R. Welch, K. D. Hahn, and B. V. Oliver, “Anode plasma dynamics in the self-magnetic-pinch diode,” Physical Review Special Topics-Accelerators & Beams, 14, no. 2, p. 024401, 2011.

41. E. Stambulchik, K. Tsigutkin, and Y. Maron, “Spectroscopic method for measuring plasma magnetic fields having arbitrary distributions of direction and amplitude," Phys. Rev. Lett. 98, 225001, 2007.

42. S. Tessarin, D. Mikitchuk, R. Doron, E. Stambulchik, E. Kroupp, Y. Maron, D. Hammer, V. Jacobs, J. Seely, B. Oliver, and A. Fisher, “Beyond Zeeman Spectroscopy: Magnetic-field diagnostics with stark-dominated line shapes," Phys. Plasma 18, 093301, 2011.

43. R. Doron, D. Mikitchuk, C. Stollberg, G. Rosenzweig, E. Stambulchik, E. Kroupp, Y. Maron, and D. A. Hammer, “Determination of magnetic fields based on the Zeeman effect in regimes inaccessible by Zeeman-Splitting Spectroscopy," High Energy Density Phys. 10, 56 (2014).

44. N. Konjevic, A. Lesage, J. R. Fuhr, and W. L. Wiese, “Experimental stark widths and shifts for spectral lines of neutral and ionized atoms (a critical review of selected data for the period 1989 through 2000)," J. Phys. Chem. Ref. Data, 31, 819 (2002).

45. E. Stambulchik and Y. Maron, “A study of ion-dynamics and correlation effects for spectral line broadening in plasma: K-shell lines," J. Quant. Spectrosc. Radiat. Transf., 99, 730, 2006.

46. F.F. Chen, Introduction to Plasma Physics and Controlled Fusion, 2nd ed., Plenum Press, New York (1984).

47. J. Lyman Spitzer, Physics of Fully Ionized Gases, Interscience Publishers, 1962.

48. J. Bailey, A. B. Filuk, A. L. Carlson, D. J. Johnson, P. Lake, *et. al*., “Measurements of Acceleration Gap Dynamics in a 20-TW Applied-Magnetic-Field Ion Diode,” Phys. Review Letters, 74, 1771, 1995.

49. A.B. Filuk, J. E. Bailey, A. L. Carlson, D. J. Johnson, P. Lake, *et. al.,* “Charge-Exchange Atoms and Ion Source Divergence in a 20 TW Applied-B Ion Diode,” Phys. Review Letters, 77, 3557, 1996.

50. Y. Maron, M. D. Coleman, D. A. Hammer, and H.-S. Peng, "Measurements of the Electric Field Distribution in High-Power Diodes," Phys. Review Letters, 57, 699, 1996.

51. Y. Maron, M. D. Coleman, D. A. Hammer, and H. S. Peng, "Experimental determination of the electric field and charge distribution in magnetically insulated ion diodes," Physical Review A, 36, 2818, 1987.

52. D. H. McDaniel *et al*., in Proceedings of the 5th International Conference on Dense Z Pinches, American Institute of Physics, Melville, NY, 2002, p. 23.

53. D. V. Rose, D. R. Welch, C. L. Miller, R. E. Clark, E. A. Madrid, *et al*., "10^7-A load-current B-dot monitor: Simulations, design, and performance," Phys. Rev. ST Accel. & Beams 13, 040401, 2010.

54. Sydor Instruments, LLC, 291 Millstead Way Rochester, NY 14624, Phone: 585-278-1168, http://sydortechnologies.com/, info@sydorinstruments.com, ROSS 5100 Streak Camera Product Specifications Sheet.

APPENDIX A: SPECTROSCOPY SHOTS ON RITS

Spectroscopy Shot Series I (May 2015)

Shot 1908: Standard Al foil with cap; 47nsec; CIV lines (very weak)

Shot 1909: Al foil, flat-foil holder, version 1; 38nsec; CIV lines (very, very weak)

Shot 1910: Al foil, flat-foil holder, version 2 (poor pulsed-power); N/A; CIV and Al III lines

Shot 1911: Al foil, anode heating hardware; 40nsec; No lines, continuum

Shot 1912: Al-mylar foil; 22nsec; CIV and CIII lines (very, very weak)

Shot 1913: Graphite foil; 27nsec; No lines (very weak continuum)

Shot 1914: Aerodag on Al foil; 21nsec; No lines, continuum

Shot 1915: Solid Ta target; 44nsec; CIV and CIII lines (weak, no obvious splitting)

Shot 1916: Al-coated Ta (1 micron); 29nsec; No lines, continuum

Shot 1917: Al-coated Ta (thermal spray); 36nsec; CIV and Al III lines (some splitting)

Shot 1918: 2mm diameter W limited target in carbon substrate; 13nsec; CIV and C III (broadening, but no indication of splitting)

Shot 1919: Carbon-coated Ta target (1 micron); 33nsec; CIV lines (splitting visible) 580nm

Shot 1920: Si-coated Ta target (1 micron); 31nsec; CIV and C III (splitting visible) 575nm

Shot 1921: Bead-blasted Ta target with AWE oil on surface; 27nsec; CIV and C III (very weak splitting visible) (MgF2 AR coated windows added)

Shot 1922: 1mm diameter W limited target in aluminum substrate; 10nsec; CIV, C III, and Si III (weak spectra, no obvious line splitting) (Gain setting increased to 200)

Shot 1923: Solid W target; 28nsec; CIV and C III lines (weak with very if any indication of splitting)

Shot 1924: Al foil, flat foil holder, version 1, with slots cut to see behind the foil

Shot 1925: Al-coated Ta (thermal spray) 8.5mm geometry

Shot 1926: Al-coated Ta (thermal spray) 12.5mm geometry

Shot 1927: Carbon-coated Ta target (1 micron)

Spectroscopy Shot Series II (October 2015)

PI-Max Camera with Unigen Coating and 3 Inch Qioptiq Achromatic Lens (160mm fl)

Shot 2021: Na-coated Ta (1 micron); 45ns, 339R; Na I absorption lines and CIV emission

Shot 2022: Si-coated, Aluminum foil (0.5 micron); 14ns, 125R; no Si III lines (5740A).

PI-Max Camera with HBf Visible Coating and 2 Inch Edmund Optics Achromatic Lens (150mm fl) Added

Shot 2023: Li-coated Ta; 50ns, 333R; Lithium line (6708Å)

Shot 2024: Boron-coated, solid Ta; 38ns, 279R; (new 2" achromat added); BII (4122Å) line barely observed.

Shot 2025: Boron-coated, solid Ta; 16ns, 163R; continua, no BII (4122Å) line.

Shot 2026: Mg-coated, solid Ta; 44ns, 335R; no lines (MgI 5528Å)

Shot 2027: Al-coated, solid Ta (thermal spray); 29ns, 220R; Flatfield

New Double Fiber Array Added

Shot 2028: Al-coated, solid Ta (thermal spray); 50ns, 324R; ~2MV voltage drop at back-half of pulse; strong Al III and CIV lines.

Shot 2029: Na-coated, solid Ta; 48ns, 369R; Na I (5890A) absorption and emission.

Shot 2030: Si-coated, solid Ta; 40ns, 329R; (no framing camera image)

Shot 2031: 8.5mm heated, aluminum foil anode; 29ns, 154R

Shot 2032: Al-coated, solid Ta (thermal spray); 39ns, 303R; strong Al III lines (Al III 4480Å, 4512Å, and 4529Å).

Note: All shots with 12.5mm cathode and 12mm A-K gap except as noted.

Spectroscopy Shot Series III (November 2015)

PI-Max Camera with HBf Visible Coating and 2 Inch Edmund Optics Achromatic Lens (150mm fl) with 100 micron (13x2) Double Fiber Array

Shot 2035: Li-coated Ta (3mm perpendicular stripe); 48ns, 353R

Shot 2042: Na-coated Ta (3mm perpendicular stripe); 45ns, 363R, C IV lines

Shot 2043: C-coated Ta (3mm perpendicular stripe); 21ns, 155R

Shot 2044: Li-coated Ta (ring coating, center 20mm diameter uncoated); 27ns, 216R

Shot 2045: Al-coated Ta (thermal spray, 20mm diameter circle in center); 41ns, 300R, Al III and C IV lines.

Shot 2046: Al-coated Ta (3mm perpendicular stripe); 37ns, 254R, Al III and C IV lines.

Shot 2047: Li-coated Ta (20mm diameter circle in center); 38ns, 260R; Flatfield

APPENDIX B: FIRST SERIES OF SPECTROSCOPY SHOTS ON Z

For the first two years of this project, Ross Falcon (Org. 1683) lead the experimental effort to field SVS on Z shots, looking at plasma conditions in the power flow regions. Previous work by Matt Gomez *et. al*., had studied plasma formation on Z in the post-hole convolute region [4], but this was the first attempt to look closer to the load in the final feed section. Listed below are all the shots on which SVS was fielded, including a summary of the results/observations by Ross.

Shots series where SVS was fielded looking at power flow:

1. Nonthermal (z2775-2777) (March 2015): Liner
2. Opacity (z2832-z2835) (July 2015)
3. ZAPP (z2870-z2874) (Oct. 2015)
4. Cibola (z2886-z2887) (Nov./Dec. 2015)
5. Opacity (z2923-2927) (March 2016)
6. Large Convolute (z2935-z2936) (April 2016)
7. LCM (z2937-z2939) (April 2016)
8. MagLIF IMP High-AR (z2945-z2946) (April 2016): Liner
9. ZAPP (z2950-z2954) (May 2016)
10. Opacity (z2970-z2973) (June 2016)
11. Pisces (z2989) (August 2016)
12. MagLIF AR Scan (z3017-z3019) (Oct. 2016): Liner

Total shots: 39

The first shot series on which I fielded was Nonthermal (PI Ampleford), shots z2775–7. The line of sight was immediately before (upstream of) the final-feed gap. I did not have much success on these shots, only obtaining data from one shot, z2776. The data showed that I could measure weak absorption lines in the final-feed gap, but this was only H-alpha of the Balmer series of hydrogen.

This prompted several hardware modifications which were slowly implemented across several shot series. Having used a collimating lens, I noticed a significant decrease in signal, so I decided to focus my line of sight on the upper-cathode surface so that I could collect more photons. I also implemented hardware modifications that allowed me to observe the upper-cathode corner (upturn into the final-feed gap) and eventually the flat surface of the final-feed gap. I also included a limiting aperture to choke off incoming particles, fearing bombardment of these particles.

Having mixed results upon using a lens, I attempted two strategies: (1) continue to use a lens to focus on a flat surface and (2) remove the lens. Needing to observe spectral lines, I also tried

using aqueous-solution dopants, after getting approval from environmental safety and hazards (ES&H), and getting properly trained.

For the May 2016 series (PI Ampleford), I tried increasing the sturdiness of my optical setup by using bigger, thicker hardware. Yes, it resulted in strength and prevented misalignment, but it also became cumbersome and tedious to align.

I soon learned many subtle procedures to facilitate my shot schedule—when and how to label my load hardware and my optical fibers, when to perform some of my calibration measurements, with whom to interact to properly and safely retrieve data. Sometimes I would not collect data due to simple procedures that I could have easily carried out.

In the middle of 2016, I soon became disheartened with SVS3 due to its consistent failures to obtain data. I kept using the dependable SVS1 and SVS2, but I stopped using SVS3. In 2017, we received SVS4 and SVS5. Each of these systems is high quality. They obtain good data, but their user manuals are horrendous. Both systems needed to be returned to the manufacturer in New York—one system twice—to repair them. And these systems are not film systems. They are CCD systems, which is fine, but they are difficult to operate.

APPENDIX C: SECOND SERIES OF SPECTROSCOPY SHOTS ON Z

With the shutdown of RITS, personnel and resources were moved over to Z, where the plasma spectroscopy work continued from that started by Ross Falcon. Upgrades were made to the hardware, including the addition of lenses and multifiber arrays. The new SVS4/5 systems [54] were incorporated, as was a bank of avalanche photodetectors [22], which made use of the Shock-Breakout infrastructure on Z. Additional lines of sight and more extensive use of dopants, including multiple thin-film coatings, were explored. The first shots were fielded in Dec. 2016 on the Low-L MagLIF 16b series. Following that series, SVS was fielded on 24 shots in 2017, looking at various aspects of power flow (electrode temperatures, plasma expansion, magnetic fields, etc.). These 24 shots covered 10 shot campaigns, using 4 different load configurations. Three power flow regions were explored on these shots, including: the post-hole convolute, the final feed, and the load. This has been the most ambitious visible spectroscopy effort on Z to date, and it is expected that the results will go a long ways towards improving the understanding of plasmas and fields in high energy pulsed-power drivers. Below is a listing of all the shots where SVS was fielded in support of this LDRD starting in Dec. 2016. The chart lists the four active SVS systems, as well as the APDs and DET10 PIN photodiodes. An "X" indicates that the diagnostic was fielded on that shot. The numerals in the APD and PIN columns, give the total number of detectors used on that shot.

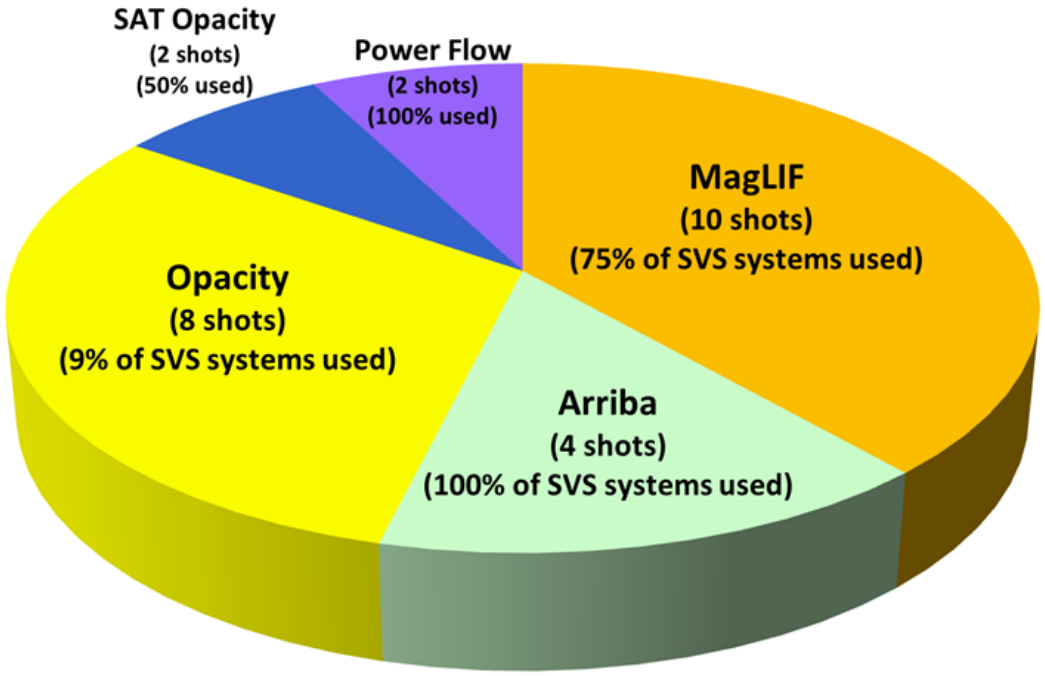

Figure C1. Breakdown of LDRD shots fielded on Z by experimental campaign, including average percentage of SVS systems fielded per campaign.

Listing of all shots where SVS was fielded on Z

Shot Number	Series	SVS1	SVS2	SVS4	SVS5	APDs	PINs
3038	Low-L 16b	X	X	X	X	2	0
3039	Low-L 16b	X	X	X	X	2	0
3048	Arriba 17a	X	X	X	X	2	0
3049	Arriba 17a	X	X	X	X	3	0
3053	SAT Opacity 17a			X	X	0	0
3055	SAT Opacity 17a			X	X	2	0
3074	Morphology 17a		X	X	X	3	1
3075	Morphology 17a		X	X	X	2	1
3076	Morphology 17a		X	X	X	4	1
3077	Morphology 17a		X	X	X	4	1
3084	Power Flow 17a	X	X	X	X	17	3
3086	Power Flow 17a	X	X	X	X	17	3
3087	AR Scan		X	X	X	4	3
3091	Opacity 17a					9	3
3092	Opacity 17a					9	3
3093	Opacity 17a					10	4
3094	Opacity 17a			X	X	8	2
3095	Opacity 17a				X	9	3
3123	StagMix 17a		X	X	X	2	1
3124	Arriba 17b	X	X	X	X	4	3
3125	Arriba 17b	X	X	X	X	5	3
3135	Morphology		X		X	3	2
3139	Opacity 17b					8	4
3140	Opacity 17b					8	5
3141	Opacity 17b					9	5
3143	Pre-Heat 17c			X	X	4	3
Totals	**26 shots**	**8**	**15**	**18**	**20**	**25**	**20**
Percentages	**26 shots (100%)**	**31%**	**58%**	**69%**	**77%**	**96%**	**80%**

* red indicates that no data was obtained although the diagnostic was fielded.

** maximum number of APDs that can be fielded are 17.

Table C1. Listing of all shots and systems fielded as part of the LDRD on the Z Machine.

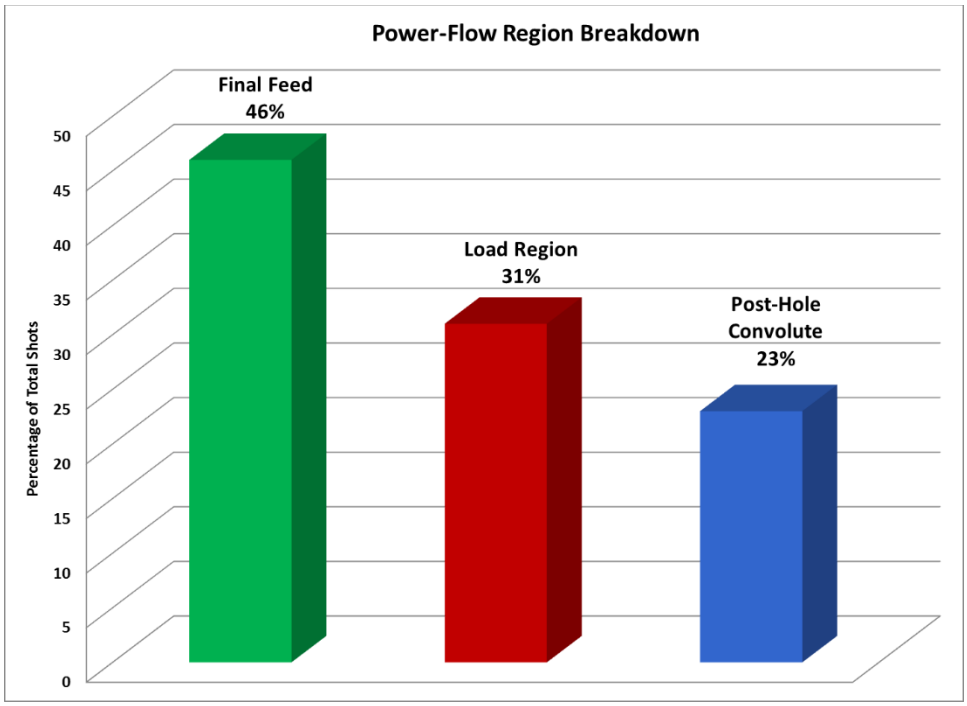

Figure C2. Percentage breakdown of power flow regions where LDRD experiments were conducted.

APPENDIX D: LINESHAPE CALCULATIONS FOR MAGNETIC FIELD MEASUREMENTS

Possibilities for magnetic-field diagnostics in the range 1 – 20 T

Table D1 gives the estimated minimal B-fields that can be determined in the density range $5\times10^{16} – 10^{18}$ cm^{-3} using Zeeman-split patterns in s – p doublets of Na I, C IV, Al III, and Si IV. The terms B_{par} and B_{per} represent lines-of-sight parallel and perpendicular to the B-field direction, respectively. Assumed spectral resolution is 0.3 Å (which generally only becomes a factor at the relatively low densities, below 10^{17} cm^{-3}). The maximum B that can be diagnosed for B_{par}, determined from the energy distance between the doublet components, is also indicated. When the line-of-sight is B_{per}, there is no practical limit on B since the σ-component that complicates the analysis in the high-B range can be easily removed from the spectrum employing a polarizer.

Transition	E_I (eV)	λ(Å)	n_e (cm^{-3})	$\Delta\lambda^{Stark}$(Å)	min. B_{par} (T)	min. B_{per} (T)	max. B_{par} (T)
			10^{18}	5	–	–	
Na I	5.1	5890,	5×10^{17}	2.5	–	–	
3s – 3p		5896	10^{17}	0.5	2	4	10
			5×10^{16}	0.25	1.5	3	12
			10^{18}	5	–	–	
C IV	64.5	5801,	5×10^{17}	2.5	8.5	–	15
3s – 3p		5812	10^{17}	0.5	2.5	4	20
			5×10^{16}	0.25	1.5	3	20
			10^{18}	6	20	–	35
Al III	28.5	5696,	5×10^{17}	3	10	18	40
4s – 4p		5722	10^{17}	0.6	2.5	4.5	50
			5×10^{16}	0.3	2	3.5	50
			10^{18}	1.4	11	20	*
Si IV	45	4089,	5×10^{17}	0.7	6	11	*
4s – 4p		4116	10^{17}	0.14	3	5	*
			5×10^{16}	0.07	3	5	*

* No practical limit

Table D1. Minimum B-fields that can be determined using Zeeman splitting.

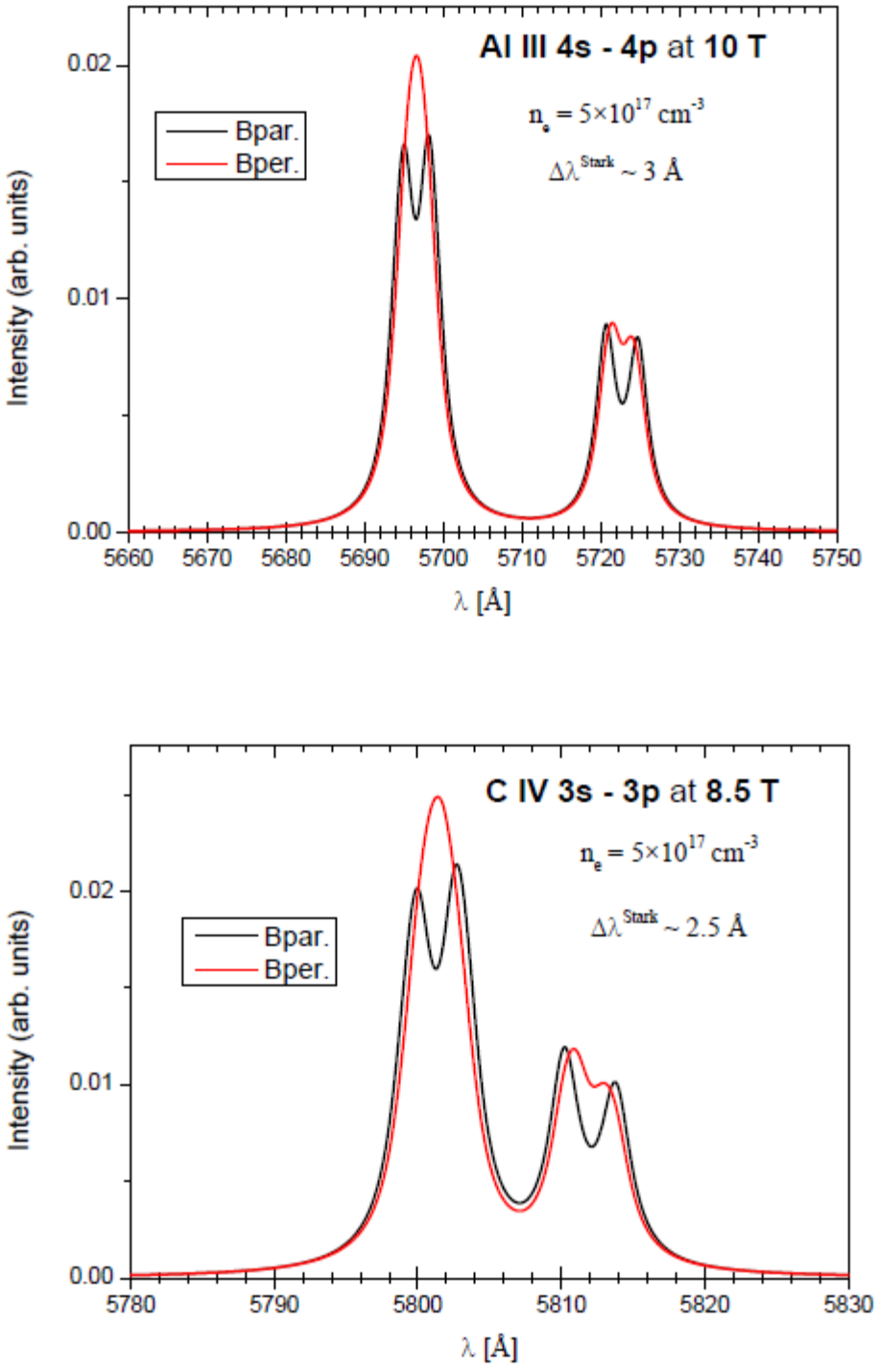

Figure D1. Parallel and perpendicular lineshape calculations for Al III and C IV lines.

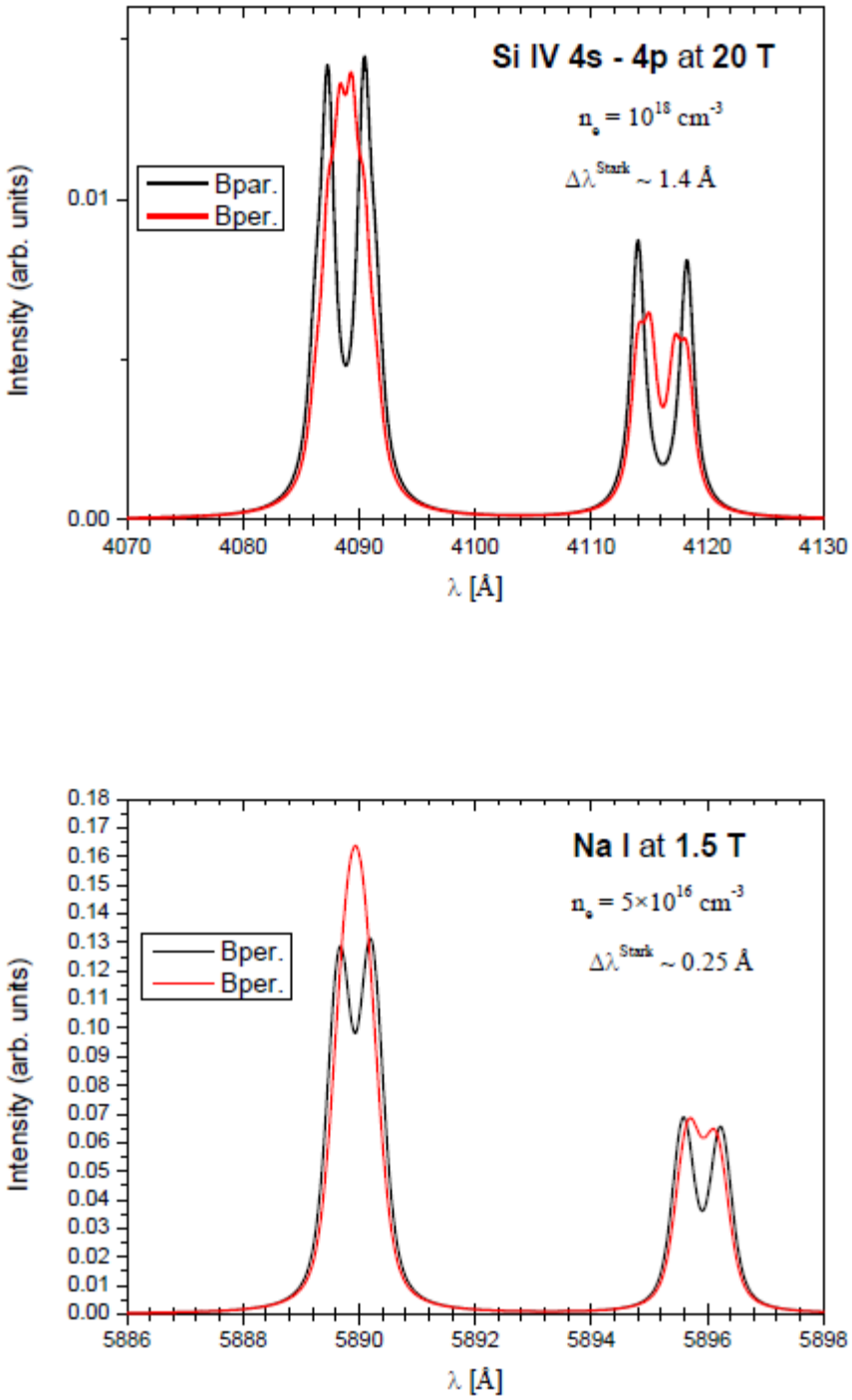

Figure D2. Parallel and perpendicular lineshape calculations for Si IV and Na I lines.

APPENDIX E: SAMPLE SPECTROSCOPY WORKSHEET FROM RITS

SHOT 2046

Setup: 80kV (8MV) Standard SMP shot, low Z MITL, 2.6uF Marx
Cathode: 85mm length (12.5mm outer diameter, 9.5mm inner diameter, through hole, 5mm silver paint. 0.015" flat tip
Anode: Al-coated tantalum target (thermal spray, 3mm wide stripe)
A-K Gap: 12.0mm
Vacuum Gap: N/A
Target: 1mm thick Al-coated (thermal spray) Ta target
Windows: 4.5" Borofloat Glass (MgF2 coated)
Anode Holder: Standard
X-ray Diagnostics: V-rolled edge and TRSD
Vacuum: $2x10^{-5}$ Torr
Notes: Tantalum surface is roughened from grit blasting

Shot Parameters
FWHM: 37ns
FWFM: 65ns
ESF Spot (V/H): 3.4/3.6mm
LSF Spot (V/H): 2.2/2.3mm
PSF Spot: 1.33mm
Dose: 254R
Cal. Factor (PIN_4): 3.58E8 (11/10/2015)
Gas Switch Timing: 0.76ns
PFL Spread: 21.1ns

TOF Distances:

Target to PIN_3: 4.0nsec
Target to PIN_4: 13.7nsec (in-between the wall)
Target to PIN_5: 4.0nsec
Target to PIN_6: 9.0 +/- 1nsec

PI-Max ICCD 1300HBf-filmless, 25mm Gen III intensifier, 20x20um, (1340x1300)

PI-Max-1300-HBf-25-FG-P43 (used since shot 2023)
Model: SPR4467M **System ID:** 131257-1-1
Serial Number: 08026412 (Purchased 2012)
Gate: 10ns (actual 9.2nsec)
Gain: 200
Internal Delay: 25ns
Gate Delay from Ext. Trig. In: 30ns
Aux Trig Out Delay: 0 nsec
ADC Rate: 100kHz
Detector Temperature: -20C (locked)
Background Counts (Trigger Check): 36 (average)
Slit Orientation: Radial, skimming the anode surface

Shot 2046

PI-Max Trigger Setup:

Output: PI-Max Trigger (TTL, Normal, 50 Ohms)
Delay: T + 191.379000μs (DG 535 #3, Channel A)
Delay: T + 725.000nsec (DG 535 #2, Channel A)
ICCD Monitor out Delay in DAS (PI_MON): 88.2ns
ICCD Aux. out Delay in DAS (AUXSOUT): 78.9ns

Spectrograph

Model: Princeton Instruments IsoPlane SCT-320
Serial Number: 32010318 (built in 9/15)
Grating: 2400g/m Visible Holographic
Slit: 50 micron
Total Path Length: 1569mm (5nsec)
Focal Length: 327mm
F-number: 4.6
Center wavelength: 575nm
Software: Winspec Version 2.6.11 July 2012

Turret #1: (S/N 32010318)
Grating #1: 2400g/mm hvis
Grating #2: 1200g/mm blazed at 500nm
Grating #3: 300g/mm blazed at 500nm

Calibration (setup in WinSpec)**:**

Pixel: 1	Wavelength: 564.605nm
Pixel: 670.5	Wavelength: 575nm
Pixel: 1340	Wavelength: 584.732nm

Spectrograph Input Optics

Lens: Achromatic pair (1:1.5 magnification)
ThorLabs (Part #MAP1050-75-A)
Input: 50mm FL, F/2.2
Output: 75mm FL, F/3.3
Object Distance: 37.7mm
Image Distance: 65.8mm

Notes: IsoPlane has silvered mirrors and gratings for higher throughput. Switched PI-Max camera with the one used previously for the framing images on shot 2023. This camera appears to have better resolution.

Shot: 2046

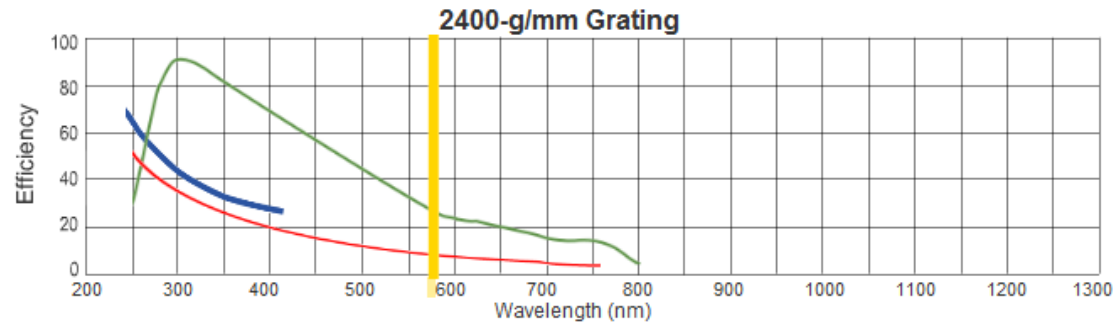

The grating curves show typical relative efficiency for the various blaze wavelengths and should be used as a comparison guide only.

Detector	PIMAX:1024x256-25mm		Center Wavelength(nm)	580 Enter	
Hor. pixel	961	Vert. pixels 253	Order	1	
Pixel Size µm	26	CCD width/mm 24.6	Select Excitation Laser	532 nm	
Linewidth,pixels	1.4		Laser wavelength,nm	532	
			Dispersion nm/mm	0.746	
Spectrograph	IsoPlane SCT 320		Bandwidth per pixel	0.019 nm	
Focal Length(mm)	327	Aperture ratio f/4.6	CCD Resolution(FWHM)	0.027	
Select Grating	2400 l		Center Wavenumber(cm-1)	17241.38	
Grooves/mm	2400		Next resolved wavelength	580.027	Grating Rotation > 40 deg.
Grating size/mm	68 x 68		Next resolved wavenumber	17240.58	Resolution,cm-1 0.8
CCD coverage	18 nm		Short Wavelength	570 nm	17544 cm-1
	545 cm-1		Long Wavelength	589 nm	16978 cm-1
nm to eV			Low Raman shift	1277 cm-1	High Raman shift 1818 cm-1

Note: Reduced resolution and throughput above 40 deg. grating rotation angle - grating rotation is 44.78 deg.

Fiber Array and Optics

Position: Bottom 45 degree port (225 degree position) 3" window
Fiber Number: 13x2 array (radially oriented, skimming the anode surface)
Fibers: 100 micron (Polymicro FVP100110125)
Delay: 52ns + fiber to slit (5.5") (0.5ns) + 34.5" (3ns) + 1569mm (5ns): **60.5ns**
Lens: 50.0mm, 150mm fl, Glass Achromat, F/3.0, Edmund Optics Part #49-285
Focal Spot Size: 0.5mm
Distance from Diode to outside of window flange: 29 11/16" (754mm)
Window: 75mm diameter Borofloat borosilicate, Edmund Optics Part #43-894 (uncoated)

Shot Results:

Trigger Background: 36 counts
Shot Background: 73 counts
Peak Intensity: 51,237 counts
Delay from PIN_4: 45nsec
Delay from IBEAM: 62nsec

Notes: New double fiber array added on shot 2028.

Shot 2046

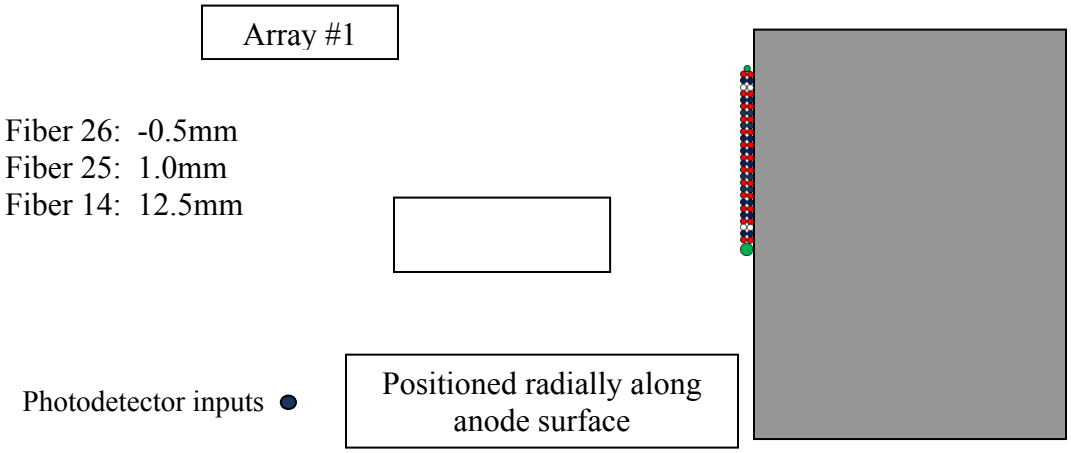

Pindiodes (NSTec APD; Model # H-EO-53):

APD_1: Fiber 13 (100µW, 0 knob setting) (400mV/div.)
APD_2: Fiber 14 (100µW, 0 knob setting) (400mV/div.)
APD_3: Fiber 15 (100µW, 0 knob setting) (400mV/div.)
APD_4: Fiber 16 (100µW, 0 knob setting) (400mV/div.)
APD_5: Fiber 17 (100µW, 0 knob setting) (400mV/div.)
APD_6: Fiber 19 (100µW, 0 knob setting) (400mV/div.)
APD_7: Fiber 20 (100µW, 0 knob setting) (400mV/div.)
APD_8: Fiber 21 (100µW, 0 knob setting) (400mV/div.)
APD_9: Fiber 22 (100µW, 0 knob setting) (400mV/div.)
APD_10: Fiber 23 (100mW, 0 knob setting) (400mV/div.)
APD_11: Fiber 24 (100mW, 0 knob setting) (400mV/div.)
APD_12: Fiber C (100mW, half knob setting) (400mV/div.)

Delay: 53ns + 1.5ns jumper + 34.5” (3ns) = **57.5ns** (APD’s 1-10)
Filter: N/A

Notes: 100 micron jumper fibers (12”) into APD detectors

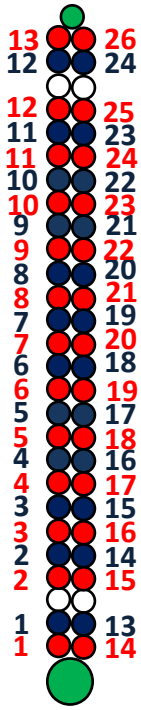

Shot 2046

Plasma Imaging Diagnostic (White Screenbox near cavity #6)

PI-Max ICCD 1300, 25mm Gen III intensifier, 20x20um, (1340x1300) (UNIGEN)

Model: 7455-0008 **System ID:** 85113
Serial Number: 2604060002 (purchased 2006)
Gate: 10ns (gate out actually reads 20nsec)
Gain: 25
Delay: T + 192.082600µs (DG 535 #3, Channel D)
Internal Delay: 25ns
Gate Delay from Ext. Trig. In: 30ns
Aux Trig Out Delay: 0 nsec
ADC Rate: 1MHz
Detector Temperature: -15C (locked)
Background Counts: 48 (average)
Slit Orientation: 2D Image of diode

Input Optics

Lens: Century LW 150-600mm Canon f/5.6 (S/N C41399)
Extenders: 2X + 1.4X
Input: 400mm FL, F/22
F-stop: 16
TOF from source to detector: 25.5nsec
Screenbox wall to camera distance: 10.4" (0.9nsec)
Wall to screenbox distance: 49" (4.1nsec)
ICCD Monitor out Delay in DAS (AUX_OUT): 107.9nsec
ICCD Aux. out Delay in DAS (PI_GATE): 106.8nsec

Shot 2046

Princeton Instruments SpectraPro 2500i Spectrometer:

S/N: 25580557
Grating: 150g/mm 5000 Angstrom Blaze Angle
Grating Size: 68mm x 68mm
Grating Dispersion: 13.1nm/mm
Wavelength Coverage: 351nm
Setting: 550nm
Slit: 100 microns
Input fiber: 100 microns
Pathlength through Instrument: 175.5cm (5.8nsec)

Spectrograph Input Optics

Lens: Achromatic pair (1:1.5 magnification)
ThorLabs (Part #MAP1050-75-A)
Input: 50mm FL, F/2.2
Output: 75mm FL, F/3.3
Object Distance: 37.7mm
Image Distance: 65.8mm

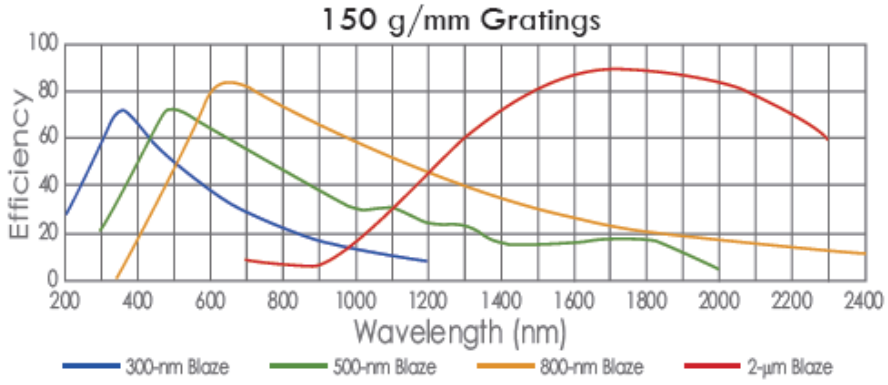

The grating curves show typical relative efficiency for the various blaze wavelengths and should be used as a comparison guide only.

Detector	PIMAX:1024x256-25mm		Center Wavelength(nm)	570 Enter	
Hor. pixel	961	Vert. pixels 253	Order	1	
Pixel Size µm	26	CCD width/mm 24.6	Select Excitation Laser	633 nm	
Linewidth,pixels	1.6		Laser wavelength,nm	633	
			Dispersion nm/mm	13.085	
Spectrograph	SP-2500i		Bandwidth per pixel	0.34 nm	
Focal Length(mm)	500	Aperture ratio f/6.5	CCD Resolution(FWHM)	0.544	
Select Grating	150 l		Center Wavenumber(cm-1)	17543.86	
Grooves/mm	150		Next resolved wavelength	570.544	Grating Rotation 2.47 deg.
Grating size/mm	68 x 68, 68 x 84 opt.		Next resolved wavenumber	17527.13	Resolution,cm-1 16.73
CCD coverage	321 nm		Short Wavelength	409 nm	24450 cm-1
	10766 cm-1		Long Wavelength	730 nm	13699 cm-1
nm to eV	633	1.95869 eV	Low Raman shift	-8650 cm-1	High Raman shift 2098 cm-1

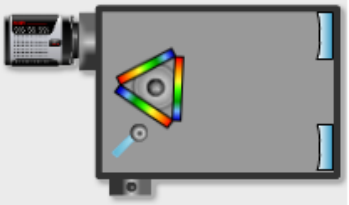

Shot 2046

Streak Camera #1 (Bechtel Nevada Model L-CA-24) Settings:

Camera S/N: 220
Fiber Input: Fiber 18 (on-axis, skimming the anode surface, new dual fiber array)
Fiber length: 34.5" (3nsec) + 417" (52.1ns fiber delay) + 135" (16.9ns) fiber jumper + fiber to slit (0.5ns) + 5.8ns transit time in air through 0.5m Acton Spectrometer = **78.3nsec**
Scintillation Fiber: 181.68" (22.7nsec) + 21.5nsec + 85.5" (11nsec) = **55.2nsec**
85.5" (11nsec) fiber attached to RITS chamber
Sweep Setting: 240ns
MCP Voltage: 650V
MCP Gate Width: ~300usec
Pos. Ramp: 1963V
Neg. Ramp: 1950V
Gate: 874V
CCD: Spectral Instruments Series 800, S/N 800-244
SI Software Version: SI Image SGL E
CCD Integration Time: 100 msec
CCD Delay: 50.1msec (50msec pre-trigger)
Temp. Setting: -10C

DG535 Setup for Streak Camera #1:
Rackmount DG: T + 50.092231480 msec (DG 535 #1, Channel B)
(added delay to compensate for the 45" fiber jumper, delay controlled by DAS)
T_o = CCD Trigger Input (50 Ω, TTL, Inverted) (CCD needs to be 50msec early)
A = T + .05000000sec
B = A + 300 μs
C = A + 100 μsec (Streak/Comb, Rear Output, 50Ω, Variable, 3V, 0 Offset)
A^B = MCP (50Ω, TTL, Normal)
AvB (Terminate at output with 50 Ω)
D = A + 100.195μsec = Impulse Generators (High Z, TTL, Normal)

Optics:

Lens: 50.0mm, 150mm fl, Glass Achromat, F/3.0, Edmund Optics Part #49-285
Focal Spot Size: 1.0mm
Distance from Diode to outside of window flange: 29 11/16" (754mm)
Window: 75mm diameter Borofloat borosilicate, Edmund Optics Part #43-894 (uncoated)

Shot 2046

Calibrations:

1) Green Laser (532nm): 1958 pixel; Intensity: 1050 @ 650V Power: 190nW
2) Red Laser (632.8nm): 2800 pixel; Intensity: 5400 @ 650V Power: 37nW
3) Xe Lamp (460.3nm): pixel; Intensity: @ 650V Power: 3.0μW
4) Xe Lamp (484.4nm): pixel; Intensity: @650V
5) Xe Lamp (529.2nm): pixel; Intensity: @650V

Comb (NSTec Model H-OE-51)/Impulse (NSTec Model H-OE-51):

Comb Delay: A + 100.4μsec (Ch D. BNC 555)
Comb Settings: 10ns; power setting: 10
Δ Comb: 225pixels Number: 12
50 micron fiber

Impulse Delay: A+ 100.4μsec
Impulse Fiber length: 85.5" + 43.5" = 129" = 16.1ns
Impulse Cable Delay in DAS (IMPSPC): 90.2nsec
100 micron fiber
Pixel: 1151
Δ Impulse to X-ray pulse: 40nsec

300W DC Xenon Lamp:

Focus Mode
Gate Width: 968ns (800ns actual)
Lens tube position: 628mm from filter holder on arc lamp

Pulsed Xenon Lamp:

Delay: 189 μs (BNC 555 Delay Generator)
Δ IMP/PIN_1: _____
Δ IMP/PINDIOD_3: _____
Δ PIN_1/PINDIOD_3: _____

Hg Lamp:

Current: 18.0mA
Gate: 100 μsec
Gain: 150
Power reading @ 254nm: ____μW

Notes: Al-coated (thermal spray) tantalum target. A 3mm wide stripe across the center of the target has been coated. The surface has been roughened from grit blasting. Looking for Al III (5696A, 5722A) line splitting.

Shot 2046

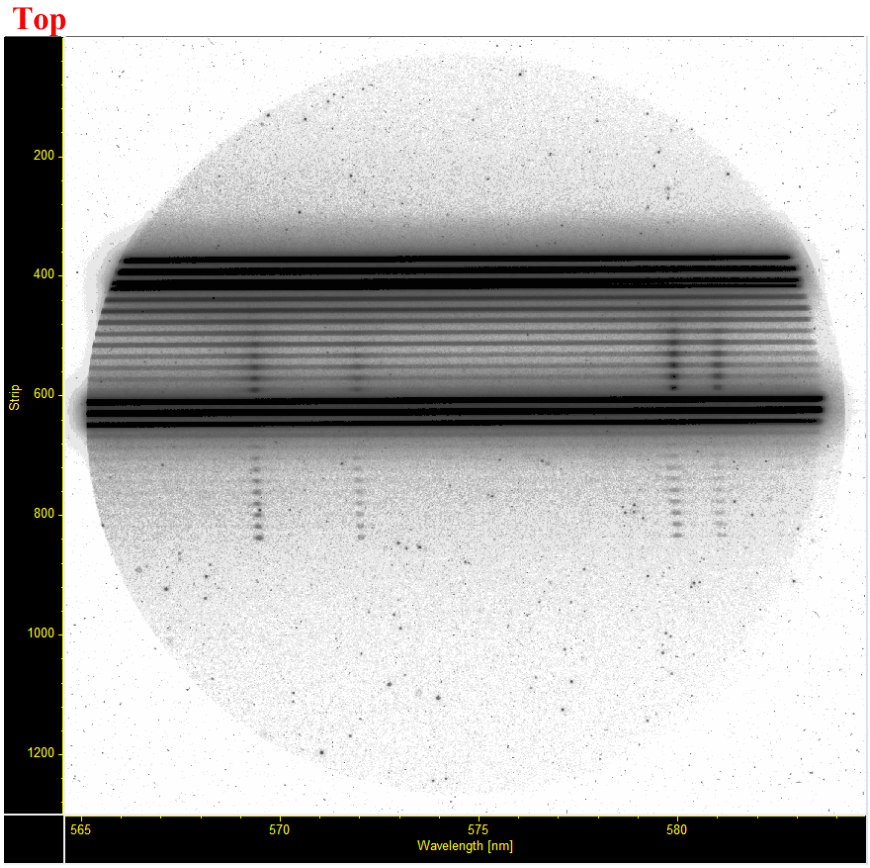

Figure E1. Shot 2046 (skimming the anode surface)

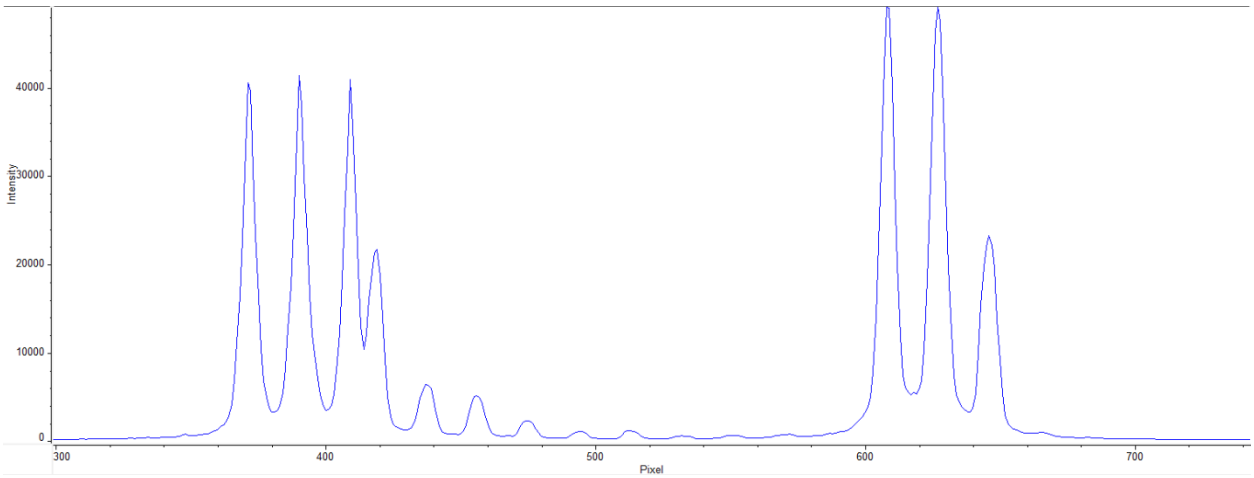

Figure E2. Shot 2046: Radial Lineout. Fibers 12 is the brightest (aligned to fiber 24).

Shot 2046

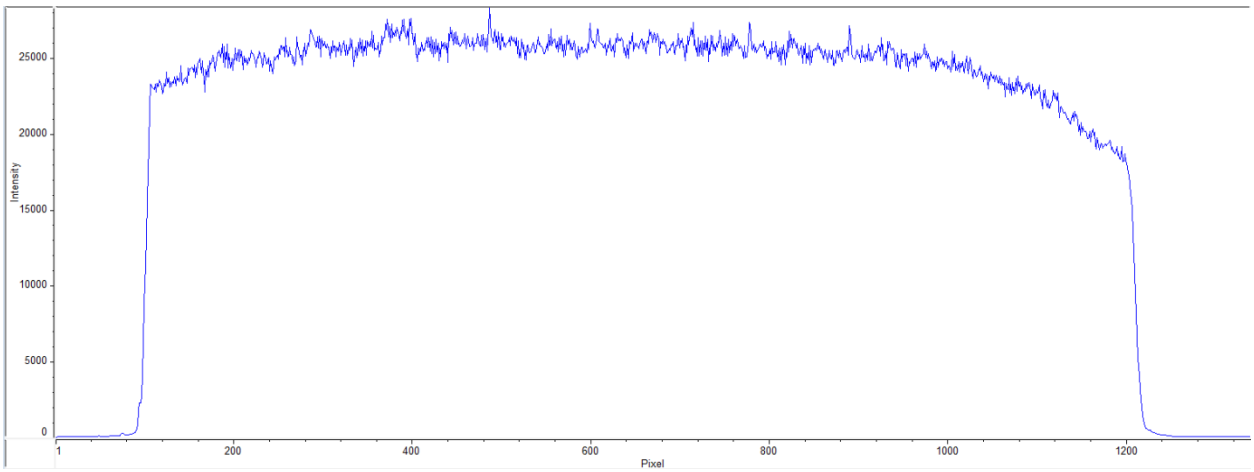

Figure E3. 2046: Fiber 26 (8 Pixel Average)

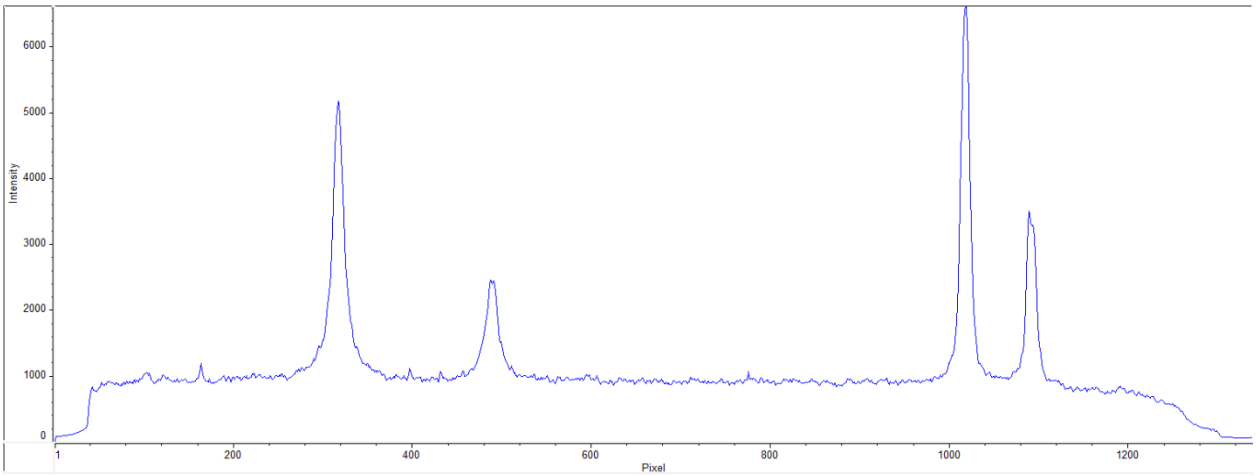

Figure E4. Shot 2046: Fiber 14 (9 Pixel Average)

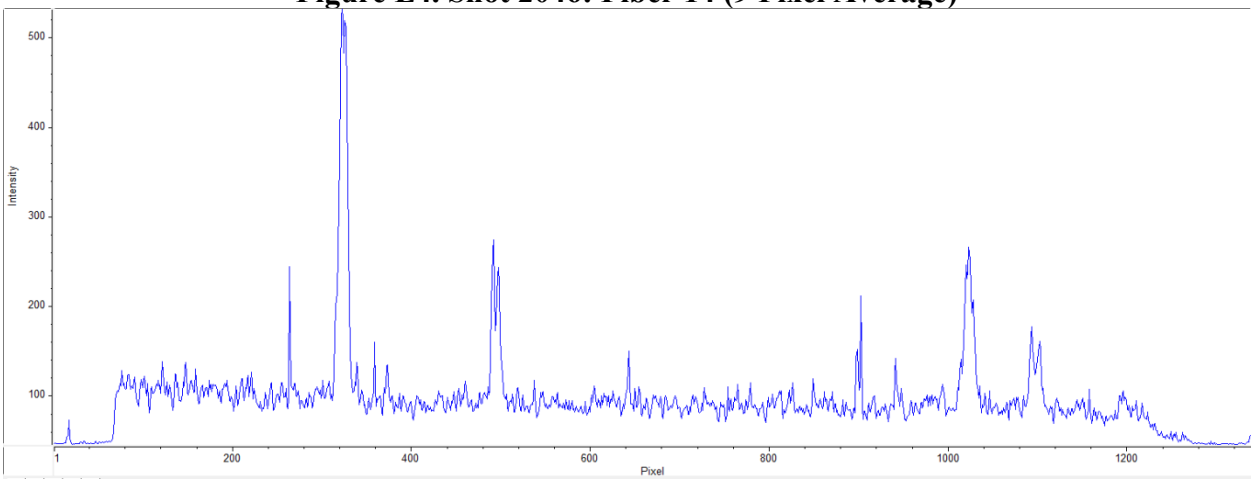

Figure E5. Shot 2046: Fiber 1 (8 Pixel Average)

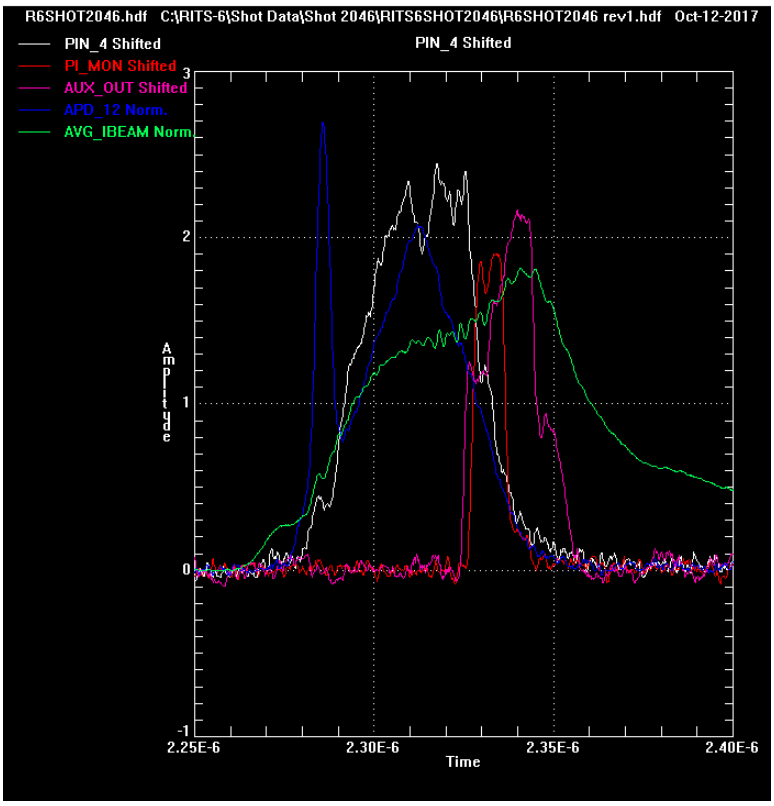

Figure E6. Camera gate relative to PIN_4 (nsec).

Top **Bottom**

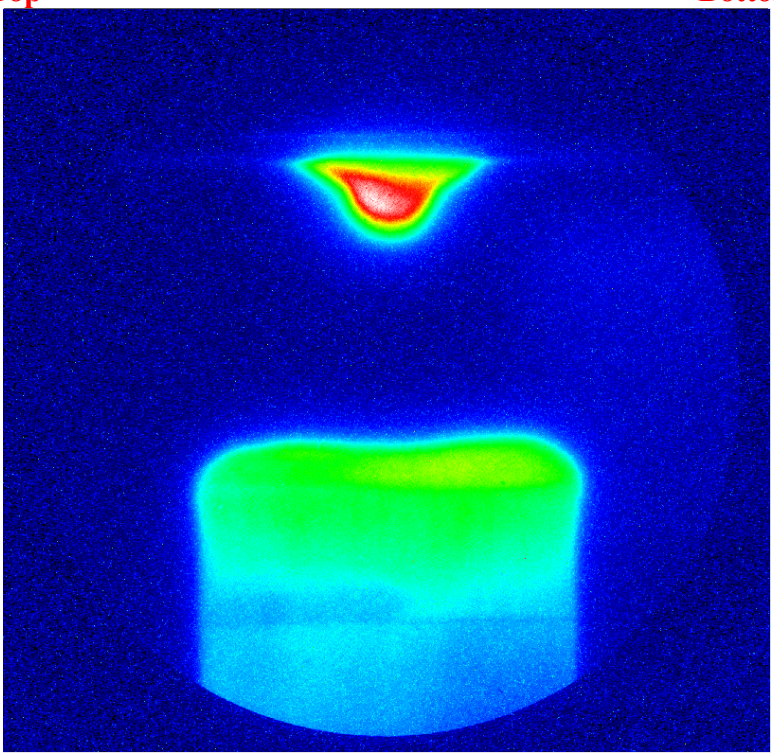

Figure E7. Shot 2046: Anode-Cathode Image; 58,068 Pk. Int.

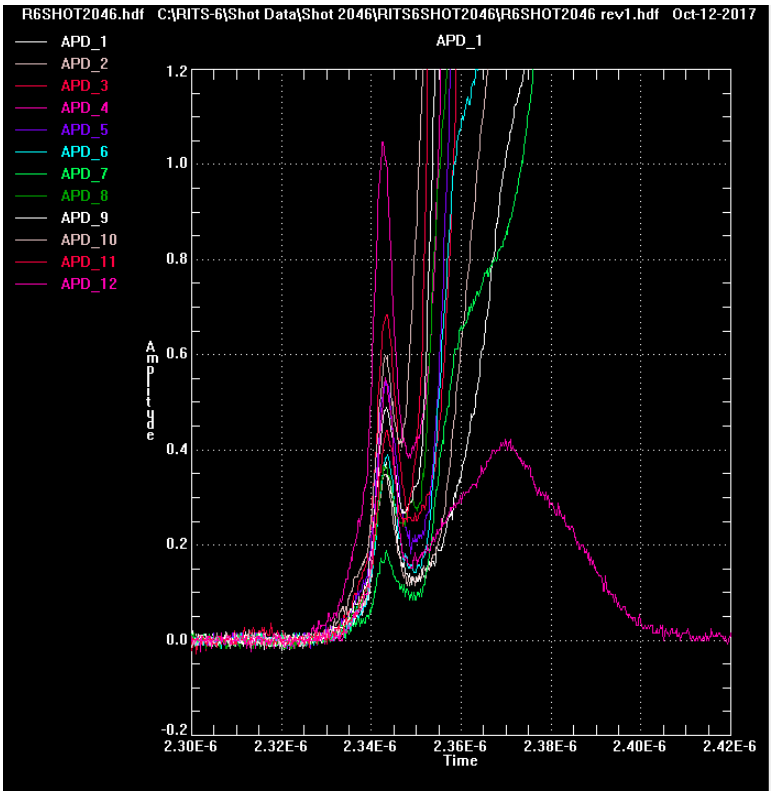

Figure E8. Shot 2046 APD Signals

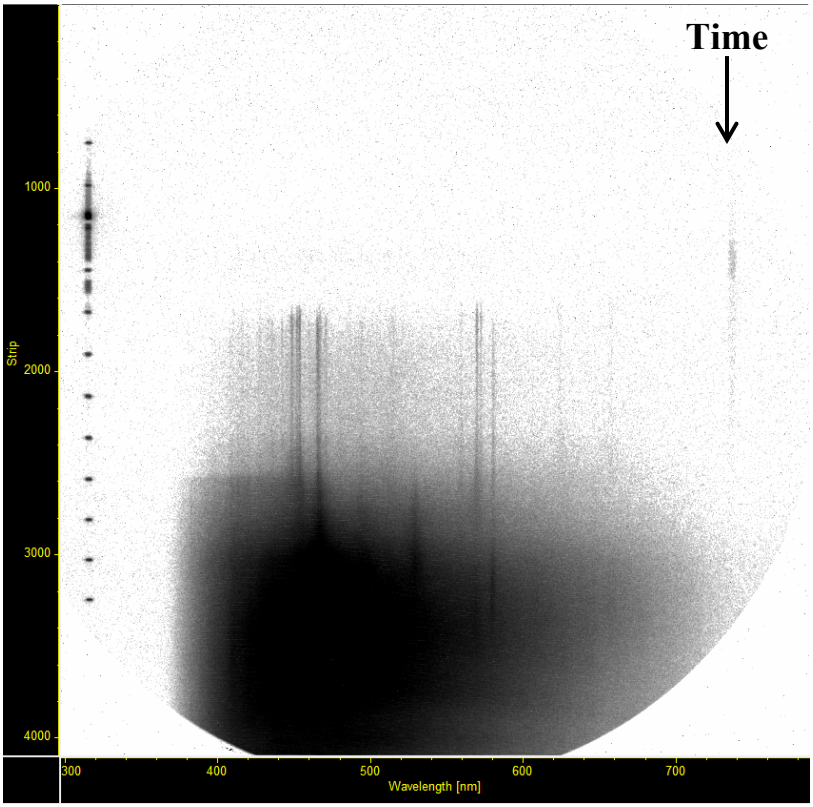

Figure E9. Shot 2046 Streak Spectra.

Shot 2046

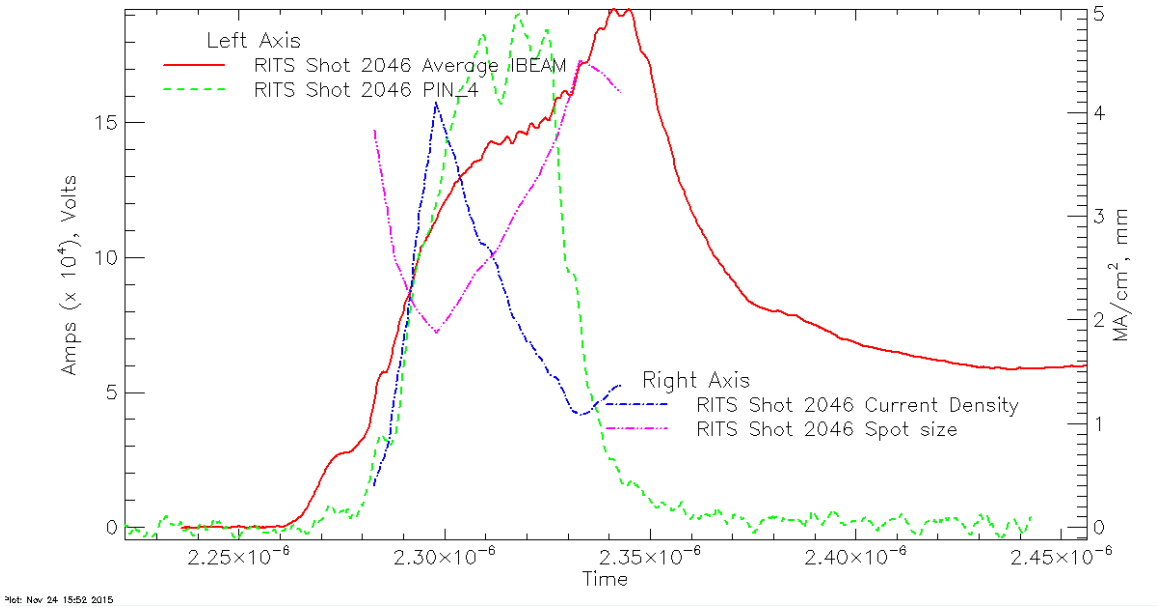

Figure E10. Current Density vs. Spot size

Top

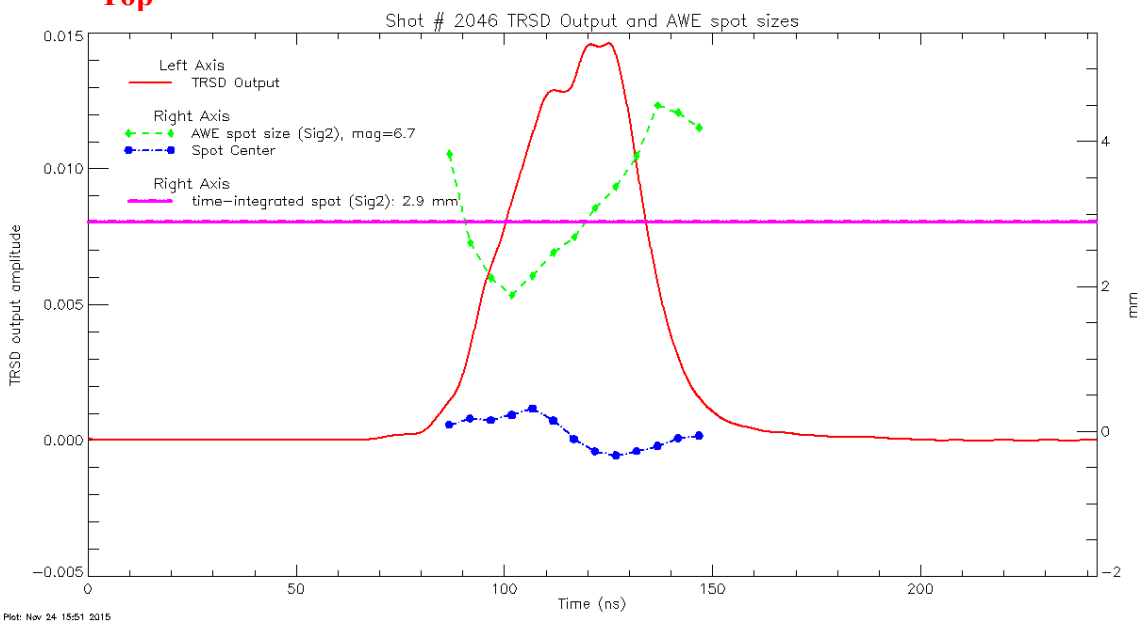

Bottom

Figure E11. TRSD spots size and centroid movement.

Shot 2046

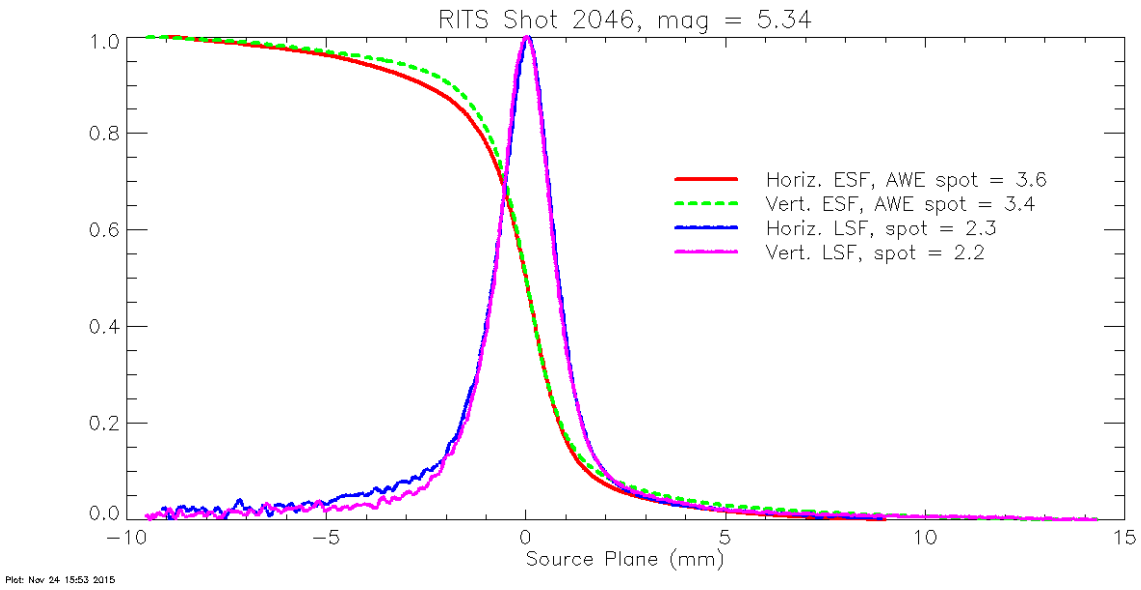

Figure E12. TRSD Spot Sizes.

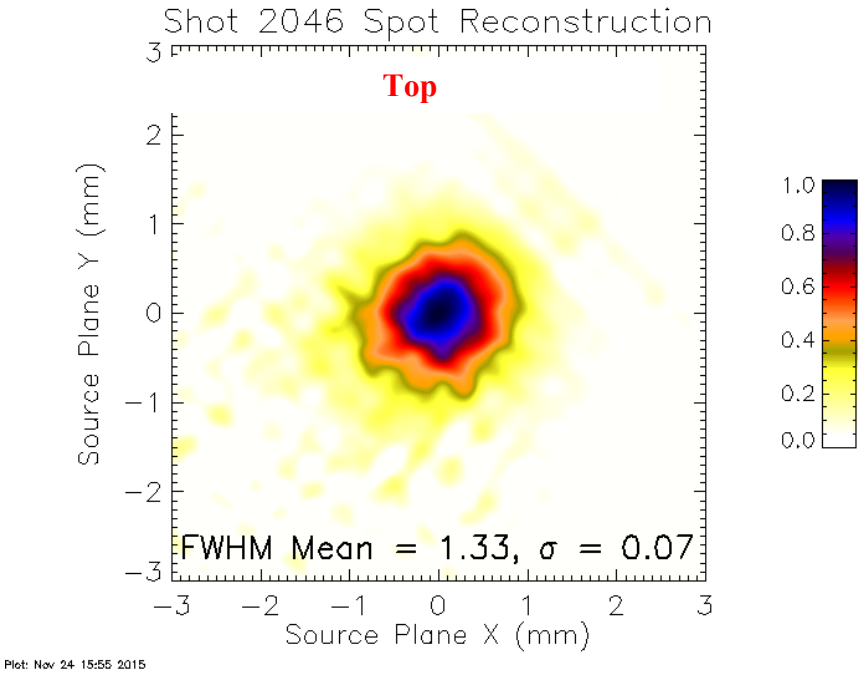

Figure E13. PSF Spot Size.

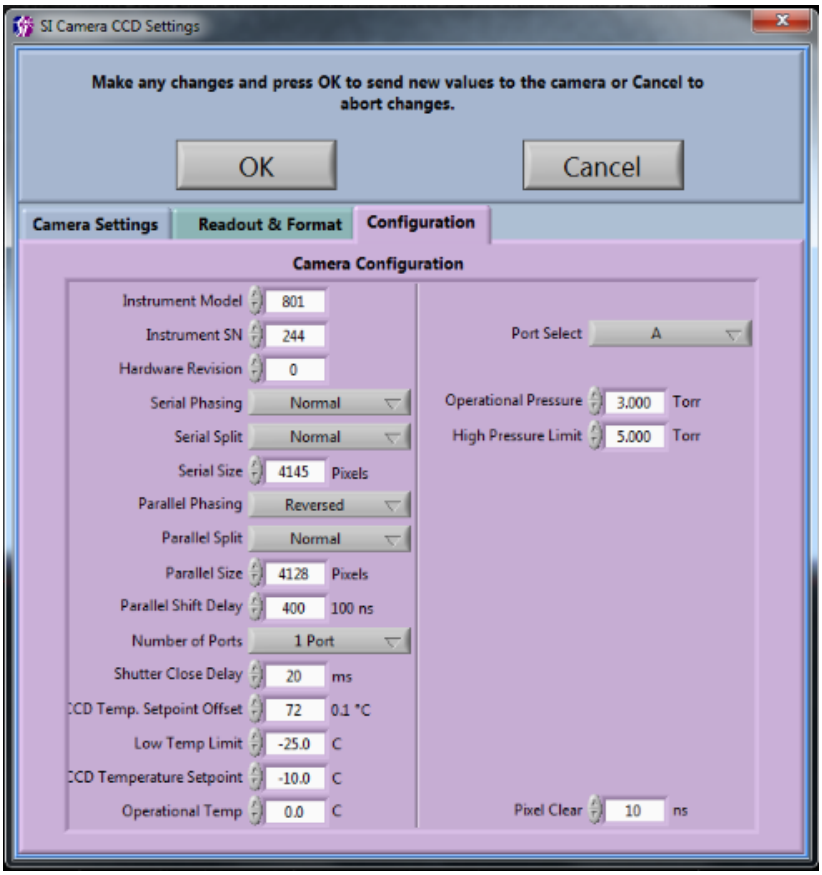

Figure E14. Streak Camera Configuration Settings

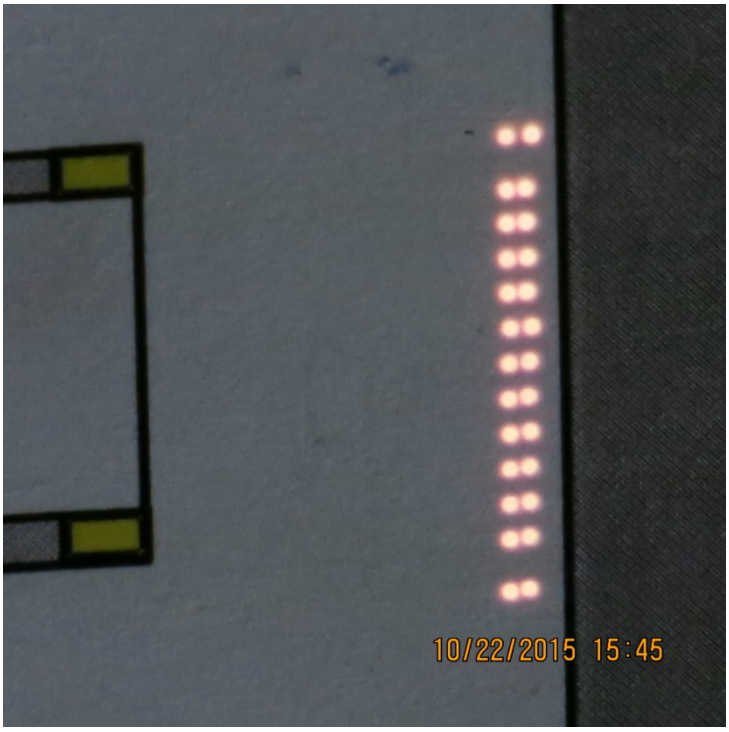

Figure E15. Double, 100um fiber array

DISTRIBUTION

1	MS1152	K.L. Cartwright	1352
3	MS1178	M.D. Johnston	1656
1	MS1178	M.L. Kiefer	1656
1	MS1178	S.G. Patel	1656
1	MS1178	T.J. Webb	1675
1	MS1195	M.E. Cuneo	1650
1	MS1197	R.E. Falcon	1683
1	MS0899	Technical Library	9536 (electronic copy)
1	MS0359	D. Chavez, LDRD Office	1911


Sandia National Laboratories